Politecnico di Milano

SCHOOL OF INDUSTRIAL AND INFORMATION ENGINEERING
Master's Degree in Aeronautical Engineering with specialisation in Aerodynamics

Master's Degree thesis

The effects of atmospheric stability on pollutant dispersion: analysis of the flow and the concentration field

Supervisor
Prof. Maurizio Boffadossi

Co-supervisor
Prof. Pietro Salizzoni

Candidate
Laerte Adami
Matr.900222

Academic Year 2019–2020

Ringraziamenti

Desidero innanzitutto ringraziare il professor Maurizio Boffadossi del Politecnico di Milano, il professor Pietro Salizzoni e il ricercatore Massimo Marro dell'École Centrale di Lione e il professor Matteo Carpentieri dell'università del Surrey per avermi sostenuto, dall'inizio alla fine, in questo percorso di tesi. Nonostante la lontananza, si è creato un rapporto costruttivo, trasformando il lavoro in un'attività piacevole. Le esperienze a Lione e a Guildford, seppur prematuramente interrotte dalla pandemia, sono state una grande fonte di crescita e di soddisfazione. Sono felice di aver potuto chiudere il mio percorso accademico con questa opportunità.

Vorrei quindi ringraziare la mia famiglia. I miei genitori Isabella e Giorgio per avermi permesso di perseguire un obbiettivo lungo e tortuoso come una laurea magistrale. Ci sono stati dei momenti complessi ma spero che questo traguardo potrà essere una fonte di serenità per il futuro.

Un ringraziamento affettuoso anche a mia sorella Lara, da sempre un porto sicuro in cui trovare affetto e amicizia. Siamo cresciuti insieme e questo è un risultato che voglio condividere con te.

Un grazie particolare va a tutte quelle persone che hanno contribuito alla mia crescita, fuori e dentro l'università.

Un grazie agli amici di una vita con cui elencare tutte le avventure vissute sarebbe impossibile, un grazie a quelle persone scoperte solo recentemente che rendono la novità un qualcosa di sempre interessante, un grazie ai compagni di università con cui si sono affrontate le lunghe giornate di lavoro e un grazie anche a chi è stato importante in qualche momento del mio percorso e ora ha preso strade diverse. Considero tutti voi una seconda famiglia allargata e dedico anche a voi questo risultato perché, un po', è anche vostro.

Milano, 24 Luglio 2020 Laerte

Contents

List of Figures

List of Tables

Sommario

Nonostante l'importanza, nonché il crescente interesse, dello studio di come un inquinante generico è trasportato nell'atmosfera in condizioni non neutre, non sono ad oggi disponibili degli esperimenti il laboratorio che trattino questo argomento. Lo scopo di questo lavoro è stato proprio cercare di colmare questa lacuna, studiando la dispersione di un inquinante in un'atmosfera stabile. Una campagna sperimentale è stata svolta presso l'EnFlo Lab dell'università del Surrey (UK). All'interno della galleria del vento, una sorgente elevata dal suolo è stata immersa in uno strato limite turbolento ben sviluppato, a diverse condizioni di stabilità. In questo contesto, sono state effettuate delle misurazioni di concentrazione, velocità e temperatura contemporaneamente, nello stesso volume di controllo.

E' stata svolta un'analisi preliminare con lo scopo di caratterizzare il campo di moto tramite uno studio delle componenti medie e fluttuanti del campo. Sono state verificate le condizioni di soppressione della turbolenza per mezzo della stabilità. Sono state inoltre valutate le scale di lunghezza e di tempo euleriane. In questa fase, si è osservato un buon accordo con studi precedenti svolti nella stessa struttura.

Uno studio innovativo è stato svolto sul campo di concentrazione e il suo accoppiamento con il campo di moto. L'effetto delle diverse intensità di stabilità e delle diverse condizioni della sorgente è stato valutato. Il segnale di concentrazione è stato analizzato fino al quarto ordine per quanto riguarda i momenti statistici. Il confronto tra la funzione di distribuzione di probabilità del segnale di concentrazione e la distribuzione gamma ha prodotto un risultato positivo.

Il lavoro è continuato con uno studio sui flussi turbolenti e sui coefficienti di diffusione al variare della stabilità. Tramite questi strumenti, è stato possibile valutare i profili verticali del numero di Schmidt turbolento. Una valutazione dell'apertura del pennacchio è stata fatta in parallelo tra i dati sperimentali e i modelli disponibili in letteratura. Tramite l'impego dell'analisi spettrale è stato possibile uno studio dettagliato sui processi diffusivi in azione. Nella parte finale del presente lavoro, è fornita una soluzione analitica per il momento secondo del segnale di concentrazione.

Abstract

The study on how a generic pollutant is transferred in the atmosphere in non-neutral conditions is extremely important. Despite this, no laboratory experiments have been performed so far. The purpose of the present work is to try to fill this lack of knowledge.

The experimental campaign has been performed at the wind tunnel of the EnFlo Lab at University of Surrey. A L-shaped source is placed inside a full developed turbulent boundary layer at different stability conditions. Measurements of concentration, temperature and velocity have been performed simultaneously in the same control volume.

A characterization of the flow field has been performed as a preliminary task, analyzing the mean and the turbulent components. Expected characteristics of turbulence suppression by means of stratification have been observed. Moreover, length scales and time scales approach have been computed with the Eulerian. A good agreement has been observed with the boundary layers produced for this work and other boundary layers analyzed in previous studies at the EnFlo Lab.

The most innovative results have been obtained by analyzing the concentration field and the coupling between this and the flow field. Having performed experiments with two source sizes and two different stratifications, among the neutral case used as reference, it has been possible to evaluate the respective effects on dispersion. The concentration has been studied up to the fourth order statistical moment. A comparison between the probability density function of concentration and the gamma distribution has shown good agreement.

Moreover, turbulent fluxes and turbulent diffusion coefficients have been computed by means of the standard gradient diffusion hypothesis. With these tools, profiles of Schmidt number for different stability conditions have been computed. The work has continued by analyzing the plume spread and its models. The concentration has been studied also by means of spectra from which it has been possible to compute the value of concentration dissipation rate and finally the mixing times at different locations further from the source. In the final part of the work, an analytical solution for the standard deviation of concentration has been computed.

Introduction

Air pollution is a mainstream topic since several decades. It is strictly linked to human activities on Earth and started to be a serious problem with urbanization and the beginning of the industrial era. In the first part of 20th century, air pollution in cities was mainly produced by combustion of coal, which was the only source of energy. Nowadays the main sources of pollution in cities are private cars emission and home heating.

Air pollution can be extremely dangerous for life and it has been estimated to be the cause of death of 7 million people per year worldwide. Among the principal diseases related to pollution, there are respiratory infections, heart disease, chronic obstructive pulmonary disease, stroke and lung cancer [1], [3]. Recent studies have also found a relationship between ambient air pollutants and the infection caused by the the coronavirus pneumonia, namely COVID-19 [39]. Moreover, air pollution harms animals, plants, the environment in general and it is also strictly related to climate change.

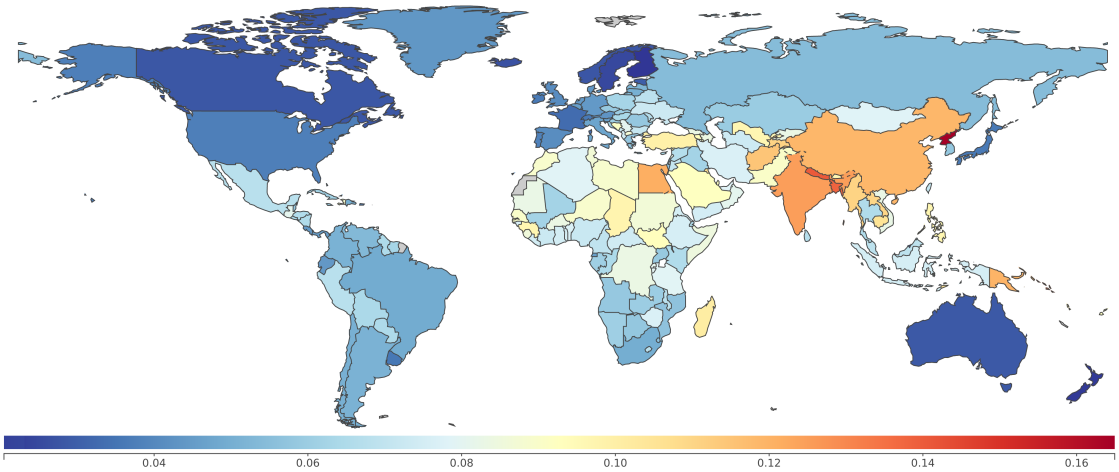

Figure 1. Percentage of death caused by air pollution in 2017.

Figure 1 shows the percentage of deaths caused by pollution over the overall number of deaths in every country in 2017. The chart is realized by the Institute for Health Metrics and Evaluation. For example, in Italy the percentage of deaths related to pollution is 4.72%, in France 3.28% and North Korea has a peak of 16.5% [13].

It has been estimated that air pollution costs 5 trillion US dollars to the world economy. It causes a loss in productivity and degradation in life quality according

Figure 2. Smoke from the bushfires along Australia's southeast coast on January 30, 2020.

Figure 3. Pollutant release.

with a joint study by the World Bank and the Institute for Health Metrics and Evaluation at the University of Washington [11].

The atmospheric dispersion is the main process that governs the transfer of a pollutant within the atmosphere. The nature of this pollutant can be whichever: the smoke of a wildfire (figure 2), the emission of a chimney in a plant (figure 3), pollution from urban sources, volcanic eruptions and uncountable more.

The atmospheric turbulence is a complex phenomenon to study and to analyze. The peculiarity is the incessantly changing conditions, from a local scale to a global one. The dispersion of a pollutant is strictly related to the atmospheric condition in which it is diluted. Due to this complexity, it is not an easy task to study, predict and model the behavior of a pollutant.

The lower part of the atmosphere which actively interacts with the ground, referred to as atmospheric boundary layer, is strongly dependent on day and night cycle or in general the meteorological conditions. The main process governing this layer is the presence of heat fluxes from the ground to the air, mainly during sunny days, or from the air to the ground, more likely to happen during cloudy nights. This causes an effect called stratification for which the density of the air changes significantly along the vertical direction. Following what previously said, the pollutant transfer will depend on the atmospheric conditions. As a reference, figure 4 shows a plume subjected to boundary layer in unstable conditions while in figure 5 the stable case is reported. The stable condition is in general the more critical one between the two since the pollutant is subjected to weaker mixing processes.

In spite of the importance of this subject, there are no laboratory experiments available in literature nowadays on the effect of heat fluxes in the dispersion of a

Figure 4. Plume in unstable conditions.

Figure 5. Plume in stable conditions.

pollutant in an atmosphere with stratification, both stable and unstable.

To fill this lack of information, the objective of this work is to study and try to comprehend the effect of boundary layer stratification on the dispersion of a pollutant from an elevated source. The work has been performed in collaboration with the Laboratory of Fluid Mechanics and Acoustics (LMFA) of the École Centrale de Lyon and the EnFlo Lab at University of Surrey. The wind tunnel at EnFlo Lab at Guildford (UK) is one of the few wind tunnels in Europe where it is possible to reproduce an atmospheric boundary layer with stratification, both stable and unstable. To perform these experiments a new layout for instruments has been used, allowing to collect data for concentration, temperature and velocity simultaneously in the same control volume.

The present work is thus very innovative and unique as it provides new experimental tools to this extremely actual and relevant issue.

Chapter 1

Environmental fluid dynamics

1.1 Atmosphere

The atmosphere is an everyday life concept but it is governed by extremely complex phenomena. A deep understanding of its composition, its dynamics and its cycles is a crucial task to understand our Earth.

The word atmosphere is a wide concept and it is not only correlated with our planet. It takes its name from the ancient Greek words $\alpha\tau\mu\acute{o}\varsigma$ (atmós) and $\sigma\varphi\alpha\hat{\imath}\varrho\alpha$ (sphaîra), which mean vapour and sphere. It is formed by layers of different gases, kept close to the Earth's surface by gravity.

It has vital roles for life on Earth, among which:

- absorbing ultraviolet solar radiation,
- warming the surface of the Earth through greenhouse effect,
- mitigating temperature excursions.

The atmosphere of Earth is composed by different gases in different percentages. The main chemical component is nitrogen (78.09%), followed by oxygen (20.95%), argon (0.93%) and small quantities of other gases such as carbon dioxide, neon, etc. [26]. The chemical composition is shown in figure 1.1.

Of course, thermodynamic conditions are not uniform within the atmosphere. Density and pressure show a decreasing behavior with the altitude. The temperature, and hence the speed of sound, has instead a more complex trend. Figure 1.2 shows vertical profiles of thermodynamic quantities in the layers of the atmosphere.

The division in layers is the following:

- troposphere, from 0 to 12 km. This is the lowest part of atmosphere and has a variable height in a range from 9 to 17 km. It contains about 80% of the mass of the whole atmosphere. In this layer most of the weather phenomena take place;
- stratosphere, from 12 to 50 km. This layer is separated from the troposphere by the tropopause. The temperature increases with height due to absorption of ultraviolet radiation by the ozone layer which is contained in the stratosphere;

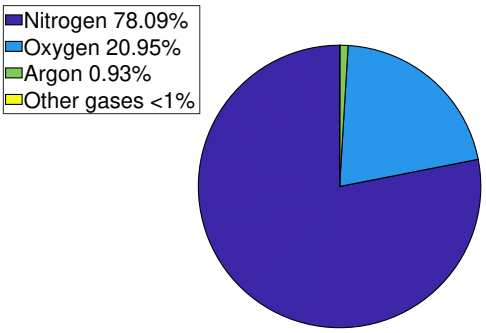

Figure 1.1. Chemical composition of Earth atmosphere.

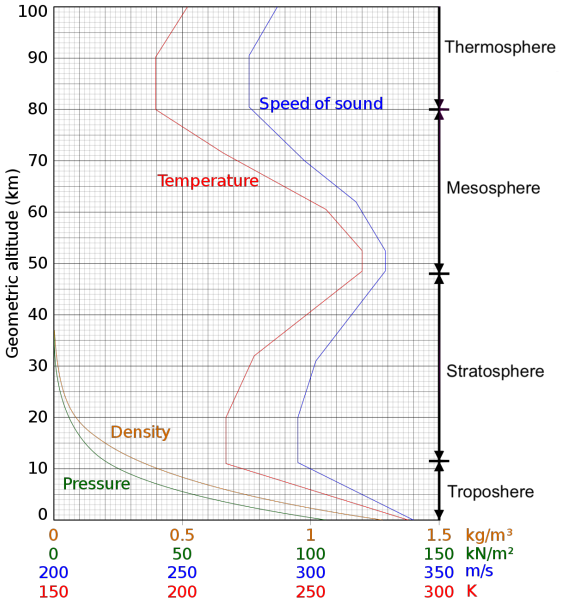

Figure 1.2. Thermodynamic quantities within the atmosphere.

- mesosphere, from 50 to 80 km. In this layer, the temperature drops with height reaching low temperatures with an average of about -85°C. This is also the layer where most of the meteors entering atmosphere of Earth get burned;

- thermosphere, from 80 to 700 km. The extension of this layer varies considerably with the variation of solar activity. The temperature increases with height reaching at maximum 1500°C and the air is so rarefied that a molecule of oxygen can move up to 1 km without colliding with other molecules. The International Space Station orbits in this layer, between 350 and 420 km;

- exosphere, from 700 to 10000 km. This is the outermost layer of the atmosphere of Earth. It does not behave like a gas since it is extremely rarefied. Most of satellites orbit in this layer.

Figure 1.3 shows a sunset captured from the International Space Station ISS over the Indian Ocean. It is easy to recognize the different layers forming the Earth atmosphere.

1.1.1 The atmospheric boundary layer

The atmospheric boundary layer (ABL), also called planetary boundary layer, is the lowest part of the troposphere [32]. The study and the understanding of atmospheric boundary layer is of vital importance for a wide range of research fields, such as pollution dispersion or weather forecast.

The atmospheric boundary layer is characterized by the interaction between the movement of huge masses of air and the Earth's surface. The latter shows great variety, from mountain chains to flat and calm seas, from metropolis to small rural towns. Due to the imposition of no-slip condition, the wind velocity at ground level

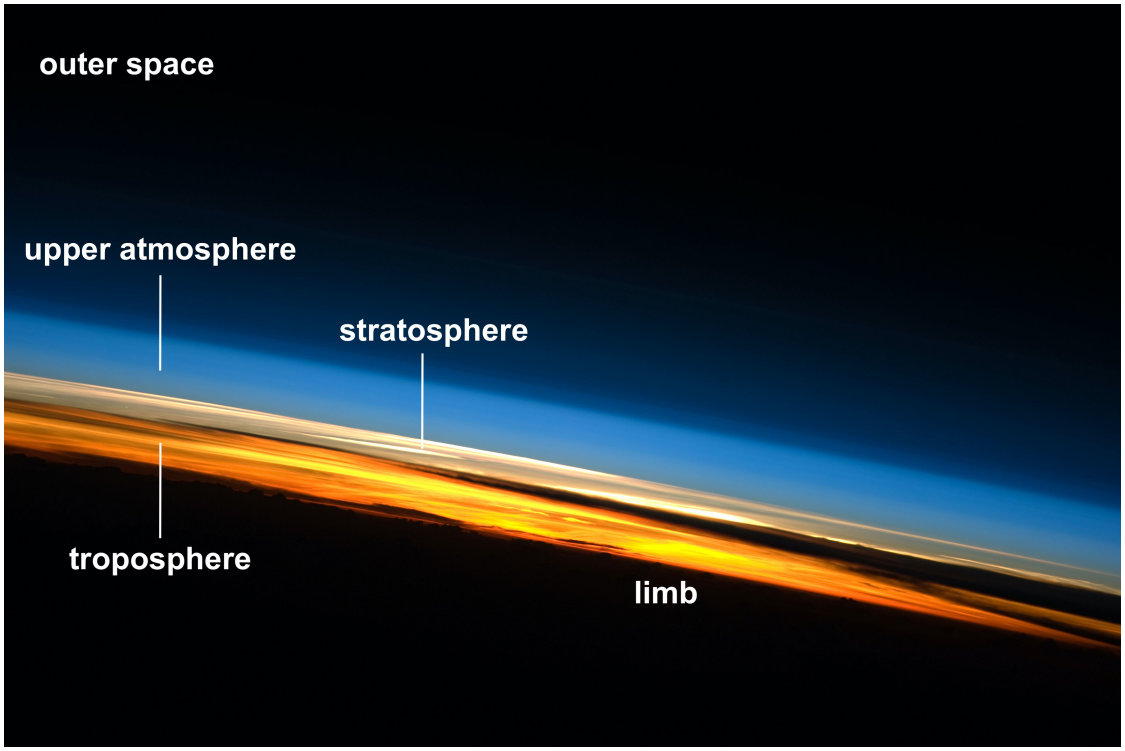

Figure 1.3. Atmosphere of Earth from ISS.

is null and with increasing height the velocity increases as well until it reaches the undisturbed wind speed at the top of atmospheric boundary layer.

The simplest description of an atmospheric boundary layer is given by considering a prevailing wind in a fixed direction and fluid dynamic or thermodynamic quantities which are homogeneous in the horizontal plane and vary only along the vertical direction, [4], [36].

The extension of the boundary layer varies in a great range, from 100 meters in a clear and calm night to 3 km during the afternoon in dry regions.

As a first approximation, it is useful to consider the atmospheric boundary layer in a neutral condition, i.e. without temperature gradients. It can be divided in different regions along the vertical direction:

- outer or mixed layer,
- inertial sublayer,
- roughness sublayer.

In the roughness layer, the flow is strongly dependent on the roughness elements on the surface of the Earth and it is not homogeneous in horizontal planes. The inertial region lays above the roughness sublayer and below the outer layer. Here the velocity profile is well described by a log law, which will be presented in section 3.2.

Differently from usual aeronautical boundary layers, when studying atmospheric boundary layer it is mandatory to consider the effect of heat flux in the development of the boundary layer itself. This fact is strongly evident in the day and night cycle

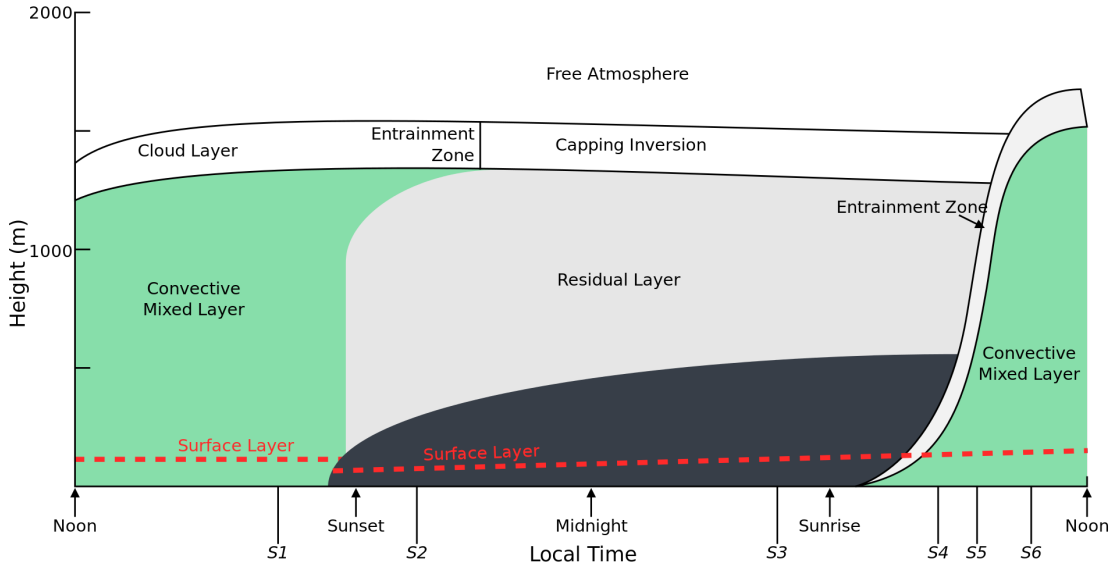

Figure 1.4. ABL during day and night cycle.

or in the summer and winter seasonal changes. The heat comes from the Earth's surface which is subjected to great irradiation from the sun during daytime and during summertime. This temperature gradient from the surface to the air causes heat fluxes and the formation of a convective mixed layer, which can be also called convective boundary layer and it is considered unstable. It grows in height during the first hours of the day. In the nighttime, or during winter time when the heating power of the sun is weaker, the process is the opposite. The soil is colder than the air and this causes a "negative heat flux" from the atmosphere towards the soil. This is the so-called stable boundary layer or SBL. If a convective boundary layer was formed during the day, a residual layer will remain over the SBL. A simple scheme of a typical boundary layer is shown in figure 1.4.

1.2 Boussinesq approximation

The Boussinesq approximation is a useful tool when studying fluid dynamic in a stratified medium or thermal flows. Moreover, it can be employed in a wider range of fields such as studying wave propagation in a density stratified medium, thermal instability and geophysical fluid dynamic.

It was first introduced by Boussinesq in 1903 and states that the density change in a fluid can be neglected when ρ appears in equation terms which are not multiplied by g, the intensity of gravitational field.

This approximation states that density variations are caused only by temperature variations neglecting the pressure contribution,

$$\frac{\rho'}{\overline{\rho}} = -\frac{T'}{\overline{T}}. \tag{1.1}$$

According to Boussinesq's procedure, the continuity equation, i.e.

$$\frac{\partial \rho}{\partial t} + \frac{\partial}{\partial x_j}(\rho u_j) = 0, \tag{1.2}$$

can be replaced with the incompressibility form, i.e.

$$\frac{\partial u_j}{\partial x_j} = 0. \tag{1.3}$$

This states that, following a fluid parcel, the density gradients are small compared to velocity gradients.

Considering the density field decomposed in a mean and a varying component as $\rho = \overline{\rho} + \rho'$, the momentum equation reads

$$\overline{\rho}\left(\frac{\partial}{\partial t} + u_j \frac{\partial}{\partial x_j}\right) u_i = -\frac{\partial p}{\partial x_i} + (\overline{\rho} + \rho')g_i + \mu \frac{\partial^2 u_i}{\partial x_j^2}, \tag{1.4}$$

where μ is the dynamic viscosity.

When the fluid is at rest and only the vertical direction is considered, equation 1.4 gives the static equilibrium as

$$-\frac{\partial p_s}{\partial z} - \overline{\rho} g = 0, \tag{1.5}$$

where p_s is the static pressure related to this condition. The pressure term can be decomposed in a contribution given by the static equilibrium in 1.5 and a contribution caused by fluid motion p'.

The equation 1.4 can be reformulated considering the static equilibrium equation and the pressure term decomposition, leading to

$$\overline{\rho}\left(\frac{\partial}{\partial t} + u_j \frac{\partial}{\partial x_j}\right) u_i = -\frac{\partial p'}{\partial x_i} + \rho' g_i + \mu \frac{\partial^2 u_i}{\partial x_j^2}. \tag{1.6}$$

This approximation simplifies the resolution of continuity and momentum fluid dynamic equations.

1.3 Atmospheric stability

The study of the atmosphere implies taking into account also the gradient of density along the vertical direction caused by temperature gradient. The application of Boussinesq approximation simplifies the problem under the aforementioned hypotheses.

The condition of neutral stability is in general unlikely to happen, unless in some very specific cases. The study of fluid dynamic stability is applied to a wide variety of problems.

The atmospheric stability or instability is an everyday phenomenon which is the cause of different effects, like thunderstorm, cloud formation and various behaviors of pollutants in the air.

In what follows basic concepts needed to study stratified boundary layers are introduced.

1.3.1 Potential temperature

Different parameters measure the stability or the instability of the atmosphere, or geophysical flows in general, taking into account the stratified density or the kinematic heat flux. Among these, a useful thermodynamic variable is the potential temperature, indicated with Θ, which is the temperature that a parcel of fluid would have if it is adiabatically brought to the standard reference pressure. The potential temperature is obtained by means of the following equation:

$$\Theta = T\left(\frac{P_0}{P}\right)^{R/c_p}, \tag{1.7}$$

where T is the temperature, P_0 is the reference pressure, R is the universal gas constant and c_p is the specific heat for a constant pressure.

According to Boussinesq approximation, the relation between the temperature and the potential temperature, defined in 1.7, simplifies in

$$\frac{T'}{\overline{T}} = \frac{\Theta'}{\overline{\Theta}}. \tag{1.8}$$

1.3.2 Brunt-Väisälä frequency

The Brunt-Väisälä frequency is defined considering a parcel inside a field of stratified density varying with the height $\rho = \rho(z)$.

When the parcel is displaced by a small vertical increment, i.e. z', it is then subjected to a net force

$$\rho_0 \frac{\partial^2 z'}{\partial t^2} = -g\left[\rho(z) - \rho(z+z')\right], \tag{1.9}$$

where ρ_0 is a constant reference density. If a linear approximation for the density is considered, viz. $\rho(z+z') = \rho(z) + \frac{d\rho(z)}{dz}z'$, then the balance equation admits the well-known solution $z' = z'_0 e^{\sqrt{-N^2}t}$ where N is the Brunt-Väisälä frequency [33].

Regarding the atmospheric field, the Brunt-Väisälä is defined as

$$N = \sqrt{\frac{g}{\Theta}\frac{d\Theta}{dz}}, \tag{1.10}$$

where Θ is the potential temperature, as expressed in equation 1.7.

According to the sign of N^2, there are three possible cases when the parcel is pushed up:

- when $N^2 > 0$ the air parcel will move up and down around the height where the density of the parcel matches the density of the surrounding air,
- when $N^2 = 0$ the air parcel will not move any further,
- when $N^2 < 0$ the air parcel will rise unless N^2 becomes negative or zero again further up in the atmosphere.

The Brunt-Väisälä frequency commonly appears in the thermodynamic equations for the atmosphere and has an effect on whether convection occurs (i.e. warm air raising and cold air sinking).

1.3.3 Richardson number

The Richardson number is useful to evaluate the magnitude of the stability condition considered. It is defined considering at first the balance equation for the turbulent kinetic energy as follows,

$$\frac{\partial k}{\partial t}+\overline{u_j}\frac{\partial k}{\partial x_j}=-\frac{\partial}{\partial x_j}\left[\left(\frac{1}{2}\overline{u_j'u_i'u_i'}\right)+\frac{1}{\rho_0}\overline{u_j'p'}+2\nu\overline{u_i'S_{ij}'}\right]+P+\varepsilon+g\alpha\overline{u_i'\Theta'}\delta_{i3}, \quad (1.11)$$

where $k=\overline{u_i'u_i'}/2$, $S_{ij}'=\partial u_i'/\partial x_j$, ρ_0 is a reference density. The right-hand side term represents the advection of turbulent kinetic energy. The first term on the left-hand side is the transport term of turbulent kinetic energy through turbulent stresses, turbulent pressure fluctuations and viscous diffusion, the second and the third term represent respectively the shear production and the dissipation rate of turbulent kinetic energy,

$$P=-\overline{u_i'u_j'}\frac{\partial\overline{u_i}}{\partial x_j}, \quad (1.12)$$

$$\varepsilon=-2\nu\overline{S_{ij}'S_{ij}'}, \quad (1.13)$$

while the last term takes into account the buoyancy due to density stratification.

The Richardson number is defined as the ratio between the buoyancy term and the shear production term. In the case of boundary layer assumption, with z direction pointing upward from the ground, the Richardson number is expressed as

$$Ri=\frac{\text{buoyancy term}}{\text{shear production}}=\frac{-g\alpha\overline{w'\Theta'}}{-\overline{uw}(d\overline{u}/dz)}, \quad (1.14)$$

where α is the coefficient of thermal expansion.

The sign of this number depends on the sign of the heat flux in the definition, since the shear production term is greater than zero. The trivial case is considered when the buoyant term is negligible or null. This implies a neutral stability case, associated to a null Richardson number.

The stable case is characterized by a positive Richardson number, which is caused by a negative heat flux (from the air to the ground). When $Ri>1$, the buoyant suppression is greater than shear production causing turbulence suppression. In reality, the critical Richardson number at which the turbulence stops being self-supporting is less than unity since a considerable fraction of shear production is always compensated by the dissipation rate.

On the contrary, the unstable case is characterized by a negative Richardson number and a positive heat flux (from the ground to the air). In this case also, the magnitude of the parameter measures the relative strength of the instability. A large negative value means strong convection and weak mechanical turbulence. A similar description can be given in terms of the Monin-Obukhov length, see section 1.3.4.

In literature, several different formulations for this parameter are available. In general, it is easier to work with the gradient Richardson number defined as

$$Ri = \frac{N^2}{(d\overline{u}/dz)^2} = \frac{g(d\overline{\Theta}/dz)}{\Theta_0(d\overline{u}/dz)^2}, \tag{1.15}$$

where N is the Brunt-Väisälä frequency defined in equation 1.10 and the assumption that stratification is due to thermal variation has been employed to express the density gradient with the potential temperature gradient. Another useful formulation, dealing with boundary layers, is called bulk Richardson number and it is an approximation of gradient Richardson number. It is expressed as

$$Ri_b = \frac{g(\overline{\Theta}_\delta - \Theta_0)\delta}{\Theta_0 \overline{u}_\delta}, \tag{1.16}$$

where $\overline{u}_\delta$ and $\overline{\Theta}_\delta$ are the stream-wise velocity and the mean temperature at the top of the boundary layer height δ, while Θ_0 is a reference temperature and g is the intensity of gravity field.

1.3.4 Monin-Obukhov length

The Monin-Obukhov length scale is extremely useful to describe the effects of stratification and stability inside a boundary layer. It was defined in 1946 by A. M. Obukhov but A. Monin gave important contributions in the development of the similarity theory.

The Monin-Obukhov length scale represents the height at which the production of turbulence by buoyancy effects equals the production due to wind shear. The formal definition is the following:

$$L = -\frac{u_\star^3 \overline{\Theta}}{\kappa g \overline{(w'\Theta')}_0}, \tag{1.17}$$

where $\overline{\Theta}$ is the mean potential temperature, $\overline{(w'\Theta')}_0$ is the mean temperature flux from the surface, $u_\star$ is the friction velocity and κ is the von Kármán constant.

This length scale is useful to define the different stability conditions. When the heat flux is positive, for example during daytime, the value of L is negative and the boundary layer is unstable. On the contrary, for example during nighttime, the flux changes in sign and L has a positive value. This implies a stable boundary layer. When the temperature flux is null, the Monin-Obukhov length scale becomes infinity, typical for neutral boundary layers. Further considerations about atmospheric stability evaluation are available in appendix B.

1.4 The statistical description of turbulent atmospheric flows

The fluid dynamic owes its fashion and its difficulties to its unpredictable and complex nature. The core of these peculiarities is the turbulence. Even nowadays,

it is not an easy task to give a complete and satisfying definition to the word turbulence.

However, the only way to describe and treat a turbulent flow is by means of a statistical approach, i.e. considering the dynamical and thermodynamical variables as random variables. The flow is divided in a mean component and in a fluctuating component. Keeping the boundary conditions fixed, the mean component is expected to be constant and reproducible. For example, in the atmospheric boundary layer, for a given value of heat transfer to or from the surface, undisturbed wind speed, surface roughness, etc., it is expected to have the same mean quantities.

From a general point of view, consider a generic quantity $u_t(x,t)$ computed or measured inside a volume of interest for which it is available the time series. Consider also a number of fields N for which there is no difference in the boundary conditions. It is possible to compute the following quantities:

- mean: $\overline{u} \equiv \langle u_t \rangle = \lim_{N\to\infty} \left[\frac{1}{N} \sum_{i=1}^{N} (u_t)_i \right]$,
- higher order moments ($m > 1$): $\mu_m = \langle (u_t - \overline{u})^m \rangle \equiv \lim_{N\to\infty} \left[\frac{1}{N} \sum_{i=1}^{N} \left((u_t)_i - \overline{u} \right)^m \right]$.

The statistical moments can be computed from the probability density function $\psi(u_t, x, t)$, when it is known. The contrary is also true, from the statistical moments it is possible to compute the probability density function. The link between the function and the moments is bijective [36].

Among the higher order moments, particular attention is given to the third-order moment, i.e. skewness, and the fourth-order moment, i.e. kurtosis, respectively

$$Sk = \frac{\mu_3}{\mu_2^{3/2}}, \qquad Ku = \frac{\mu_4}{\mu_2^2}. \tag{1.18}$$

The skewness measures the asymmetry of the probability density function while the kurtosis measures the flatness of the probability density function. Reference values are $Sk = 0$ and $Ku = 3$ for the normal or Gaussian distribution.

Temporal and spatial structures

The analysis of inner geometrical structure inside a generic flow can be accomplished by means of spatial auto-correlation functions. Considering a velocity field, in the Eulerian form, decomposed in $u_t = \overline{u} + u'$, the dimensionless form of auto-correlation is

$$c_s(s) = \frac{1}{\sigma_u^2} \langle u'(x) u'(x+s) \rangle, \tag{1.19}$$

which is referred to as auto-correlation coefficient. It is equal to one when $s = 0$ since $\sigma_u^2 = \langle u'(x) u'(x) \rangle$.

In a turbulent flow it is possible to identify a maximum length scale over which the fluctuations of every quantity are uncorrelated. This scale is usually estimated as,

$$\Lambda = \int_0^\infty c_s(s)\, ds, \tag{1.20}$$

and referred to as the Eulerian integral length scale.

The definition of this scale gives geometrical informations about the turbulent structures but not about the timescale. In order to know the life time of turbulent structures it is required to follow them during their evolution. For this analysis, Lagrangian statistics are necessary.

A description of the flow field is given by means of the Lagrangian velocity $v_t = v_t(x,t)$, which can be decomposed in $v_t = \overline{v} + v'$. In analogy with the Eulerian procedure, the Lagrangian auto-correlation coefficient is defined as

$$c_l(r) = \frac{1}{\sigma_v^2}\langle v'(x,t)v'(x,t+r)\rangle, \tag{1.21}$$

and the Lagrangian macroscale or integral scale reads

$$T_L = \int_0^\infty c_l(r)\ dr. \tag{1.22}$$

In Lagrangian models, this time scale governs turbulent relative dispersion and is needed in Gaussian models to calculate the turbulent diffusion coefficient D_t. Moreover, it is used to estimate the convective flux by means of a gradient law and the plume spread downwind the source.

1.5 Dispersion of pollutant in the atmosphere

A wide range of dispersion models of pollutant are available in literature. The main objective is to give a description of the spatial and temporal distribution of the mean concentration field and the deposition of pollutant induced by emission scenarios. The are two available approaches: Eulerian models give a temporal description of statistics at a spatial fixed point, the Lagrangian provide quantities related to particles moving in the fluid.

Among the Eulerian models, it is possible to define the Gaussian model when some hypotheses are taken into account: stationary phenomena, constant diffusion coefficient, constant and uniform wind in the direction of pollutant transport, flat ground, turbulent diffusion neglected compared to pollutant transfer in the streamwise direction. In spite of the simplistic approach of Gaussian models, they are nowadays widely used in main pollutant dispersion numerical codes. In the present work, Gaussian models will be employed.

1.5.1 Phenomenological aspects

Considering the dispersion of pollutant from an elevated source within a homogeneous flow, the process depends mainly on the relative ratio between the length scale of turbulent motion and the characteristic size of the plume.

With this in mind, two different conditions are defined: when the dispersion is caused by turbulent motions associated to spatial scales smaller than plume characteristic length and when the dispersion is caused by bigger scales turbulent motions.

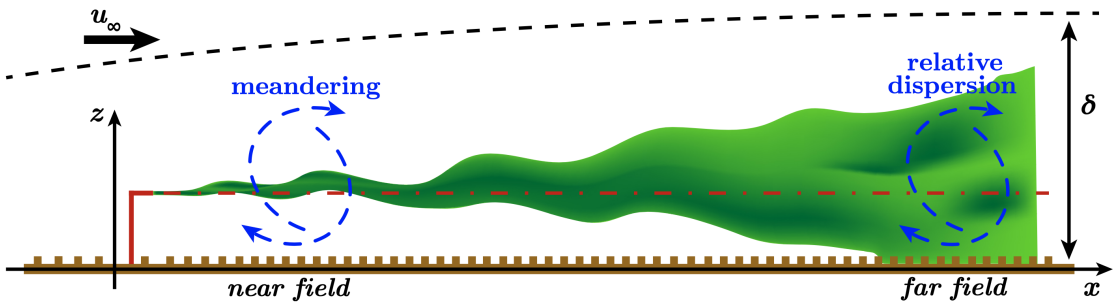

Figure 1.5. Plume dispersion process in a boundary layer.

For the first case, the turbulent dispersion can be treated in analogy with a molecular diffusion process of strong intensity. The spatial dispersion of pollutant is caused by a random motion of fluid parcels, which are considered unrelated.

For the second case it is interesting to study the dispersion process for flight times t smaller than the integral Lagrangian time scale of flow field T_L, defined in equation 1.22, which is associated to the big size of turbulence structures. The process of dispersion can be hence considered a quasi-steady process.

The described limiting conditions are in general unlikely to happen one at a time. Turbulent flows are characterized by a wide range of length scales as in turbulent boundary layers there are both bigger and smaller scales compared to plume characteristic size. The description of this process differs from the one of the standard diffusion process.

However, in the hypothesis of homogeneous turbulence, it is possible to state that the two limiting conditions can be seen as limiting situations of the same diffusion process. When $t/T_L \to 0$, the dispersion is related to a conic shape of the plume and a concentration which varies across the plume section with a law related to the distribution of fluctuating velocities. At the opposite, when $t/T_L \to \infty$ the dispersion process turns into a diffusion process: the plume has a parabolic shape and the concentration is distributed according to the Gaussian distribution across the section. In fact, the plume configuration aims to the Gaussian solution as the time goes on [34].

However, in a real scenario it is in general difficult to verify the action of these limiting conditions. The first limiting condition can be observed only in the proximity of the source where complex phenomena such as mixing with ambient air, jet effect and plume bifurcation makes almost unrealistic the hypothesis that distribution of local velocities is identical to atmospheric velocities distribution. On the contrary, the opposite limiting condition can be matched only very far downstream, usually at distances where the problem of pollution is not critical anymore. Moreover, the measurement of mean values representative for the process would require the flow field to be statistically steady and an extremely long sampling time.

The spread of a plume of pollutant is governed by two phenomena [10]: a

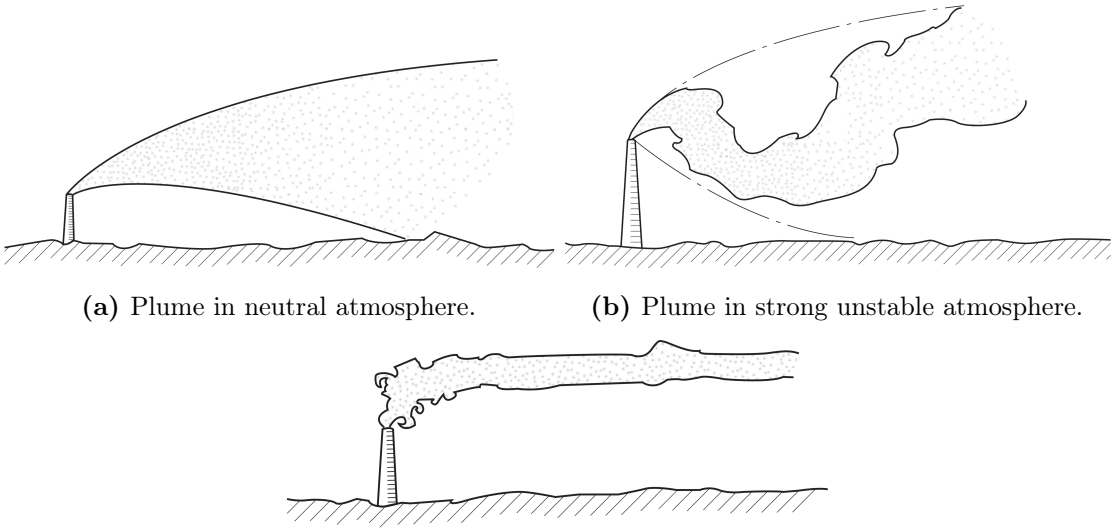

(a) Plume in neutral atmosphere. **(b)** Plume in strong unstable atmosphere.

(c) Plume in strong stable atmosphere.

Figure 1.6. Effects of stability on the plume.

meandering motion of the instantaneous plume, causing the displacement of the center of mass, and the relative dispersion of the plume particles relative to the mass center position. In figure 1.5 a qualitatively description of a plume in a turbulent boundary layer is reported. These phenomena can be considered statistically independent, since they are related to length scales separated by some orders of magnitude. The relative importance of one of the two phenomena depends on the plume size compared to the turbulence scales, at a given distance from the source.

In the near field, if a source having a small size compared to the local turbulence scales is considered, meandering is the major contribution to concentration fluctuations. In this case, the smallest source generates the highest concentration fluctuations. In the far field, the instantaneous plume begins to spread to a dimension comparable to the bigger structures in the flow and develops a fine scale structure also resulting in fluctuations. In these conditions, the meandering motion is almost inexistent and relative dispersion governs plume dispersion. In this case, the effect of the source size on the concentration statistics is negligible.

The stability conditions of the atmosphere play a crucial role in how the pollutant is transferred and how the plume behaves in the boundary layer. A frequently used approach to characterize the stability of the atmosphere is presented in appendix B, which define stability classes according with meteorological conditions. Associated to the classes of atmospheric stability, it is possible to identify peculiar behaviors of the plume. Different plume shapes are identified, as in [5], with different names such as coning for neutral atmosphere, looping for strong unstable atmosphere and fanning for strong stable atmosphere.

Effects of stability on the plume

In general, it is not easy to find the atmosphere in neutral stability conditions. This situation is associated to nighttime fresh breeze or daytime breeze under a

thick cloud cover. In figure 1.6a it is shown a qualitatively behavior of a plume in a neutral atmosphere. It has a conic shape, with an opening angle of about 10-20° [4].

The atmosphere in unstable conditions can be found with light breeze and strong heat flux coming from the ground, such as in a bright sunny day. A convective boundary layer is generated and the plume is transported as shown in figure 1.6b. The dynamic of the plume is dominated by recirculating structures, with the same size of the boundary layer height, generated by ascending hot air masses. The instantaneous shape of the plume shows big spirals and it is highly unsteady.

In this case, there is not a good accordance with the Gaussian model. At the ground it is possible to experience high intermittent concentration values.

The maximum height reached by the plume is fixed by the boundary layer height, which can be considered as a reflecting surface exactly as the ground.

During nighttime, with winds below 2-3 m/s, the turbulent motion is absent or is limited in a small region close to the ground. The plume moves in a fully stratified boundary layer where atmospheric turbulence is suppressed. Following a first phase in which the kinetic energy due to the jet emission is dissipated and the temperature differences between the pollutant and the air are leveled out, the dispersion process can be considered completed. The plume is dragged downwind like a compact streak, with small drifts or oscillations. The situation is shown in figure 1.6c. During this phase, no deposition of pollutant reaches the ground unless it descends due to gravity.

1.5.2 Mathematical models

In the present work, the concentration field of pollutant diluted in turbulent boundary layers is modeled as a passive scalar [37]. It is expressed as $c(x_j, t)$ and considered as a random variable decomposed in a mean and a fluctuating component. A full characterization of the concentration field requires a multi-point, multi-time probability density function but it is in general unfeasible to evaluate. In a more practical manner, it is possible to evaluate only the one-point one-time probability density function of concentration to obtain a statistical description of concentration field in a specific position and time, independently from other points, both in space and in time [17].

Dispersion models based on the Reynolds average concept are able to characterize the first order moment of the concentration probability density function. This is satisfactorily when the process considered (from a wide broad of fields such as physical, chemical or biological) is linearly dependent on the concentration. However, a non-linear behavior is often observed in many interesting cases such as releases of toxic and flammable substances. In these cases, it is necessary to know the second or higher order moments of probability density function of the concentration.

The convection-diffusion equation of the concentration is expressed as follows

$$\frac{\partial c}{\partial t} + u_j \frac{\partial c}{\partial x_j} = D \frac{\partial^2 c}{\partial x_j^2}, \tag{1.23}$$

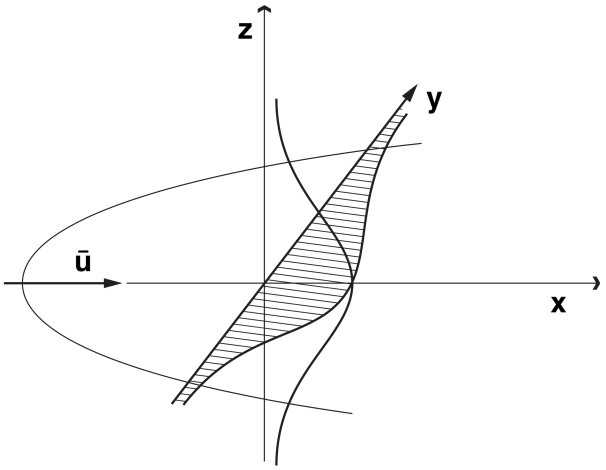

Figure 1.7. Gaussian model of dispersion.

where D is the molecular diffusion coefficient. Applying Reynolds decomposition both to concentration and velocity fields, i.e. $c = \overline{c} + c'$ and $u_j = \overline{u}_j + u'_j$, and averaging equation 1.23, the evolution equation of mean concentration is obtained:

$$\frac{\partial \overline{c}}{\partial t} + \overline{u}_j \frac{\partial \overline{c}}{\partial x_j} = \frac{\partial}{\partial x_j}\left(D \frac{\partial \overline{c}}{\partial x_j} - \overline{u'_j c'} \right). \tag{1.24}$$

The correlation $\overline{u'_j c'}$ represents the coupling between velocity and concentration fluctuations and makes the problem unsolvable. The standard closure procedure consists in modeling this term considering it proportional to mean concentration spacial gradient as follows

$$\overline{u'_j c'} = -D_{t,j} \frac{\partial \overline{c}}{\partial x_j}, \tag{1.25}$$

where $D_{t,j}$ is the turbulent diffusion coefficient. This coefficient appears to be similar to molecular diffusivity D but it differs for its higher order of magnitude. For this reason, the molecular diffusion can be neglected and equation 1.24 becomes

$$\frac{\partial \overline{c}}{\partial t} + \overline{u}_j \frac{\partial \overline{c}}{\partial x_j} = -\frac{\partial}{\partial x_j} \overline{u'_j c'}. \tag{1.26}$$

Under the hypotheses necessary to introduce the Gaussian model, presented in section 1.5, and considering x as the stream-wise direction, equation 1.26 simplifies in

$$\overline{u} \frac{\partial \overline{c}}{\partial x} + \frac{\partial \overline{w'c'}}{\partial z} + \frac{\partial \overline{v'c'}}{\partial y} = 0, \tag{1.27}$$

.

Applying the definition in equation 1.25, the last equation reduces to

$$\overline{u} \frac{\partial \overline{c}}{\partial x} = D_{t,y} \frac{\partial^2 \overline{c}}{\partial y^2} + D_{t,z} \frac{\partial^2 \overline{c}}{\partial z^2}, \tag{1.28}$$

where $D_{t,y}$ and $D_{t,z}$ are the turbulent diffusion coefficients along the lateral and vertical direction.

It admits an analytical solution, i.e.

$$\overline{c}(x,y,z) = \frac{\dot{M}_q}{4\pi\sqrt{D_{t,y}D_{t,z}}} \exp\left[-\frac{\overline{u}}{4x}\left(\frac{y^2}{D_{t,y}} + \frac{(z-h_s)^2}{D_{t,z}}\right)\right], \tag{1.29}$$

where $\dot{M}_q$ is the pollutant mass flow and h_s is the height of the source. A graphical visualization of the analytical solution is given in figure 1.7.

Considering the dynamic of the second order moment of concentration, expressed in terms of concentration variance σ_c^2, molecular diffusion processes are not negligible [23]. The equation reads

$$\frac{\partial \sigma_c^2}{\partial t} = -\frac{\partial}{\partial x_j}\left(\overline{u}_j\sigma_c^2 + \overline{u_j' c'^2} - k\frac{\partial \sigma_c^2}{\partial x_j}\right) - 2\overline{u_j' c'}\frac{\partial \overline{c}}{\partial x_j} - 2D\left(\frac{\partial c'}{\partial x_j}\frac{\partial c'}{\partial x_j}\right), \tag{1.30}$$

where the first terms of the left-hand side are fluxes from convective and diffusive origins, the second term is the production term of variance while the last term expresses the dissipation rate ε_c of the variance.

Chapter 2

Wind tunnel and experimental setup

2.1 Wind tunnel description

The experiments have been performed in the EnFlo Lab Wind Tunnel at the University of Surrey. This is an open-circuit wind tunnel specifically designed for environmental fluid dynamic experiments. Figure 2.1 shows an overview of the wind tunnel.

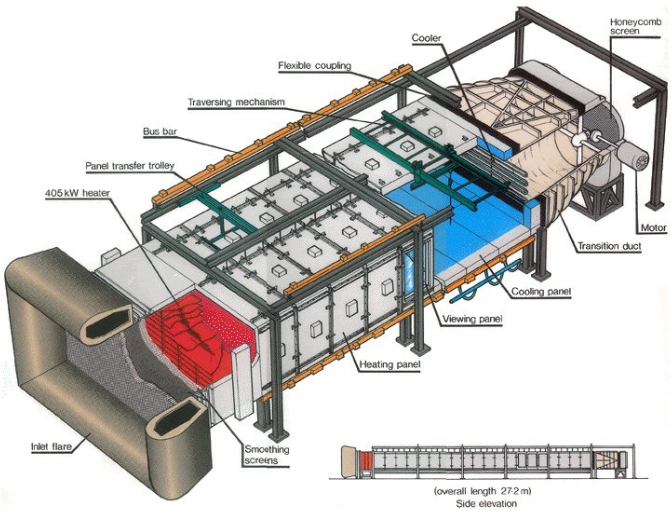

Figure 2.1. EnFlo Wind Tunnel.

The engine of the wind tunnel is connected to twin fans and it works via suck through. The overall length is 27.2 meters and the working section is 20L x 3.5W x 1.5H m. The airspeed range goes from 0.3 m/s to 3 m/s.

In order to reproduce the atmospheric boundary layer and turbulence, two main devices are used: spires and roughness elements. At the inlet of the test section, seven spires of 986 mm height are separated by 500 mm each along the lateral direction. These spires are truncated Irwin-type spires [14]. They are mainly used to reproduce atmospheric boundary layers onshore. Figure 2.2 shows the spires

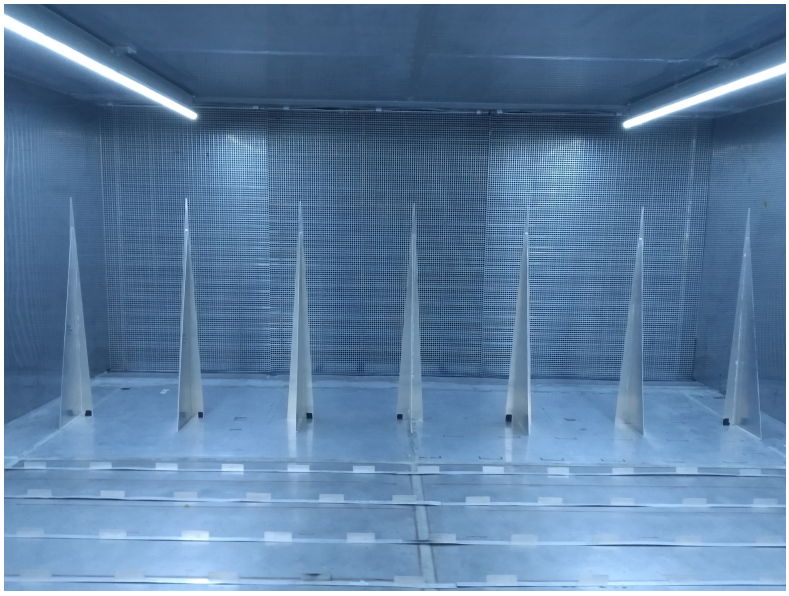

Figure 2.2. Irwin spires and roughness elements.

disposition at the inlet of the working section.

Moreover, roughness elements are placed all over the test section floor. They are rectangular-shaped elements 20 mm high and 80 mm wide. They are staggered, with a longitudinal and a lateral spacing of 240 mm.

2.1.1 Stable boundary layer generation

The stratified boundary layer and its different stability conditions are obtained through a specific temperature profile at the inlet of the test section and cooling the wind tunnel floor.

The temperature profile at the inlet is imposed with 15 heaters, each formed by a group of 9 tubes. Each group is spaced by 0.1 m along the vertical direction. The maximum temperature gradient which can be imposed is 80°C/m.

Moreover, the sidewalls of the test section are heated as well to help the inlet heater keep the correct vertical temperature gradient for all the testing section length. The sidewalls are formed with three levels of covers, through which the temperature gradient can be imposed.

The correct temperature imposition, i.e. temperature at the inlet, temperature of the floor and temperature for the sidewalls, is given by previous studies such as performed at the EnFlo Lab [19], [20].

In this work, two conditions of stability are considered, in addition to one neutral condition taken as reference. The stability condition is imposed by the temperatures set in the wind tunnel and the reference speed U_{ref}. The latter is imposed via a feedback loop on the wind tunnel engine measuring the test section speed with a reference ultrasonic anemometer located above the boundary layer, close to the test section inlet. Figure 2.3 shows the two temperature profiles used to impose the two stability conditions.

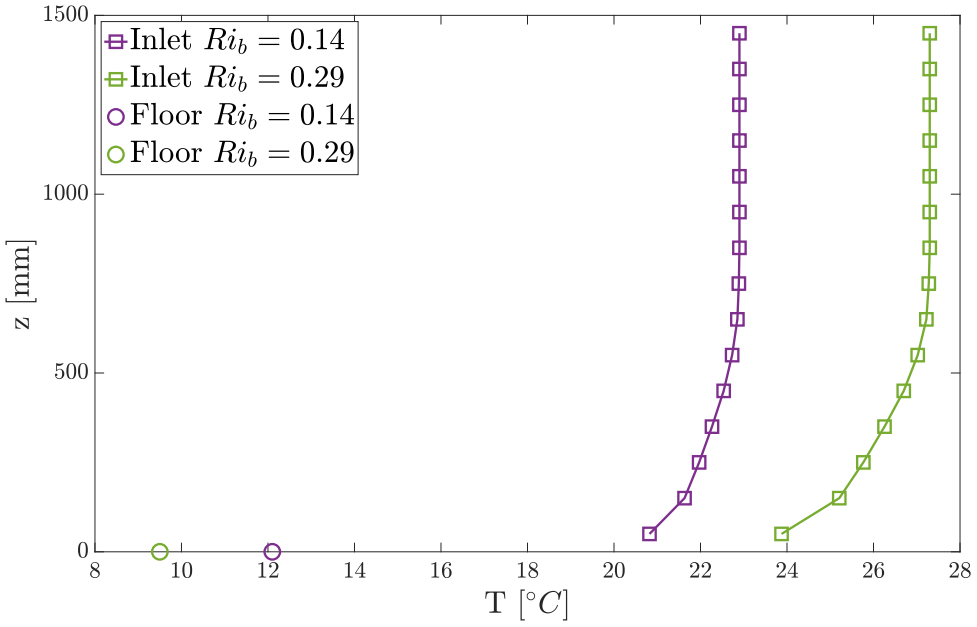

Figure 2.3. Temperature profiles at the inlet of test section and floor temperature.

The stratification strength is imposed through the value of $\Delta\Theta_{max}$, which is the difference between the maximum value of temperature imposed at the inlet and the floor temperature. The strongest boundary layer in terms of stability has been performed with a reduced reference wind speed of 1.15 m/s. This reduction of speed, with the increase of temperature difference, was found to be the best compromise in order to have a sufficiently high Reynolds number and not to cause overheating of the LDA probe.

In table 2.1, the imposed stability parameters are reported. The Ri_b^{app} is the desired bulk Richardson number which is often slightly different form the actual measured one, here indicated as Ri_b. In what follows, only the applied bulk Richardson number Ri_b^{app} will be used to label the different stability conditions. The Reynolds number is defined as $Re_\delta = \delta U_\delta/\nu$, where ν is the air kinematic viscosity at floor temperature Θ_0 and U_δ is the stream-wise speed at boundary layer height δ. For the neutral case, the floor temperature has not been imposed so the value of ambient air temperature of about 20°C is considered. The Monin-Obukhov length L is computed as in equation 1.17.

The reference speed U_{ref} differs from U_δ since they are defined in different ways. The reference speed is used to impose a reproducible condition inside the wind tunnel, measured close to the inlet. The speed U_δ is evaluated further downstream where measurements have been performed as explained in section 2.2. Here, the free flow is slightly accelerated due to the formation of lateral boundary layers.

In order to produce a stable boundary layer, it would have been easier to impose a uniform inlet temperature and make the stability grow thanks to the cooling effect of the floor of the test section. The problem is that, in this configuration, it has been proved that the upper part of the boundary layer remains unaffected

Ri_b^{app}	0	0.14	0.29
Ri_b	0	0.12	0.24
$\Delta\Theta_{max}$ [°C]	0	10.8	17.8
U_{ref} [m/s]	1.25	1.25	1.15
U_δ [m/s]	1.31	1.32	1.23
Θ_0 [°C]	20	12.1	9.5
L [mm]	∞	1272	600
δ [mm]	850	850	850
Re_δ	$7.39{\cdot}10^4$	$7.82{\cdot}10^4$	$7.40{\cdot}10^4$

Table 2.1. Boundary layer parameters.

by the stratification. The mean temperature remains constant with height, while temperature fluctuation and heat fluxes approach zero at lower heights than the Reynolds shear stress [19].

2.2 Instrumental setup

For the purpose of this work, measurements of concentration, temperature and velocity are taken simultaneously in the plume of tracer injected in a fully developed turbulent boundary layer from an L-shaped elevated source. Figure 2.4 shows the experimental layout.

The instruments employed are the following: cold wire (CW) for temperature, Fast FID (FFID) for concentration and two-component Laser Doppler Anemometer (LDA) for velocity. The general layout is similar the one already employed in [18].

Instruments are fixed to an automatic movable traverse. The goal is to measure the flow and concentration quantities in the same measurement volume, given by the intersection of LDA lasers. For obvious problematic interaction between lasers and CW or FFID, the former two are kept fixed in a position 4 mm downstream with respect to the measurement volume.

The LDA is kept horizontally by a fixed arm in order to measure the u and w components of velocity. The seeding for the LDA is performed with a solution of tap water and sugar, vaporized by an ultrasonic humidifier [18]. The seeding takes place from the top of the wind tunnel, in a recirculating region of the laboratory.

Typical acquisition rates for the instruments are about 100 Hz for the LDA, 400 Hz for the cold wire and 1000 Hz for the FFID.

The acquisition time is fixed at 5 minutes in order to obtain a proper description of the turbulent phenomena. In particular, the most strict condition on convergence is given by the fourth order moment, i.e. kurtosis, of concentration. The convergence of the kurtosis of concentration at the center-line of the plume at source height is shown in figure 2.5.

The measurements have been performed at different stations along the streamline direction, as shown in table 2.2. Two different reference systems are employed. The

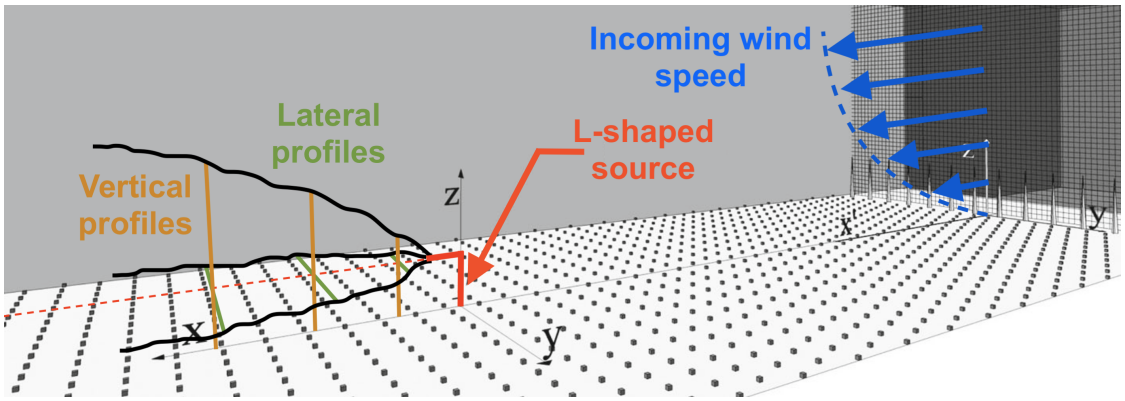

Figure 2.4. Experimental layout.

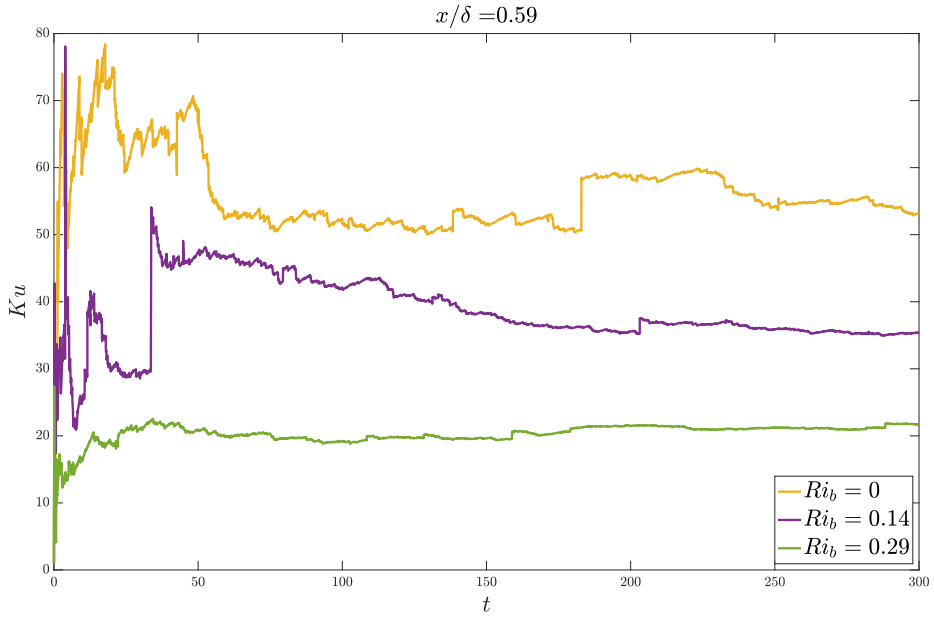

Figure 2.5. Convergence of kurtosis of concentration.

Stations	Station position [mm]
1	250
2	500
3	1000
4	2000
5	3000
6	4000
7	4797

Table 2.2. Measurement stations along x direction.

Source	Inner diameter	Outer diameter	X position	Z position
1	6	8	12200	161.5
2	3.1	5	12090	161.5

Table 2.3. Source details in millimeters.

wind tunnel reference system has the origin at the beginning of test section, in center line at the floor. The x axis points in the stream direction, z axis points upward and the y axis following standard rule. The source reference system is translated just along the x axis, with the origin of x axis which coincides with source origin. Two sources have been used for the experiments. Characteristics are reported in table 2.3. The x position of the source has to be intended as the longitudinal position of the opening of the L-shaped tube. This position is the longitudinal origin of station positions in table 2.2.

At each longitudinal station, both vertical and transverse profiles have been measured. Transverse profiles are measured at source height while vertical profiles are measured at the lateral coordinates where maximum concentration value has been measured. Since the extension of the plume is unknown a priori, the measurements are performed along the given direction (either lateral or vertical) until the mean concentration signal drops to a value equal or below the 2% of the maximum value measured in that configuration.

The run of the wind tunnel and the data acquisition system is controlled by a LabView code developed by the EnFlo Lab staff. The analysis of the data is performed using Matlab codes.

2.2.1 Fast FID

The concentration is measured by means of a fast response flame ionization detector, or Fast FID, [7]. It works through the detection of ions produced during the combustion of carbon compounds in a hydrogen flame. The ions are collected by an electrode negatively based at 150-200 V. The chemical reactions undergoing this process are complex but they can be synthesized as $CH + O = CH^+ + e^-$. The number of ions produced is proportional to the concentration of the carbon components inside the measured stream flow. In this work, the propane has been used as tracer gas. To guarantee a constant mass flow rate of tracer, a constant-

pressure chamber is employed inside the instrument.

The calibration is performed by measuring the concentration of fixed and well known gases in order to produce a calibration curve which is typically linear. This process is performed regularly during the data acquisition. After the calibration, the background propane concentration in the wind tunnel has been also measured and the value of the noise has been subtracted to the measured concentration.

The instrument is equipped with a small tube, 0.3 mm in diameter, which takes a small amount of air and tracer inside the instrument body where the flame burns. Due to this, in general, there is a delay time between the measurement and the FID output. This delay time has been measured to be around 0.003 s. This value has been obtained in the preliminary phase of the experiments. The source has been employed as a hot jet and the instruments have been located just in front of it. The delay time has been obtained with convolution between the signals; it means having peaks of velocity, concentration and temperature at the same time.

The propane diluted in air is released by the source with a different percentage of tracer according to the position of measurements. In the measurement stations close to the source, the percentage of tracer is kept low to avoid saturation of FID and to keep below flammable limit. In the far flow, the percentage is higher in order to measure a signal strong enough to be relevant between background noise. For safety reasons, the maximum percentage of propane in the air was fixed to 1.8%.

2.2.2 Cold wire

Cold wire is an instrument used to detect temperature variations and its fluctuations. The setup is a classical thermal anemometry setup with a small cylindrical wire kept in position by prongs. The cold wire was a Dantec Dynamics (55P11) miniature wire probe. This has been used with a high frequency rate of 400 Hz in order to correlate the signal with velocity components signals and compute the heat fluxes. The calibration of the cold wire has been done with a thermistor placed just next to the cold wire.

2.2.3 Laser Doppler Anemometer

The Laser Doppler Anemometer or LDA is an instrument widely used in wind tunnel test facilities. It is used to measure up to three velocity components using the Doppler effect with laser beams. The Doppler frequency gives a measure of velocity magnitude. By means of shifting and multi frequency beams, it is possible to measure all velocity components. In order to perform measurements, it is necessary to seed the flow inside the wind tunnel. A wide variety of seeding particles and seeding techniques are available nowadays. The Doppler frequency is measured by the light scattered from the particles moving in the flow and hit by the laser beams. Typical LDA configuration is composed by laser generator, Bragg cell, beam color splitter and one or two probes.

For the purpose of this work, a two-component LDA has been used to measure mean and fluctuating velocity components in a single point. In particular, it allowed to measure, in two different configurations, both longitudinal-vertical and longitudinal-lateral components, namely uw and uv.

The laser was a Coherent Genesis MX-STM laser equipped with a 40 MHz Bragg cell. The two lasers employed were a green laser with 513.6 mm wavelength and a blue laser with 488 mm wavelength. A Dantec Dynamics 27 mm fiber-probe has been adopted to convey the two lasers. The measuring volume had a diameter of 0.049 mm. The nominal acquisition rate for the LDA is fixed at 100 Hz but the real value varies according to seeding rate. The value of 100 Hz is fixed as target and the seeding in controlled by a feedback closed loop. The range of LDA acquisition frequencies has been obtained to be from about 50 Hz close to the ground, where the flow velocity is low, to about 150 Hz in the upper part of the boundary layer.

From the LDA system, statistics of velocity computed by measurements are highly dependent on the velocity of particles passing through the control volume. In general, there will be a tendency to have higher statistics where the flow velocity is higher. To avoid this kind of bias, mean and higher-order averages are obtained using the transit times as weighting values.

Moreover the two components of velocity were actually not measured with the same frequency rate. For this reason, a resampling was necessary when correlation between the two components was computed, or when correlation between velocity and concentration field is analyzed.

Chapter 3

Flow field

3.1 Introduction

The first step for the analysis of the data collected at the EnFlo Lab is to characterize the velocity field in which propane is injected. To that purpose, a series of measurements of velocity and temperature has been performed. These data have been analyzed along side data of previous studies at the EnFlo Lab presented in Marucci and Carpentieri (labeled M & C 2018) [19]. Three specific cases have been selected: the neutral case and two stable cases, respectively with a Richardson bulk number of 0.14 and 0.21. The parameters of the flow field are reported in table 3.1, where the experiments performed for the purpose of this work and presented in chapter 2 are referred to as *Surrey experiments*.

3.2 Mean flow analysis

Firstly, the vertical profiles of the mean longitudinal velocity are analyzed and are shown in figure 3.1. Data have been normalized with U_δ, the longitudinal velocity at the limit of the boundary layer referred to as δ. More specifically, this is defined from vertical profiles and it is the 99% of the maximum velocity measured. In this way, also an evaluation of the boundary layer height δ is obtained, i.e. the height where U_δ is defined. The profiles are plotted for different longitudinal

	M & C 2018			**Surrey experiments**		
Ri_b [-]	0	0.14	0.21	0	0.14	0.29
$\Delta\Theta_{max}[K]$	0	10.8	16	0	10.8	17.8
U_δ [m/s]	1.30	1.31	1.33	1.31	1.32	1.23
$u_\star$ [m/s]	0.081	0.066	0.059	0.073	0.054	0.049
z_0 [mm]	2.2	2.3	2.3	1.3	0.7	1.8
$\vartheta_\star$ [K]	-	0.24	0.34	-	0.24	0.39
L [mm]	∞	1350	752	∞	1272	600
δ [mm]	850	850	850	850	850	850

Table 3.1. Flow field parameters.

stations and they show a good agreement between the different cases.

In the following figures, the data identified with a cross and the label M&C are the data obtained by Marucci and Carpentieri (2018) [19] while data represented with a circle are measurements of the experimental campaign presented in this work.

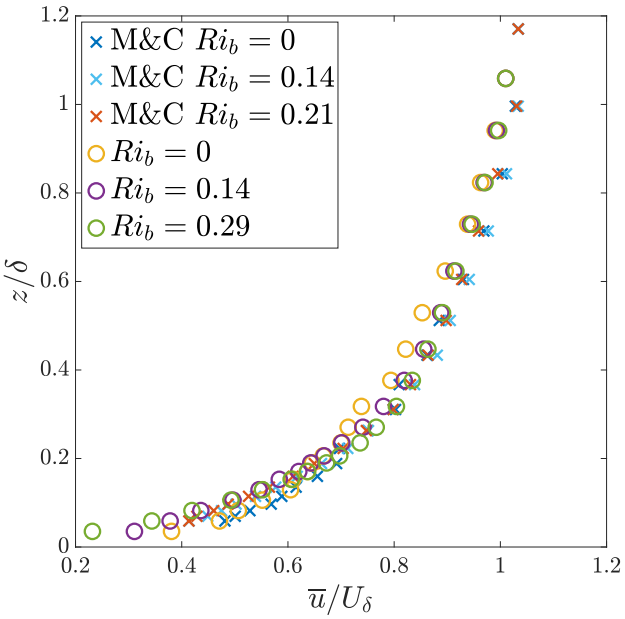

Figure 3.1. Vertical profiles of longitudinal velocity.

It is well known that a turbulent boundary layer can be described, at least in a region close to the wall, by means of similarity relations. The flow field in this region can be characterized by only one length scale z and one velocity scale $u_\star$. In studying a stratified boundary layer, or in general the atmospheric boundary layer, there are heat fluxes which must be taken into account in the description of the the flow. In this trend, the general form valid in the surface layer is the following:

$$\varphi_m(\zeta) = \frac{\kappa z}{u_\star}\frac{\partial U}{\partial z}, \tag{3.1}$$

where k is the von Kármán constant set to 0.41 and $u_\star$ is the friction velocity. The right-hand side function has, as variable, a non-dimensional length scale which is used as stability parameter. It has been defined in the Monin-Obukhov theory, [25] and [22], as

$$\zeta = \frac{z}{L} = -\frac{\kappa z \vartheta_\star}{u_\star^2 \Theta_0}, \tag{3.2}$$

where L is the Monin-Obukhov length, $\vartheta_\star = -\overline{w'\Theta'}/u_\star$ and Θ_0 is the reference temperature at the ground.

The equation 3.1 has to be integrated between the roughness height z_0, defined as the height close to the wall where the analytic velocity profile is null, and a generic height z. The integration of the universal function is computed for stable

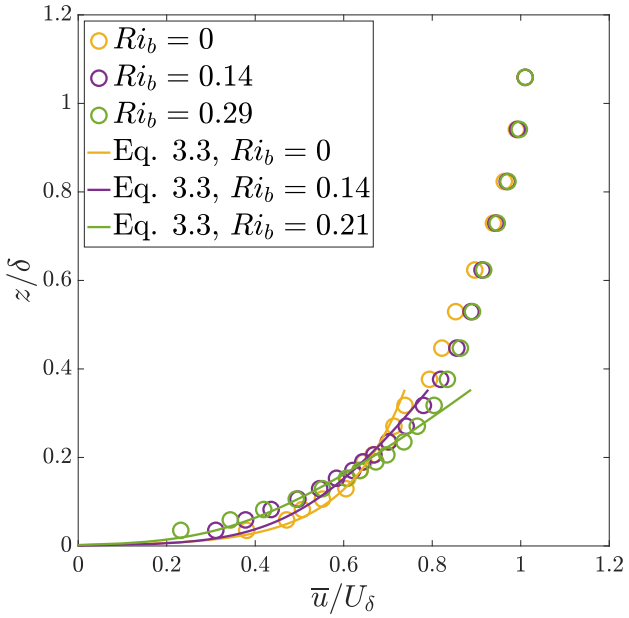

Figure 3.2. Vertical profiles and analytical solution in the surface layer.

boundary layers considering $\varphi_m = 1 + 8\zeta$, which has been used by [19] and obtained by fitting the non-dimensional gradient from experimental data. The well-known logarithmic expression is eventually obtained, valid for stable cases or neutral cases neglecting the last term:

$$U(z) = \frac{u_\star}{\kappa}\left[\ln\left(\frac{z-d}{z_0}\right) + 8\frac{z-d-z_0}{L}\right]. \tag{3.3}$$

Figure 3.2 shows the logarithmic law for each stability condition considered, along side the experimental data. In the present work, the displacement height d is fixed to 0.

3.2.1 Estimation of surface properties

There is not a universal procedure to compute the surface proprieties of boundary layers. The friction velocity is defined as follows $u_\star = \sqrt{-(\overline{u'w'})_0}$ where $(\overline{u'w'})_0$ are the cross-Reynolds stresses at the wall. In the present work, the mean of the first three measured values of $\overline{u'w'}$ closer to the ground have been considered [19].

A similar procedure has been adopted to estimate the scaling temperature $\vartheta_\star = -(\overline{w'\Theta'})_0/u_\star$, computing the mean of the first three measured values of $\overline{w'\Theta'}$.

The value of z_0 has been then determined by a best fit performed between experimental data and equation 3.3 in the lower part of the boundary layer, from the first measured point at 30 mm until about 300 mm in the vertical direction.

3.3 Fluctuating flow

The main purpose of this section is the analysis of the Reynolds stresses and of the turbulent heat flux profiles.

Vertical profiles of $\overline{u'u'}$, $\overline{w'w'}$ and $\overline{u'w'}$ which are shown in figure 3.3 together with the heat flux $\overline{w'\Theta'}$.

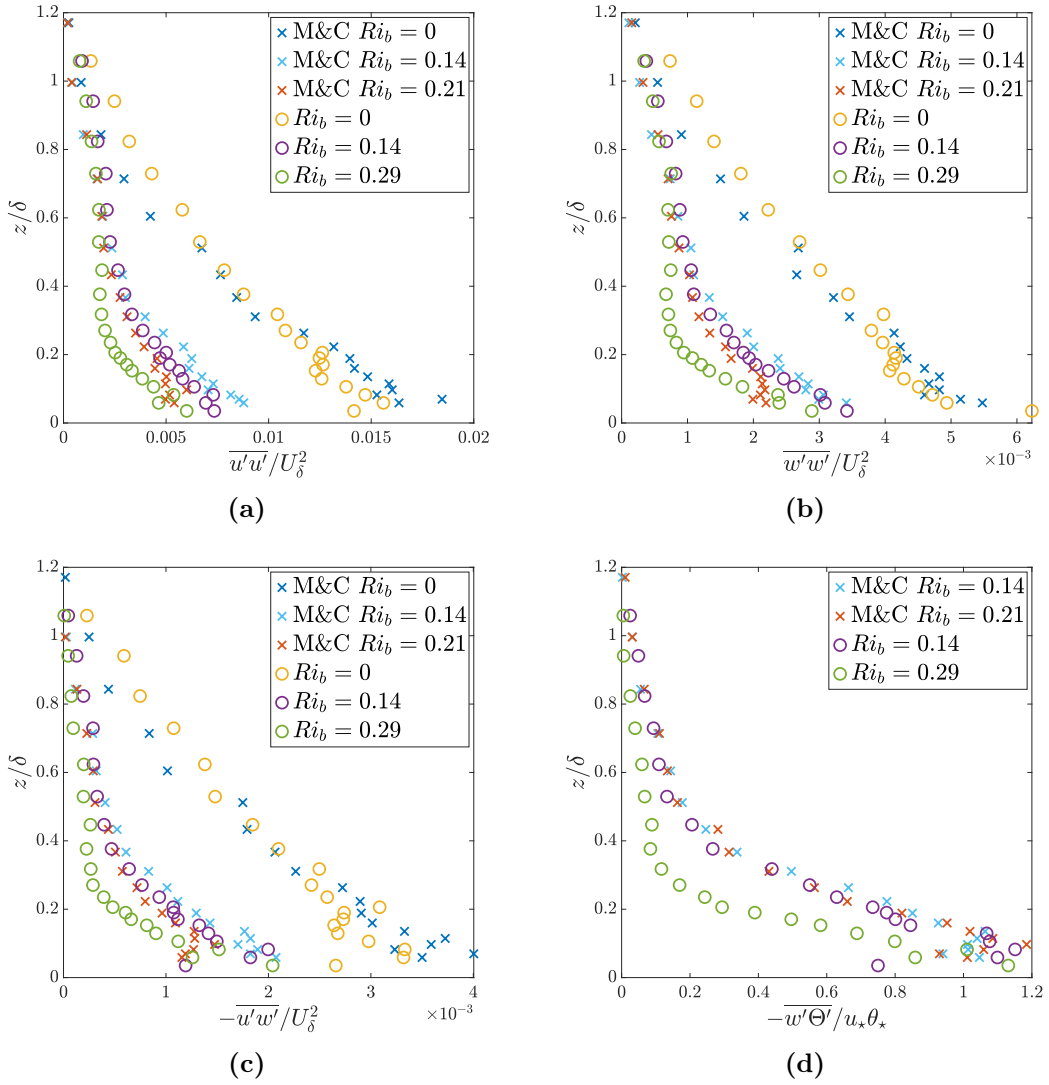

Figure 3.3. Vertical profiles of Reynolds stresses and kinematic heat flux.

From the Reynolds stress profiles, it is possible to verify that the thermal stability acts in suppressing turbulent fluctuations. In fact, the higher the Richardson number, the lower the variances of fluctuations components. The action of the temperature gradient will be further discussed when analyzing the turbulent kinetic energy budget in section 3.5.

In the surface layer, the velocity field can be rescaled by means of two appropriate scales, i.e. the Monin-Obukhov length L and the friction velocity $u_\star$, see section 3.2.1. Rescaling the Reynolds stresses and the kinematic heat flux reveals the existence of a region, close to the ground, where the profiles coincide. Results are

shown in figure 3.4. A good agreement in the data can be seen for all measured profiles except for those obtained by Marucci and Carpentieri with a Richardson number of 0.21. This divergence is likely to be due to the uncertainty in the evaluation of the length and velocity scales, which could cause this small drift in the rescaled profiles.

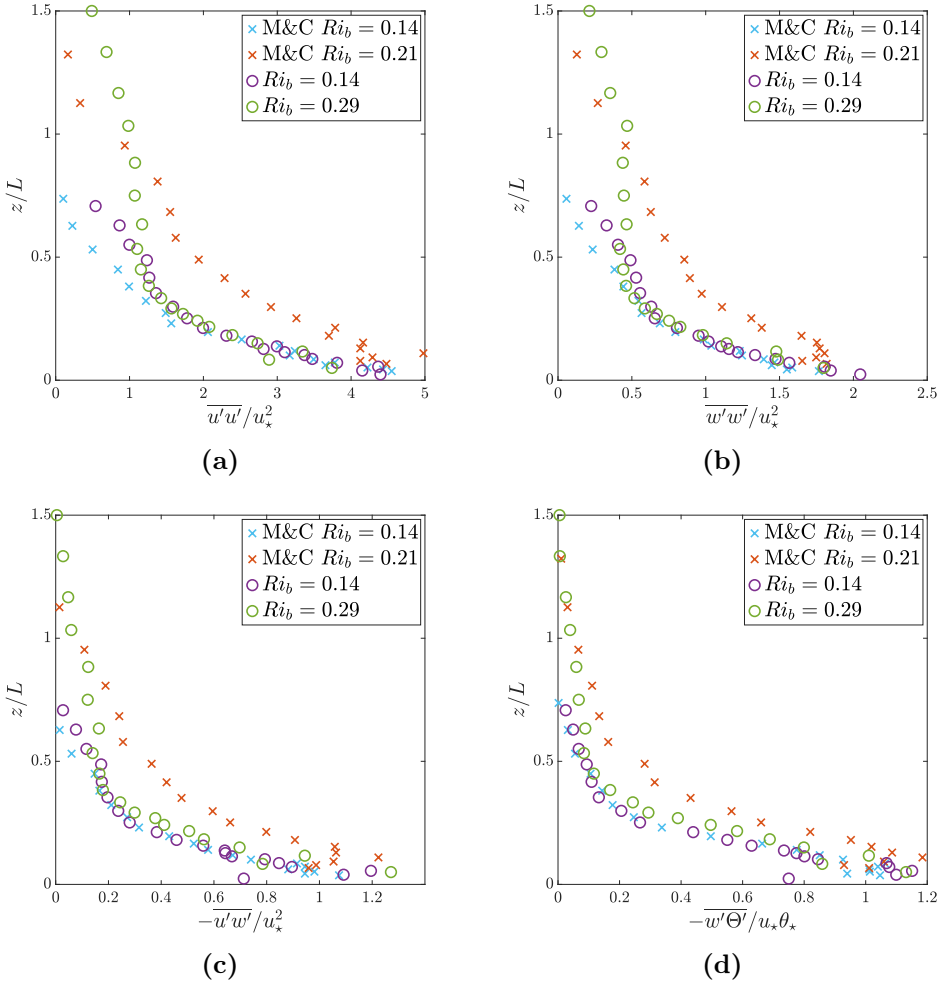

Figure 3.4. Rescaled Reynolds stresses and kinematic heat flux.

3.4 Velocity spectra

The spectrum of velocity is a powerful tool to study a turbulent boundary layer. It is computed as $E(k)$ and represents the contribution to turbulent kinetic energy associated to turbulent structures with a wavenumber between k and $k + dk$. Since experimental data are available only in time domain, the wavenumber k is obtained by means of Taylor's frozen turbulence as $2\pi f/\overline{u}$ where f is the frequency. Moreover, it is important to consider the following relation, [15],

$$kE(k) = fS(f), \tag{3.4}$$

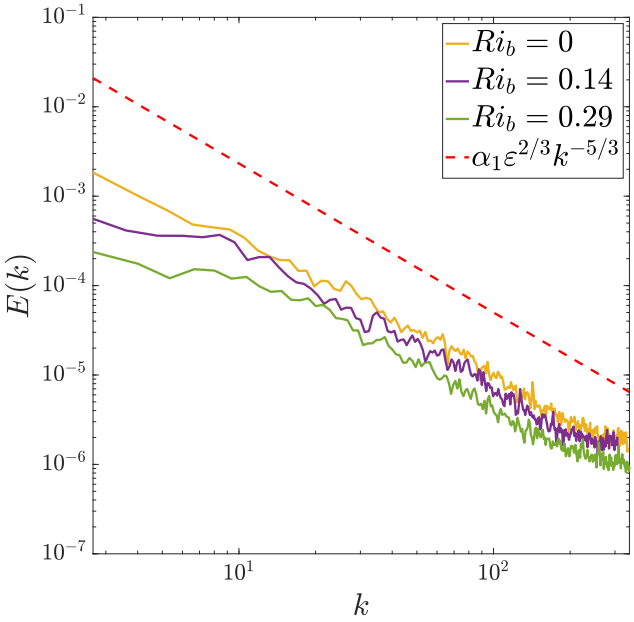

Figure 3.5. Velocity spectra of longitudinal component at source height $z/\delta = 0.19$.

in order to plot spectra in different spaces.

According to Kolmogorov's theory of 1941, in the hypothesis of homogeneous and isotropic turbulence, three ranges exist in the wavenumber space: the energy-containing range associated with the production of energy by buoyancy or shear, the inertial subrange where energy is transferred from bigger scales to smaller scales and the dissipation range, where energy is converted in internal energy by viscosity. In the inertial subrange the velocity spectra are proportional to $\alpha_1 \varepsilon^{2/3} k^{-5/3}$ as shown in figure 3.5, where $\alpha_1 = 0.5$ according to [29].

In order to have an estimation of turbulent kinetic energy dissipation rate, a fitting of longitudinal velocity spectra has been performed. This estimation, from now denoted as ε_{sp}, is shown in figure 3.6 in non-dimensional form.

3.5 Turbulent kinetic energy budget

The balance of turbulent kinetic energy, assuming steady conditions and neglecting the molecular viscous transport, reads

$$\overline{u}_j \frac{\partial}{\partial x_j} k + \frac{\partial}{\partial x_j} \left[\left(\frac{1}{2} \overline{u'_j u'_i u'_i} \right) + \frac{1}{\rho_0} \overline{u'_j p'} \right] = P_m - \varepsilon + \frac{g}{\rho_0} \overline{\rho' u'_i} \delta_{i3}, \tag{3.5}$$

with $k = \overline{u'_i u'_i}/2$ as the turbulent kinetic energy. The terms in the equation are respectively the advection term, the transport by means of velocity fluctuations, the pressure diffusion term, the production, the mean dissipation rate and the buoyancy flux.

The production term related to mean shear flow, assuming an horizontally homogeneous boundary layer, is approximated as

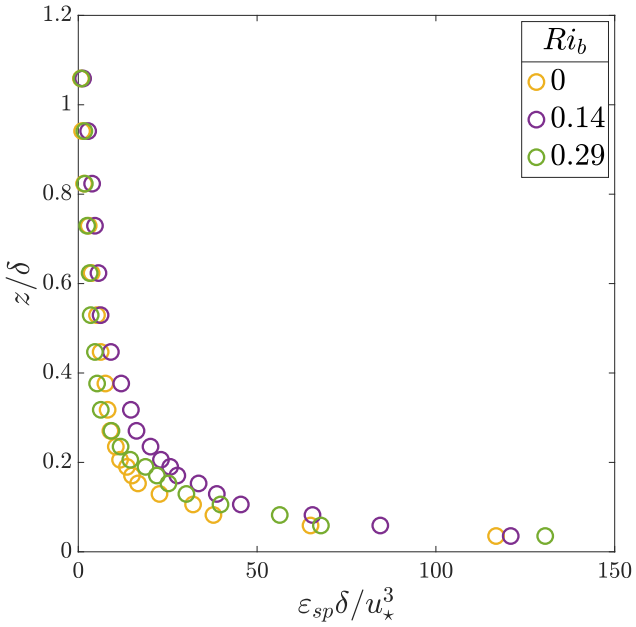

Figure 3.6. Vertical profiles of mean dissipation rate by means of spectra.

$$P_m = -\overline{u_i' u_j'} \frac{\partial \overline{u_i}}{\partial x_j} \approx -\overline{u'w'} \frac{\partial \overline{u}}{\partial z}. \tag{3.6}$$

In the study of stratified boundary layers, the buoyancy term can act both as buoyant production or dissipation of turbulent kinetic energy. It is related to the heat flux caused by temperature gradients along the vertical direction. In an unstable case, in which the mean temperature $\overline{\Theta}$ decreases upward, the heat-flux correlation $\overline{w'\Theta'}$ is positive (upward), signifying that the turbulence is generated convectively by upward heat fluxes. In a stable case, the heat-flux correlation is negative and the turbulence is suppressed by stratification. The term can be expressed in terms of temperature considering that a variation in density is caused only by a variation in temperature:

$$P_t = -\frac{g}{\Theta_0} \overline{w'\Theta'}. \tag{3.7}$$

Vertical profiles of production term is show in 3.7a while suppression terms in figure 3.7b. The latter terms are small compared to production due to mean shear effect.

3.6 Integral length scales

Inside the turbulent motion of the flow, it is possible to find turbulent length scales which give approximated extension of the turbulent structure. In particular, these scales express the maximum length over which a velocity signal does not show a correlation to the velocity signal where the length scale is measured or computed. In general, turbulent length scales are difficult quantities to measure. The integral

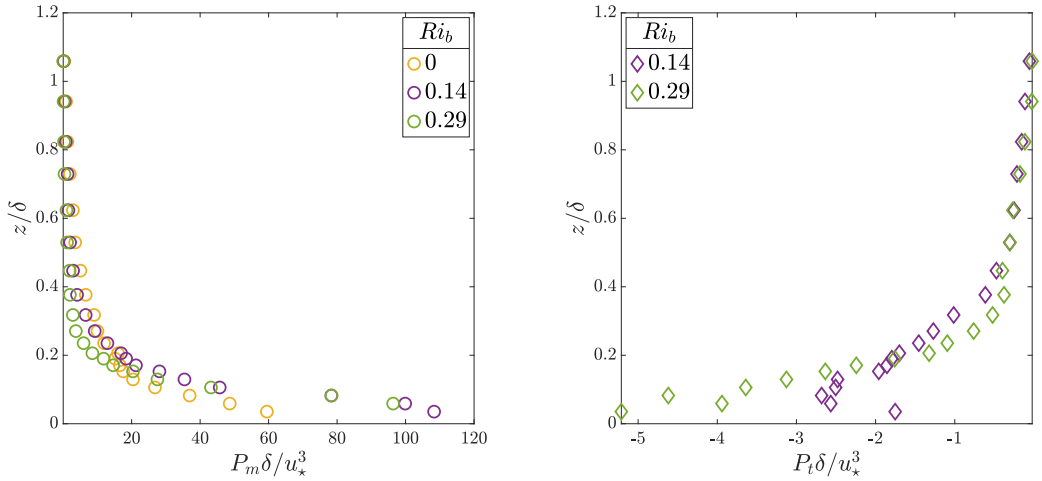

(a) **(b)**

Figure 3.7. Production and suppression terms of TKE.

length scales are obtained by means of numerical integration of auto-correlation coefficient of velocity signal. According to [9], the coefficient has been integrated until it drops to a value of 0.05 and Taylor's hypothesis of frozen turbulence has been used to convert timescale to length scales. Namely:

$$T_E(z) = \int_0^\infty \rho_E(z,\tau)\, d\tau, \tag{3.8}$$

$$\Lambda(z) = T_E(z) \cdot \overline{u(z)}, \tag{3.9}$$

where $\rho_E(z,\tau) = \overline{u_i'(t)u_i'(t+\tau)}$ referres to the u_i' component of velocity field. In this study, velocity components $u(t)$ and $w(t)$ have been analyzed and studied to find length scales.

Length scales are shown in figure 3.8 and 3.9. For the vertical case, among data from Marucci and Carpentieri [19], two other references have been introduced for the neutral stability case. The dotted line is the linear model, viz.

$$\frac{\Lambda_w}{\delta} = 0.4\frac{x}{\delta}, \tag{3.10}$$

which appears to work properly in the region closer to the ground for the neutral case. The square marks refer to experimental data in [30]. In both streamwise and vertical scales, there is difference between neutral and stable cases but it not possible to clearly distinguish the effect of stability.

The approach here presented is an Eulerian approach. The length scale is evaluated by a fixed point measurement so the statistical description of the turbulent structures is obtained analyzing the signal by means of autocorrelation in time as previously explained.

The Eulerian time and length scales do not give a complete description of the extension or the lifetime of turbulent structures. A better procedure will require the evaluation of Lagrangian scales, defined in equation 1.22. These scales are important parameters in the modeling of pollutant dispersion but they are extremely complex

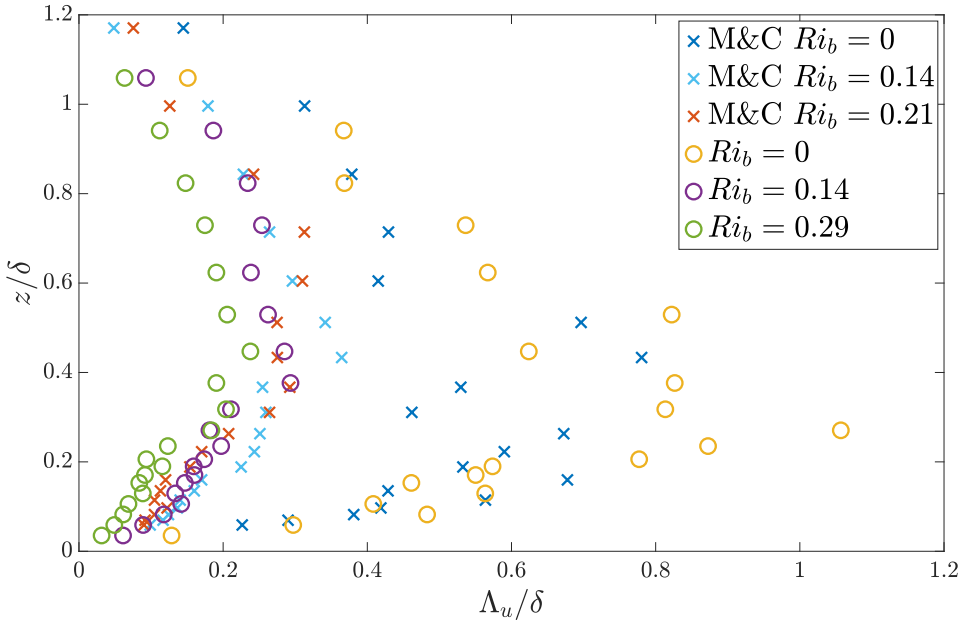

Figure 3.8. Streamwise velocity integral length scales.

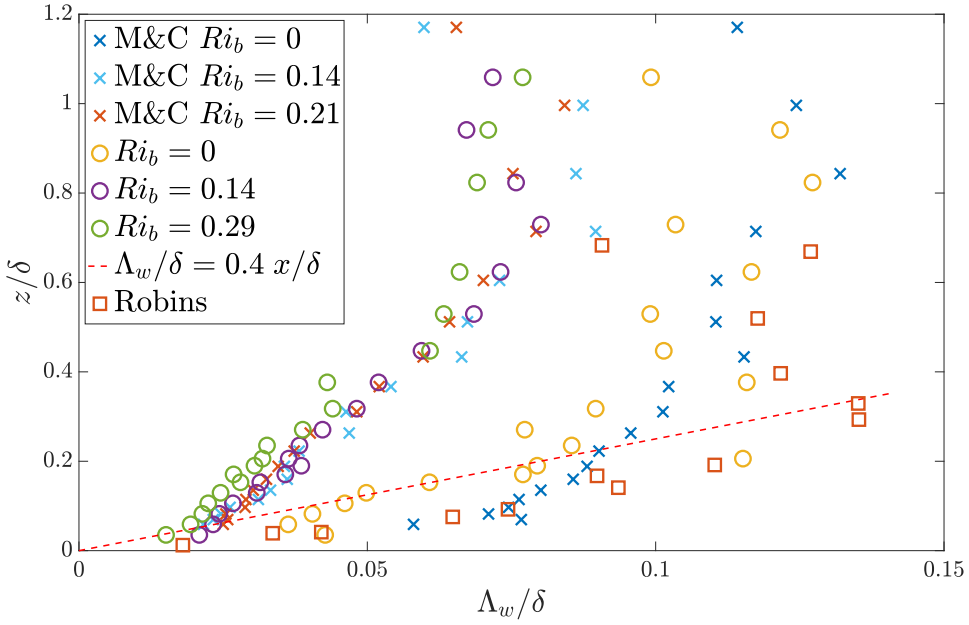

Figure 3.9. Vertical velocity integral length scales.

to measure since a great number of particles in the flow should be traced instant by instant. Given these difficulties, the Lagrangian time scale is often estimated by means of relations as [35]:

$$T_{Lw} = \frac{2\sigma_w^2}{C_0 \varepsilon}. \tag{3.11}$$

where the Kolmogorov constant C_0 has a value in the range $3.5 \leq C_0 \leq 5$ (in this work the value of 4.5 has been selected according to [24]) and ε is the turbulent kinetic energy mean dissipation rate, computed by velocity spectra (figure 3.6). In figure 3.10, vertical profiles are shown for the Lagrangian time scales, computed by means of equation 3.11, in both the dimensional and non-dimensional form.

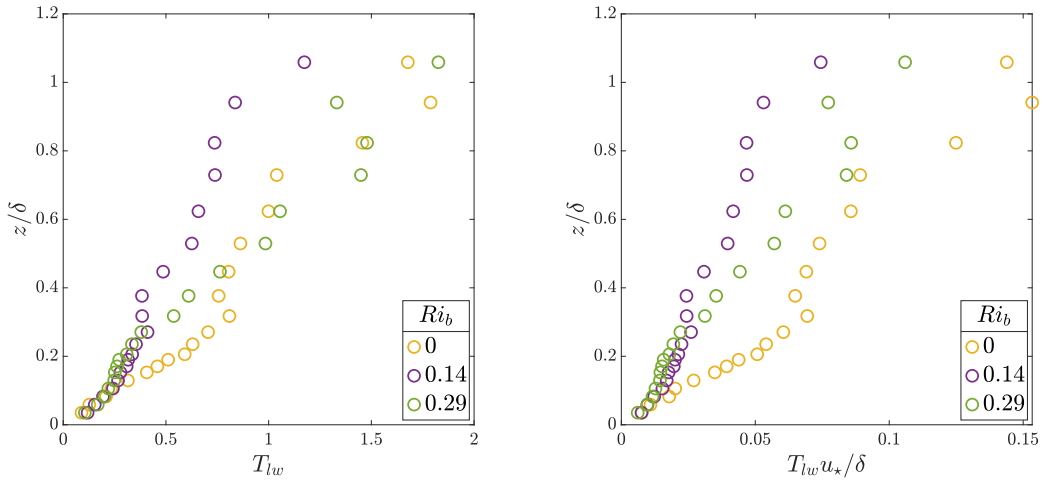

(a) **(b)**

Figure 3.10. Vertical Lagrangian time scales.

3.7 Turbulent viscosity

A deeper analysis for the turbulent components of flow field is obtained computing and analyzing the turbulent diffusivity. This quantity is defined by means of the following formulation:

$$\overline{u'w'} = -\nu_t \frac{\partial \overline{u}}{\partial z}. \tag{3.12}$$

The so defined turbulent viscosity bears with itself some limitations due to the hypothesis introduced for its formal definition. It is based on the turbulent-viscosity hypothesis, first introduced by Boussinesq in 1877, stating that the deviatoric component of Reynolds stress tensor is proportional to the mean rate of strain through a constant called turbulent viscosity. Formally, this hypothesis states that:

$$-\rho\overline{u_i'u_j'} + \frac{2}{3}\rho\delta_{ij} = \rho\nu_t \left(\frac{\partial \overline{u_i}}{\partial x_j} + \frac{\partial \overline{u_j}}{\partial x_i} \right). \tag{3.13}$$

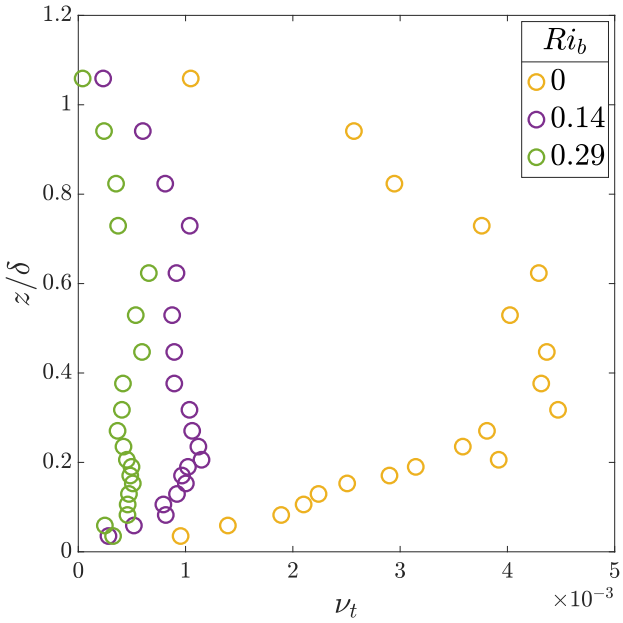

Figure 3.11. Turbulent viscosity profiles.

In the case of two-dimensional turbulent boundary layer, this formal definition reduces to equation 3.12.

Vertical profiles of turbulent viscosity computed for different stability conditions, are shown in figure 3.11.

For a given stability condition, the profiles do not change at varying the position downstream. This result was expected since the flow is considered, and in this way also verified, to be homogeneous along the longitudinal direction. The values and the shape of profiles obtained for the neutral case are similar to values obtained by previous studies [16].

Main differences are visible for different stability condition. In particular, the higher the stability the lower the values of turbulent viscosity. This was expected since increasing the stability causes a decreasing in turbulent stress $\overline{u'w'}$ but the vertical gradient of mean flow is not much affected by stability. From 3.12, it is straightforward to obtain that lower level of turbulence causes lower values of turbulent viscosity.

3.8 Stability characteristics

The peculiarity of the flows reproduced in the experimental campaign is that they have been produced with a temperature gradient along the vertical direction. As explained in section 2.1.1, the temperature is imposed by means of heat exchanger at the inlet of the wind tunnel and cooling plates on the floor. The imposed temperature profiles are shown in figure 2.3.

For the neutral boundary layer, the heat exchanger and the ground plates have been kept switched off. In this case, the measured temperature is constant along the vertical direction and it is the laboratory mean temperature. For the two stable

cases, the action of heating the wind tunnel inlet and cooling the floor produces a temperature profile shown in figure 3.12a. The stability parameters of the flow are obtained by means of mean temperature profiles or temperature fluctuating field in different ways, as several parameters are available in the literature.

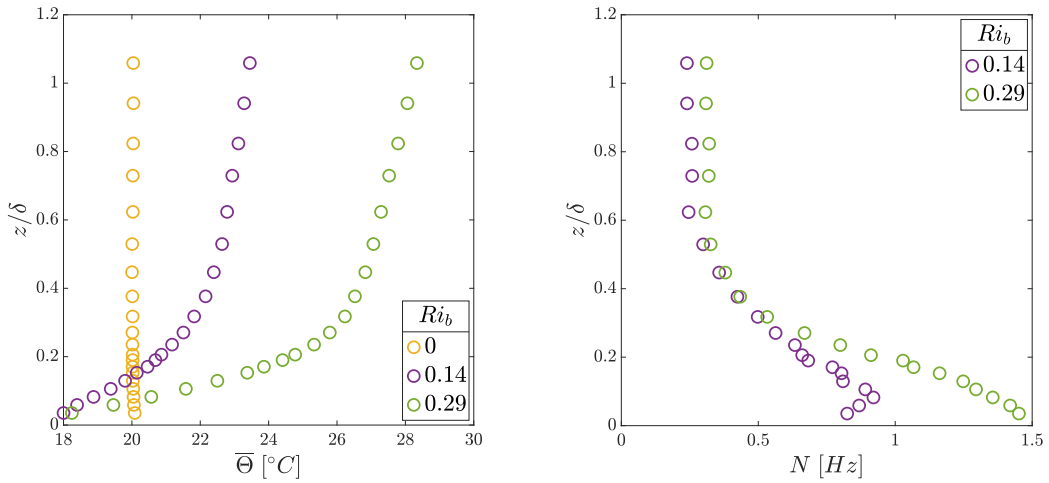

(a) **(b)**

Figure 3.12. Flow stability characteristics.

From equation 1.10 it is possible to evaluate the Brunt-Väisälä frequency profiles, used as stability parameter. Since the considered flows are stable, the value of N is found to be positive. The effect of different strength of stratifications is evident only in a small portion of the boundary layer of N, shown in figure 3.12b, as the profiles almost coincide for measuring points of about $z/\delta > 0.4$.

3.9 Higher order moments

The higher order moments of velocity signals have been investigated to further characterize the flow field. The third and the fourth order moments (skewness and kurtosis) are computed according to definitions presented in section 1.4. Vertical profiles for these statistical moments are shown in figure 3.13. Close to the ground, until a value of about $z/\delta \approx 0.4$, the moments are in good agreement with the Gaussian distribution skewness and kurtosis, i.e. $Sk = 0$ and $Ku = 3$. Going upward, further from the ground, the moments diverge slightly from the reference values of a Gaussian distribution.

In all the cases, there are not in general differences between the neutral case and the stable ones, neither among stable ones only. The profiles of kurtosis are almost coincident for both stream-wise and vertical velocity component. The effect of stability can be seen in the profiles of skewness for the vertical component of velocity in figure 3.13b. The profiles for the stable cases remain almost constant as the height of measurement varies. The neutral case shows a more clear drift from stable profiles and from the Gaussian reference value of $Sk = 0$ the higher from the ground.

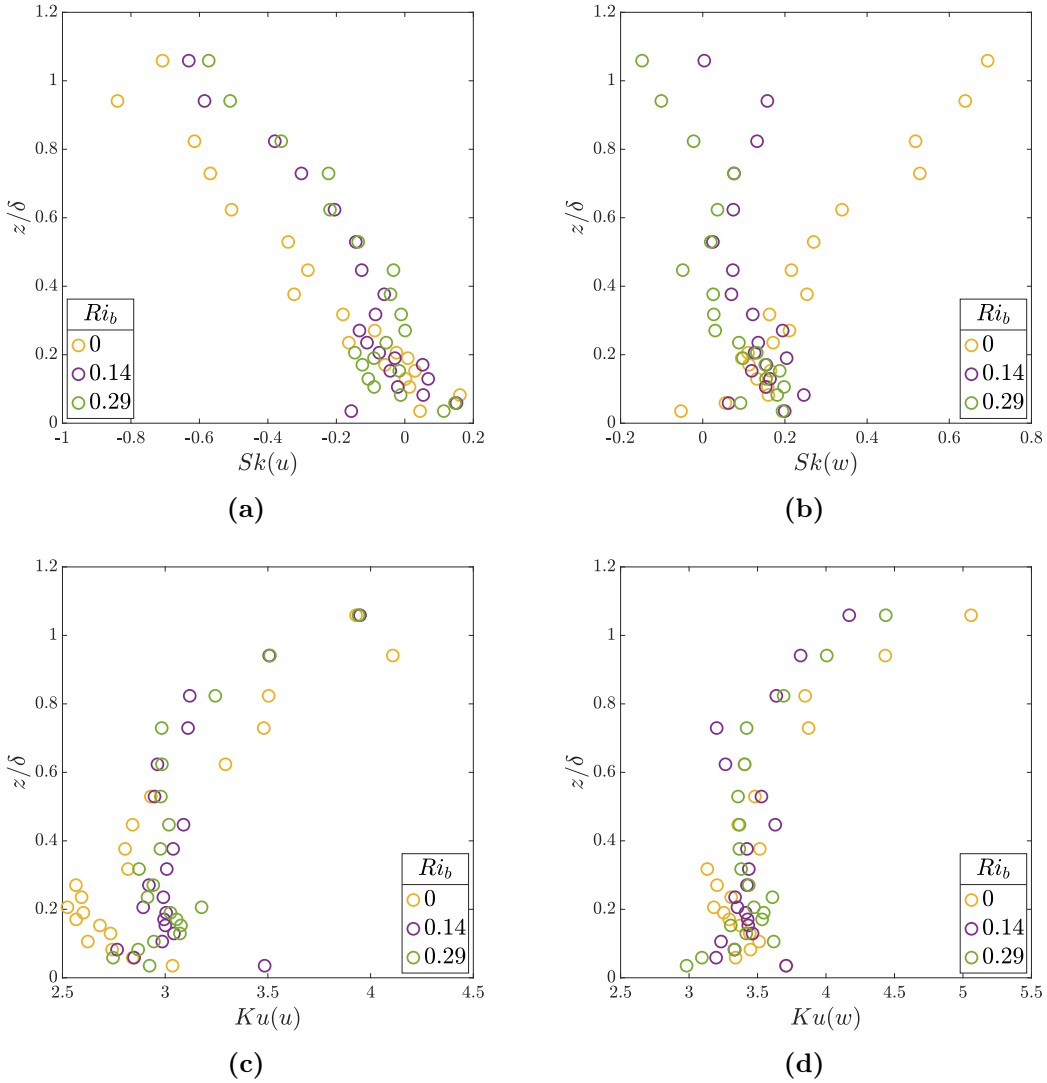

Figure 3.13. Flow field higher order moments.

Chapter 4

Concentration field

4.1 Introduction

In this chapter, dispersion is investigated for an elevated source at varying dimensions of the source diameter and the stability conditions. In literature, a wide study on dispersion has been made for neutral boundary layers. In [8], [23] and [24] the concentration field is investigated by means of statistical instruments such as mean value, fluctuations and higher order moments. In particular the variance, the intermittency, peak values of concentration, probability-density functions and spectra are analyzed. The objective is the understanding of the main mechanisms controlling the scalar dispersion and how they depend on the release condition, the source diameter and the source height.

This work will follow the same approach to treat and analyze the concentration signals from Fast FID. Comparisons between neutral and stable boundary layers and between two source diameters will be done. In the present work, the tracer is injected with a velocity lower compared to the boundary later velocity at the source height. This choice was made during experimental setup in order to avoid the formation of a jet condition at the source.

During experimentation a small drift on the plume has been observed towards the negative y side.

4.2 Mean field

The first analysis is made analyzing the spatial evolution of time-averaged concentration values. As discussed in section 1.5.2 and referring to equation 1.29, the mean concentration field is usually modeled by means of a Gaussian curve:

$$\bar{c}(x,y) = \bar{c}_{max} \exp\left(-\frac{y^2}{2\sigma_y^2}\right). \tag{4.1}$$

For the vertical profiles, a Gaussian distribution is preferred with total reflection in the following form:

$$\bar{c}(x,y) = \bar{c}_{max}\left[\exp\left(-\frac{(z+h)^2}{2\sigma_z^2}\right) + \exp\left(-\frac{(z-h)^2}{2\sigma_z^2}\right)\right], \tag{4.2}$$

which is important mainly when the mean concentration field starts to interact with the floor of the wind tunnel. In order to obtain the Gaussian description of the field, a best fit has been performed on experimental data having $\bar{c}_{max}$, the plume spreads σ_y and σ_z and the vertical coordinate h as free parameters.

Results are shown in figure 4.1 for vertical profiles and figure 4.2 for lateral profiles, measured at different longitudinal locations as reported in table 2.2. Two kinds of visualization are provided for each profile. The first one, i.e. figure 4.1a and 4.2a, provides a comparison between measured mean concentrations, represented as circles, and equations 4.1 and 4.2 represented as lines. In figure 4.1b and 4.2b the Gaussian laws are plotted with rescaled values at the different longitudinal stations where data are collected. The rescaling values are changed stations by stations but, having fixed the longitudinal axis, the same value has been used for the three stability conditions. They do not have physical sense, they have been chosen for graphical clarity. In this way, it is possible to qualitatively visualize the actual development of the plume shape downstream both in lateral and vertical direction.

More profiles of the mean concentration field are reported in appendix A.

Data are presented in the non-dimensional form as:

$$\overline{c^*} = \frac{\overline{c}\,\delta^2\,U_\delta}{\dot{M}_q}, \tag{4.3}$$

where $\dot{M}_q$ is the mass flow of the scalar. The concentration of the scalar injected by the source is changed while changing the longitudinal position of measurement in order to avoid saturation of FID close to the source and to avoid having a weak signal concentration value further downstream. Using non-dimensional format of data ensures a proper comparison along the longitudinal direction. This formulation will be used from now on omitting the apex $(\cdot)^*$ for simplicity.

A good agreement between data and the Gaussian model is observed. Lateral distribution is affected in shape by the stability condition, but it changes the maximum value of measured concentration. Greater differences can be seen in the vertical profiles. Scalar tracer is found in a small region closer to the ground the higher the stability condition considered. The stable boundary layer presents higher values of mean concentration and the pollutant plume is narrower in shape. Moreover it is possible to distinguish a delay in the development of the plume shape. This behavior is in agreement with the theoretical point of view for which atmospheric stability suppresses the turbulence and hence its action on pollutant diffusion.

The center of the mass of the plume is estimated as:

$$z_{cm} = \frac{\int z \cdot \bar{c}\, dz}{\int \bar{c}\, dz}. \tag{4.4}$$

Results are shown in figure 4.3 which shows different behaviors of the center of mass for the three cases studied. For the most stable case, the center of mass keeps a constant position along the longitudinal direction, while for the less stable case it shows a progressive drift upward. For the neutral case, an increase of about 47% of the center of mass between the first and last station is observed.

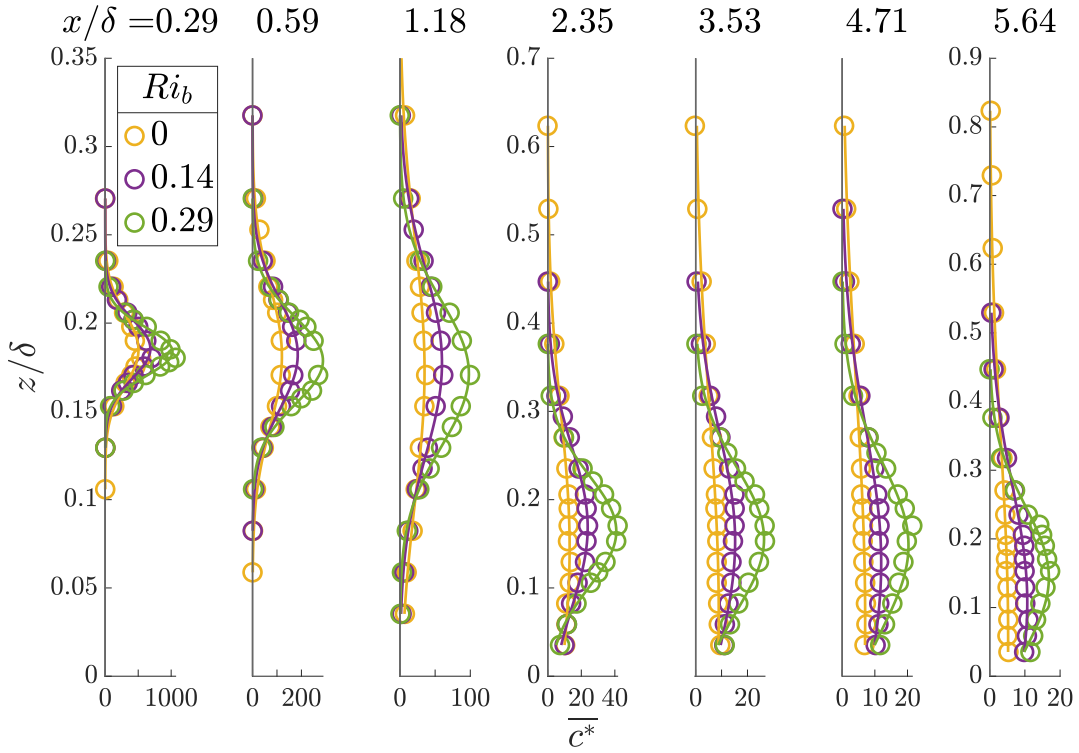

(a)

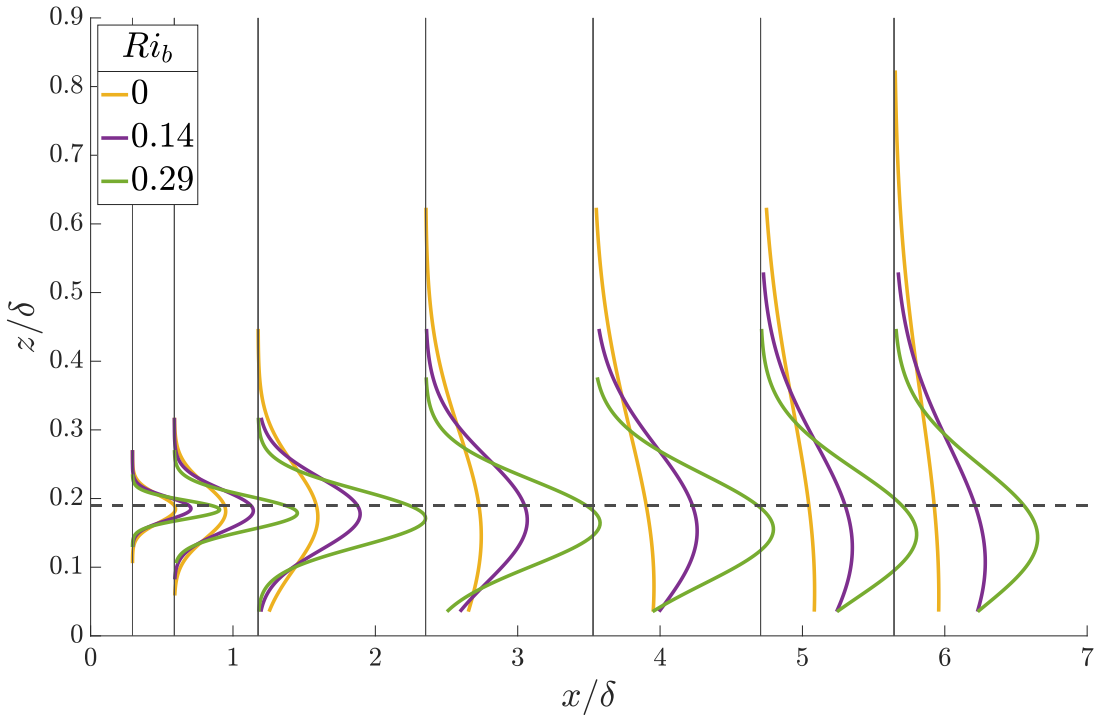

(b)

Figure 4.1. Vertical profiles of mean concentration.

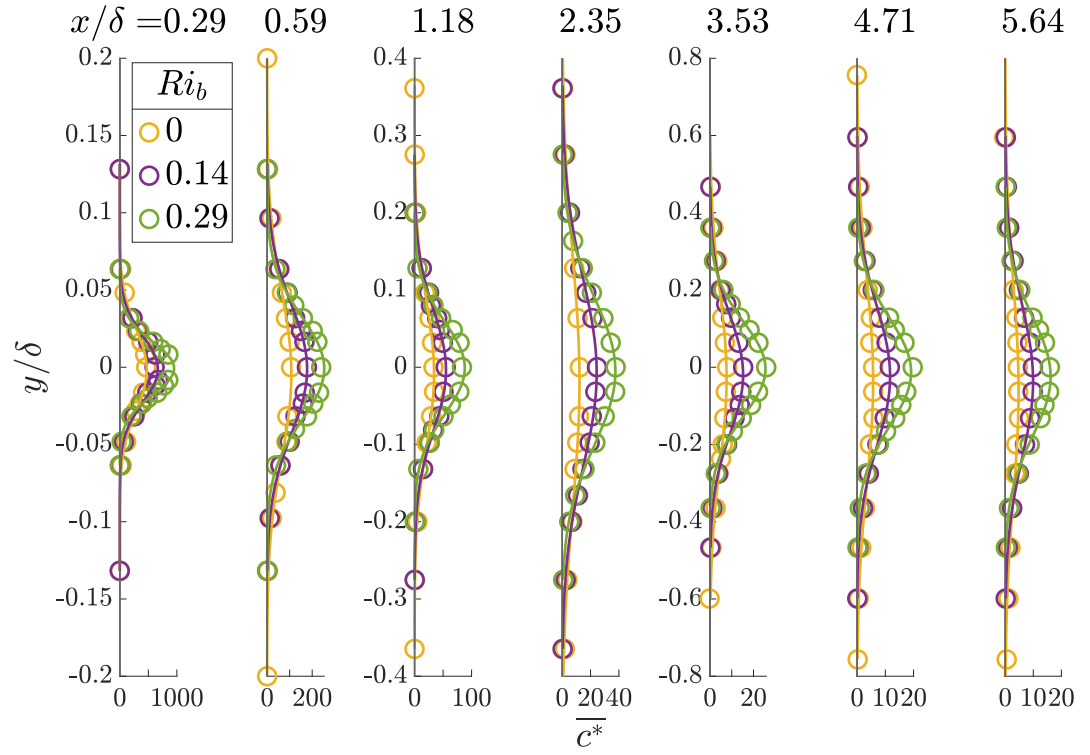

(a)

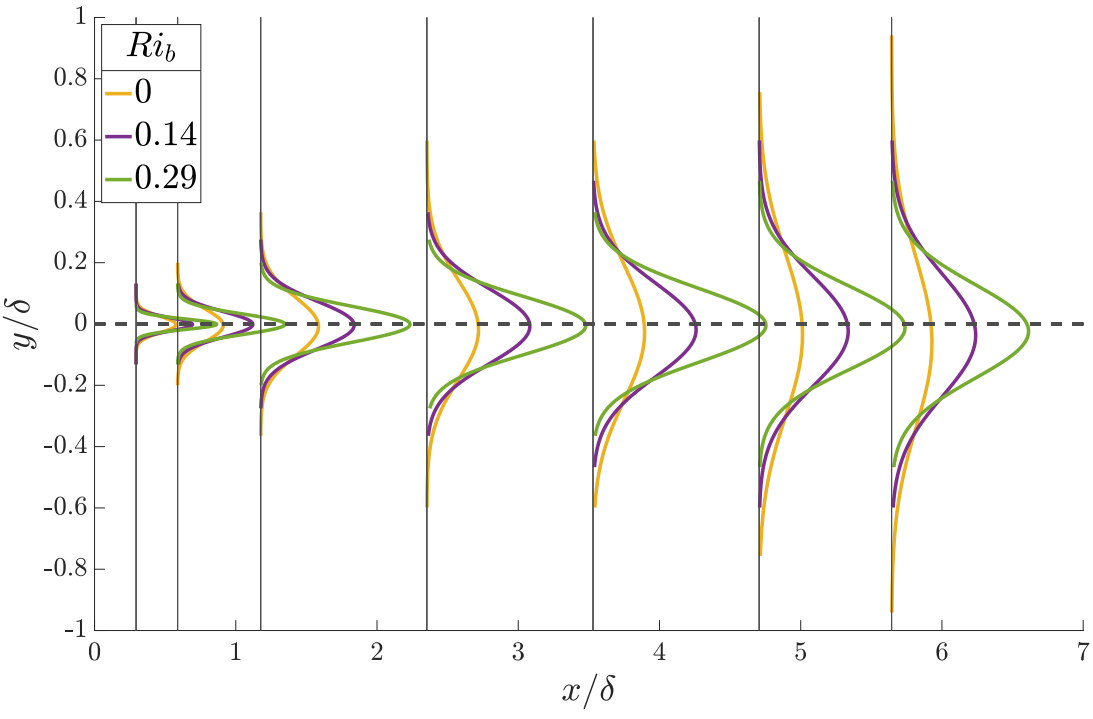

(b)

Figure 4.2. Lateral profiles of mean concentration.

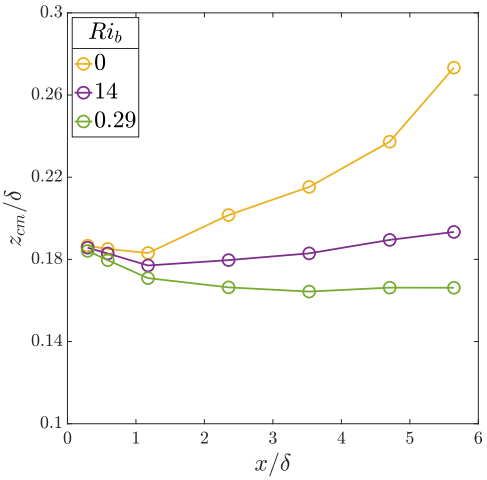

Figure 4.3. Center of mass of the plume.

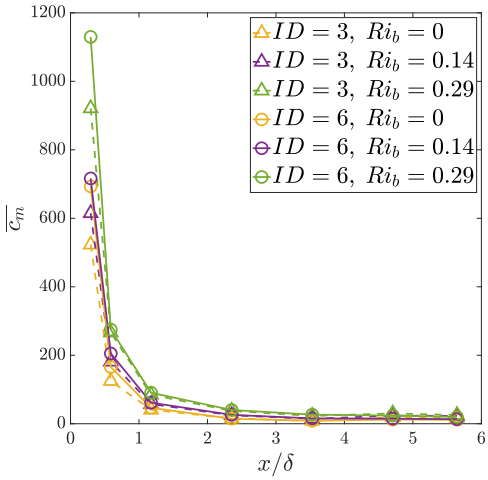

Figure 4.4. Longitudinal profiles of mean concentration at plume center.

In figure 4.4, the non-dimensional values of the mean concentration in the longitudinal direction are reported. The values are obtained from the lateral profiles measured at the source height at different stations, selecting the maximum value measured. Triangles and dotted lines refer to source size with internal diameter of 3.1 mm (ID = 3) while circle and continuous lines to a diameter of 6 mm (ID = 6). As expected [24] there is no dependency of the mean field on the source size. As previously reported, it is possible to verify a trend of mean concentration related to the stability condition: higher stability condition means higher concentration values.

4.3 Concentration variance

The concentration variance, expressed as standard deviation, is investigated by means of the intensity of concentration fluctuations. It is defined as the ratio between the concentration standard deviation and the mean concentration evaluated at the source elevation:

$$i_c = \frac{\sigma_c}{\overline{c}}. \tag{4.5}$$

In figure 4.5, the longitudinal profiles of intensity of concentration at source axis are reported for different stability and source conditions. There is a general trend which can be easily evaluated. Close to the source, the intensity is greater than one, with a peak value which is computed around the second station for all the cases under analysis. Proceeding further from the source, the intensity decreases and eventually reaches the asymptotic value of approximately 0.4.

The greater differences between cases can be seen around the peak of intensity. Considerations about the source size were expected in [24], where it was demonstrated that the standard deviation of concentration strongly depends on source diameter. In particular, the smaller the source, the higher the peak.

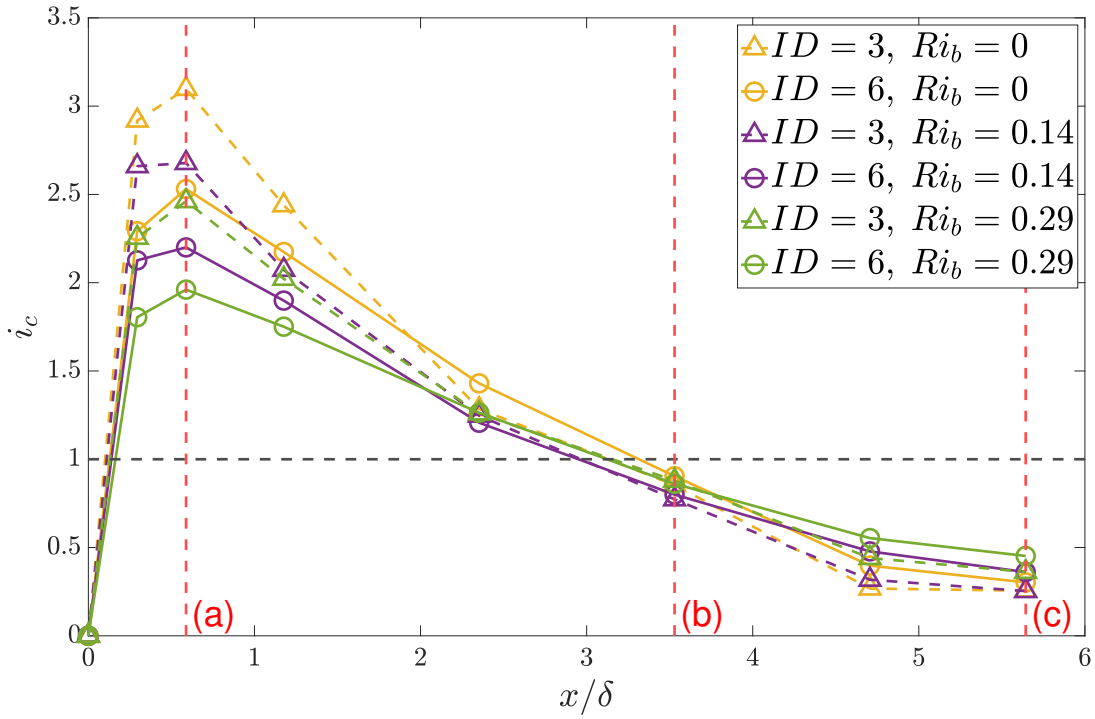

Figure 4.5. Longitudinal profiles of intensity of concentration.

On the contrary, the effects of stability were so far left unstudied. Hence, it is possible to see that the stability condition of the flow where pollutant is diluted effects not only the mean concentration value, figure 4.4, but also its standard deviation. In particular, the stronger the stability condition, the lower the peak, which means lower concentration fluctuations. Further downstream the effects of stability are less evident.

4.3.1 Concentration spectra

To further analyze the effect of stability on concentration, a spectral analysis has been performed on concentration fluctuations. The spectrum $E(k)$ has been computed considering the wavenumber $k = 2\pi f/\overline{u}$ and represents how concentration fluctuations are distributed on turbulence scales.

In figure 4.6, the spectra are plotted in a non-dimensional form, $E^* = E\delta/\sigma_c^2$ as a function of the (non-dimensional) wavenumber. The spectra are computed from the signal at a station close to the source, in 4.6a, and from a station further downstream, in 4.6b.

It is possible to distinguish inertial subranges of small extension which are the regions parallel to the red lines in figure 4.6. However, the interpretation is not straightforward. The meandering motion occurs at small wavenumbers, corresponding to big length scales in the plume. It is the main process in the region close to the source where concentration fluctuations are mainly caused by this motion. On the contrary, relative diffusion occurs at elevated wavenumbers, or fine length scales, and it is predominant in the far field. In it not easy to visualize

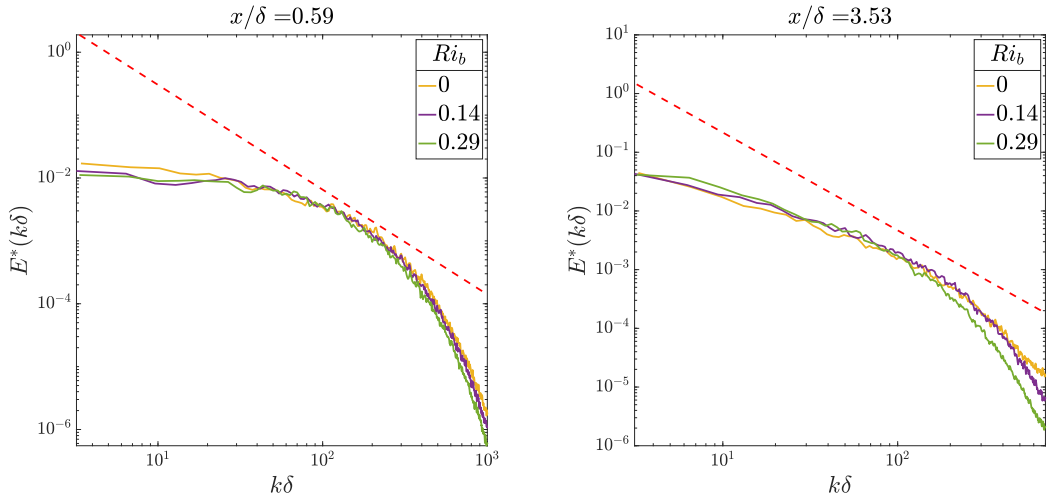

(a) **(b)**

Figure 4.6. Spectra of concentration fluctuations for two longitudinal positions.

these different regions with the spectral analysis presented in this work.

4.3.2 Concentration variance production and dissipation

The balance equation for concentration variance, i.e. equation 1.30, under the hypothesis of neglecting the diffusive transfer, reduces to the following form:

$$\overline{u}_j \frac{\partial \sigma_c^2}{\partial x_j} + \frac{\partial \overline{u_j' c'^2}}{\partial x_j} + 2P + 2\varepsilon_c = 0, \tag{4.6}$$

The dissipation is expressed by

$$\varepsilon_c = D \left(\overline{\frac{\partial c'}{\partial x_j} \frac{\partial c'}{\partial x_j}} \right), \tag{4.7}$$

while the production term is

$$P = \overline{u_j' c'} \frac{\partial \overline{c}}{\partial x_j}. \tag{4.8}$$

Alternatively, it is possible to evaluate the value of the dissipation following the approach proposed in [8]. Dissipation is then expressed from a universal expression valid in the inertial subrange of concentration fluctuations spectra:

$$E(k) = 2\alpha_2 \varepsilon_c \varepsilon^{-1/3} k^{-5/3}, \tag{4.9}$$

where α_2 is a constant value.

Regarding the production, the formulation under hypotheses of a boundary layer diffusion process reads

$$P \approx \overline{w' c'} \frac{\partial \overline{c}}{\partial z}. \tag{4.10}$$

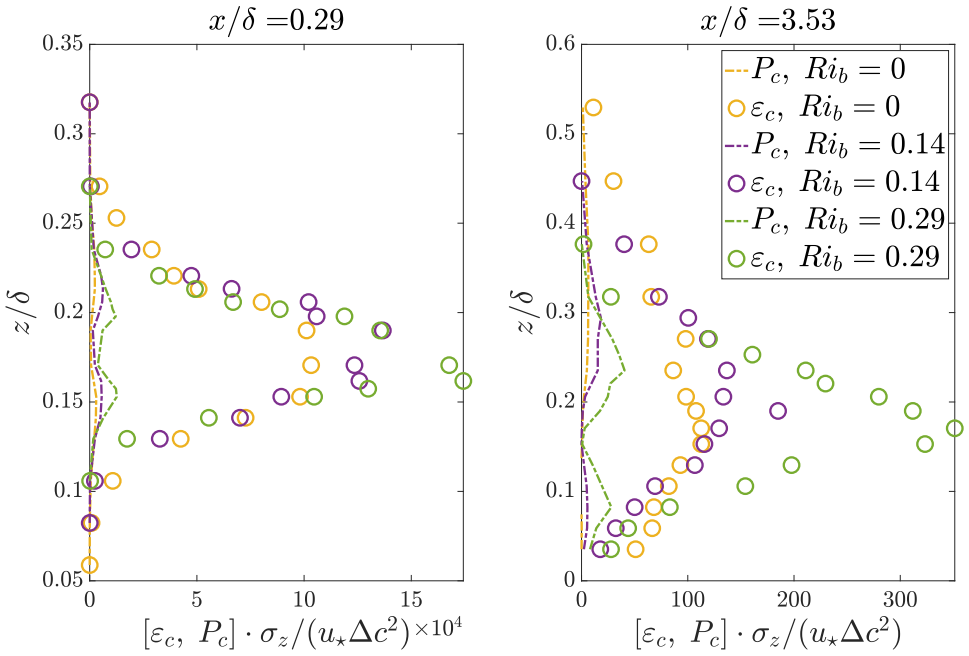

Figure 4.7. Vertical profiles of concentration production and dissipation.

Vertical profiles of production and dissipation of concentration fluctuations are shown in figure 4.7 in non-dimensional form.

A trend in the profiles at varying stability conditions can be recognized. The higher the stability considered, the higher the values of dissipation. This is more evident in the profiles computed further downstream from the source. Similar difference is observed also for the production.

It is generally believed that the dissipation of concentration fluctuations is related to the relative dispersion. This means that higher values for ε_c are related to regions where the relative dispersion is more important with respect to meandering motion. This result is in agreement with the effect of turbulence suppression of boundary layer stability. Reducing the turbulence, reduces the meandering motion which eventually causes an increasing importance of relative dispersion.

4.3.3 Mixing times

To further investigate the action of meandering and relative dispersion of plume dynamic, mixing times have been computed. By definition, the mixing times are obtained as

$$T_M = \frac{\sigma_c^2}{\varepsilon_c}. \tag{4.11}$$

Vertical profiles of two longitudinal stations are reported in figure 4.8. The non-dimensional form is obtained by means of a characteristic time of turbulence, i.e. k/ε.

The mixing time can be interpreted as a characteristic time which allows the concentration of a tracer to become homogeneous inside the flow. It refers to

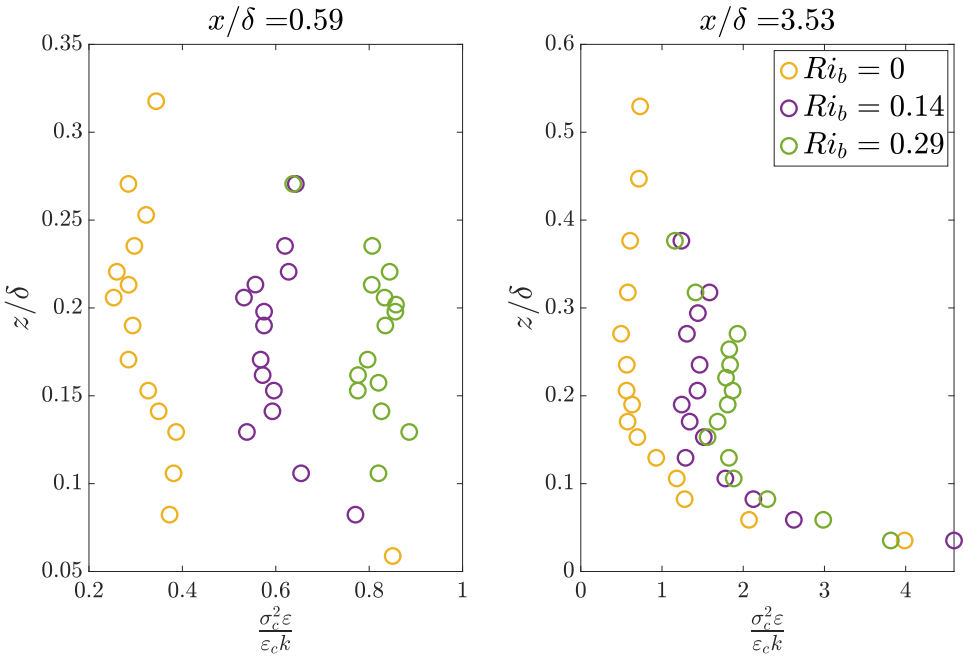

Figure 4.8. Mixing times at two stations along longitudinal direction.

turbulence isotropy, in particular to turbulence small scales. The higher the time, the less efficient is the dispersive action of turbulence.

Profiles show an expected behavior since times are greater when a stronger stability condition is considered. This can be seen better in the profiles closer to the source, in a position of $x/\delta = 0.59$.

4.4 Higher order moments and concentration probability density function

Previous studies such as [24] and [38] report how a statistical description of a concentration signal by means of its probability density function can be well modeled with a gamma distribution. In the present study, a one-parameter gamma distribution has been used in the form

$$p(\chi) = \frac{k^k}{\Gamma(k)} \chi^{k-1} \exp(-k\chi), \tag{4.12}$$

where $\Gamma(k)$ is the gamma function, $k = i_c^{-2}$ and $\chi = c/\bar{c}$. The parameter of the distribution is called intensity of the concentration fluctuations is defined in equation 4.5. Further information about gamma distribution can be found in appendix C.

The consistency of the dataset is verified by searching a simple functional dependency for the moments of the concentration [21], i.e.

$$Sk = a_1 (i_c)^{a_2}, \tag{4.13}$$

$$Ku = b_1 (Sk)^{b_2} + b_3, \tag{4.14}$$

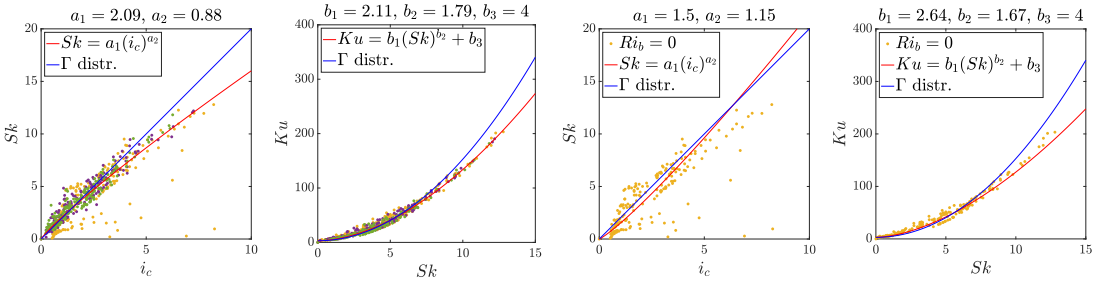

(a) All cases **(b)** $Ri_b = 0$

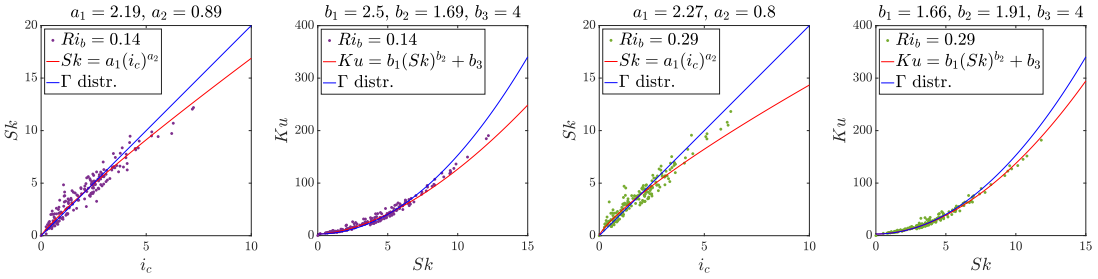

(c) $Ri_b = 0.14$ **(d)** $Ri_b = 0.29$

Figure 4.9. Higher order moments functional dependency and fitting.

where Sk is the skewness, Ku is the kurtosis and a_1, a_2, b_1, b_2 and b_3 are free parameters obtained through a best fit procedure. The logarithmic form of equations 4.13 and 4.14 has been employed in order to perform a linear fitting. The parameter b_3 has been determined by a best fit procedure among the fitted curves of kurtosis versus skewness. The value of $b_3 = 4$ has been found to be the best fitted value. Results of this fitting procedure can be seen in figure 4.9. Figure 4.9a reports the complete data set, while the other figures show dependency for a single stability condition.

Reference values among the free parameters for a gamma distribution are $a_1 = 2$, $a_2 = 1$, $b_1 = 1.5$, $b_2 = 2$ and $b_3 = 3$. The values obtained via the best fit are close but a better agreement could be obtained.

Figure 4.10 shows the probability density functions of concentration signals at source axis. The three cases reported refer to stations defined in figure 4.5: the distribution at peak point for the intensity (label a), the distribution for a value of i_c close to unity (label b) and the distribution for the asymptotic value of i_c in the furthest station from the source (label c). For the station closer to the source, labeled (a), both linear and logarithmic plots are shown. The red line in the figures represent the gamma distribution computed as in equation 4.12. Only the case referred to the neutral case has been reported for the clarity of the figure. A good agreement is reported in terms of shape and values between the gamma distributions and the experimental pdfs.

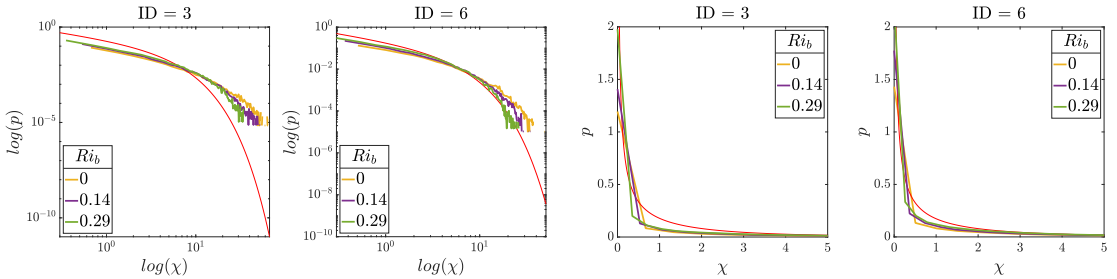

(a) Station (a) - log

(b) Station (a) - lin

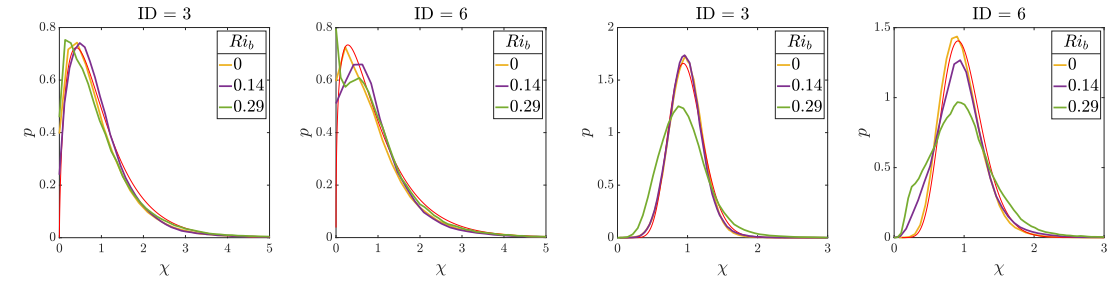

(c) Station (b) - lin

(d) Station (c) - lin

Figure 4.10. Probability density function of concentration at different longitudinal station.

It is worth noting that the gamma distribution is fully regulated by the value of i_c only, and specifically to its value relative to unity: from an exponential-like distribution in the near field, a log-normal-like distribution with short tail in the intermediate field and a Gaussian-like distribution in the far field.

Higher order moments, i.e. skewness and kurtosis, of concentration signal are computed along the longitudinal direction, at the source height and at the center of the plume. The values are compared to the values obtained by gamma distribution in figure 4.11. Data are reported both for different source size and stability conditions. Blue and red lines refer to values of skewness and kurtosis for the gamma distribution of small source size and big source size respectively. A deviation between computed values from data and values obtained by means of gamma distribution modeling can be seen mostly in the region close to the source. This can justify the differences shown in figure 4.9 among the relations between moments of concentration.

4.5 Intermittency factor

One useful and important parameter to study concentration dispersion and large-scale meandering motion is the intermittency factor defined as

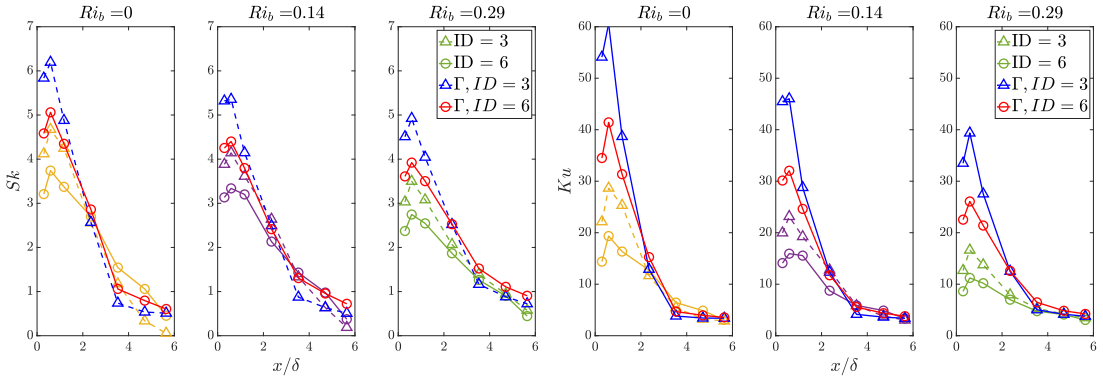

(a) Skewness **(b)** Kurtosis

Figure 4.11. Higher order moments longitudinal profiles.

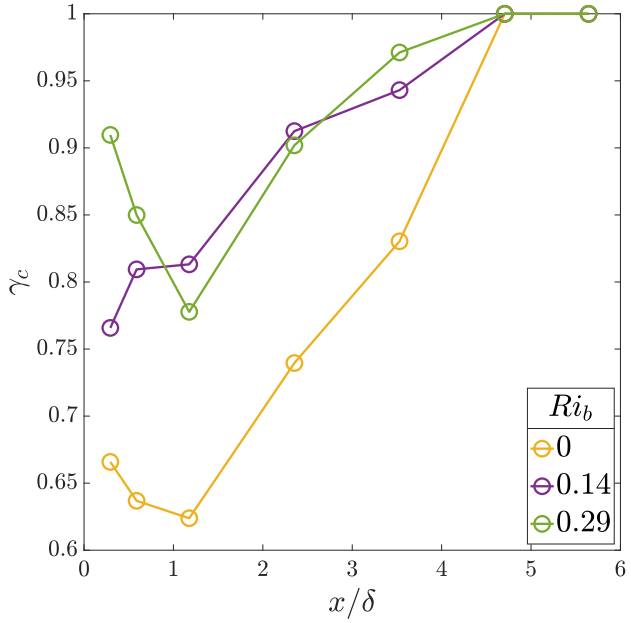

Figure 4.12. Intermittency factor.

$$\gamma_c(x,t) = Prob(c(x,t) > 0). \tag{4.15}$$

This parameter estimates the probability to have a value of concentration greater than zero or greater than a given value Γ_t, selected in order to avoid false results due to noise. The intermittency factor is shown in figure 4.12, where a threshold value of 1 has been selected for Γ_t. The closer to the source, the lower the value of γ_c; this is because, due to meandering effects, the plume is subjected to strong intermittent movements. Moving further from the source, the plume grows in size thanks to the relative dispersion which causes the meandering motion to be damped. For this reason intermittency reduces and γ_c increases.

The meandering effect is related to turbulent scales larger than plume dimension. Meandering causes the plume to oscillate thus generating an intermittent signal of

the concentration. This effect is stronger close to the source since plume dimension is still small and it is easily affected by a larger number of turbulent scales. Moving downstream, the plume spreads increasing its dimension. In this phase, the relative dispersion plays a more important role, reducing fluctuations.

Close to the source, the different role played by meandering motion for different stability condition is evident. As expected, the neutral case shows the lower values of intermittency factor since the turbulent motions are not damped as in the stability cases. The two stable cases are very similar in values. This behavior is caused by the fact that the turbulent quantities for these cases are very close to each other, as shown in figure 3.3.

4.6 Turbulent mass fluxes

The magnitude of turbulent fluxes, i.e. $\overline{w'c'}$ and $\overline{v'c'}$ in equation 1.27, is responsible for the spread of the plume both in vertical and lateral directions, [8]. Figures 4.13 and 4.14 show respectively vertical and lateral profiles of fluxes for different locations along the longitudinal direction. Lateral fluxes are computed at source height, vertical profiles at the center of the plume.

Differences in the lateral fluxes, changing the stability condition, are obeserved. The shape is similar but the values change with the stability. The effect can be observed as well in the lateral spread of the plume which decreases with increasing stability, as in figure 4.19a. Regarding the vertical profiles, it is possible to distinguish in a more clear way the effects of stability. The development of fluxes starts to diverge mostly after a distance from the source of about $x/\delta = 1$. The behavior of vertical profiles for the neutral cases is close to the one shown in [8]. Increasing the stability causes a delay in this development. For example, the profile for the case $Ri_b = 0.29$ at a distance $x/\delta = 5.64$ from the source is similar to the profile for the neutral case at a distance $x/\delta = 2.35$. This is justified by the suppressed action of turbulence by stratification.

The turbulent fluxes are modeled by means of the standard gradient diffusion hypothesis as expressed in equation 1.25.

Along the lateral direction, it is expected to find a constant value of $D_{t,y}$ provided that the lateral gradient of concentration is almost null. The computation of $D_{t,z}$ is highly affected by numerical errors due to the fact both turbulent flux and vertical gradient of concentration change in sign at some point along the vertical direction. Unfortunately, due to uncertainties, there is not a perfect correspondence between zeros and this causes a divergent profile of $D_{t,z}$ at the height of zero turbulent flux. To prevent this numerical issue, the profiles of turbulent flux and concentration gradients are shifted by the computed vertical drift. The vertical drift of zeros is observed to be very small.

The results for the vertical profiles are reported in figure 4.15. These profiles have a fictitious shape caused by numerical corrections employed to avoid strong divergence effect around the source height. In spite of the non-clear shapes, the values show small variations along the vertical directions, having an almost constant

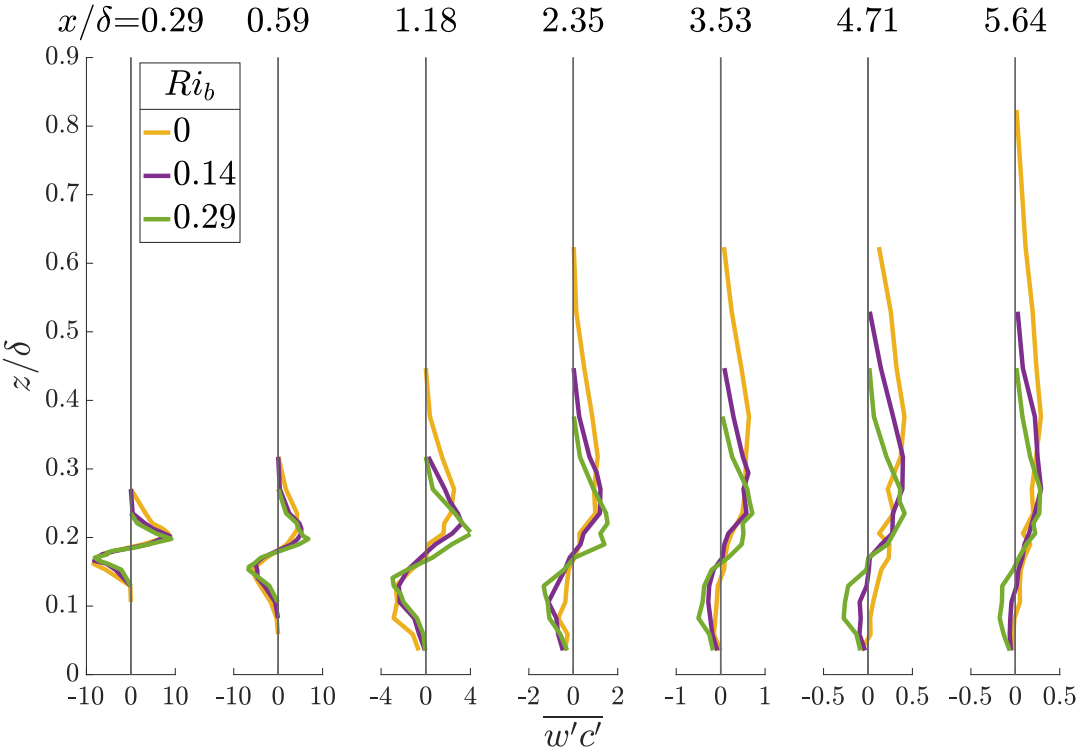

Figure 4.13. Vertical turbulent flux of concentration.

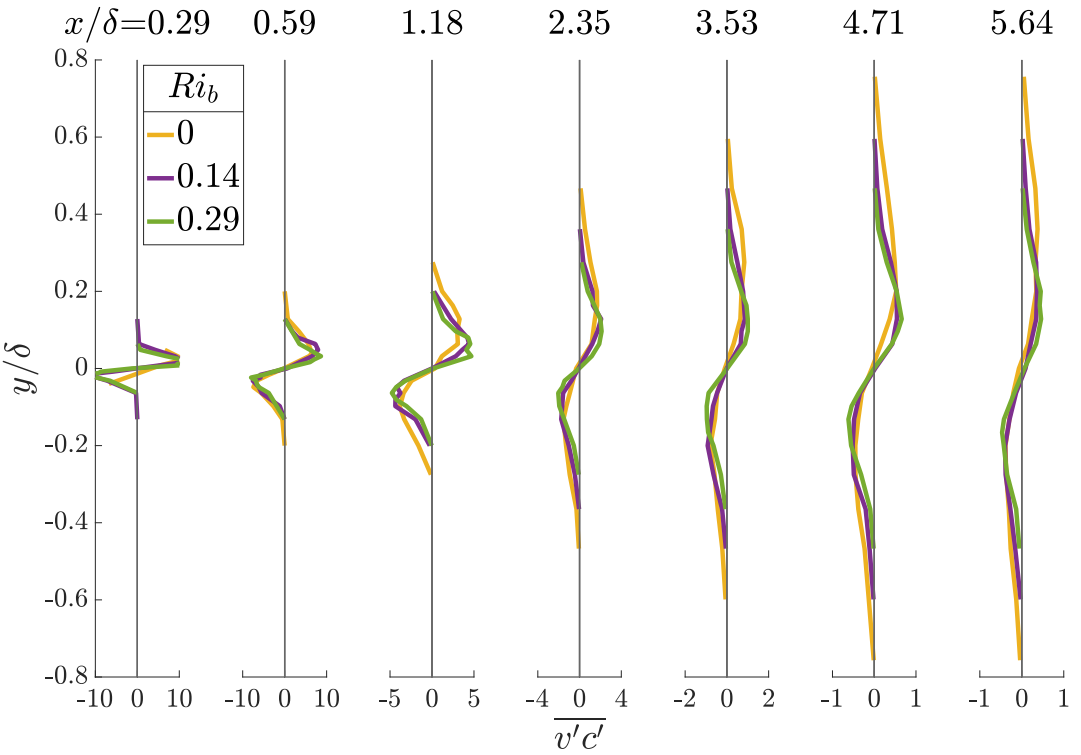

Figure 4.14. Lateral turbulent flux of concentration.

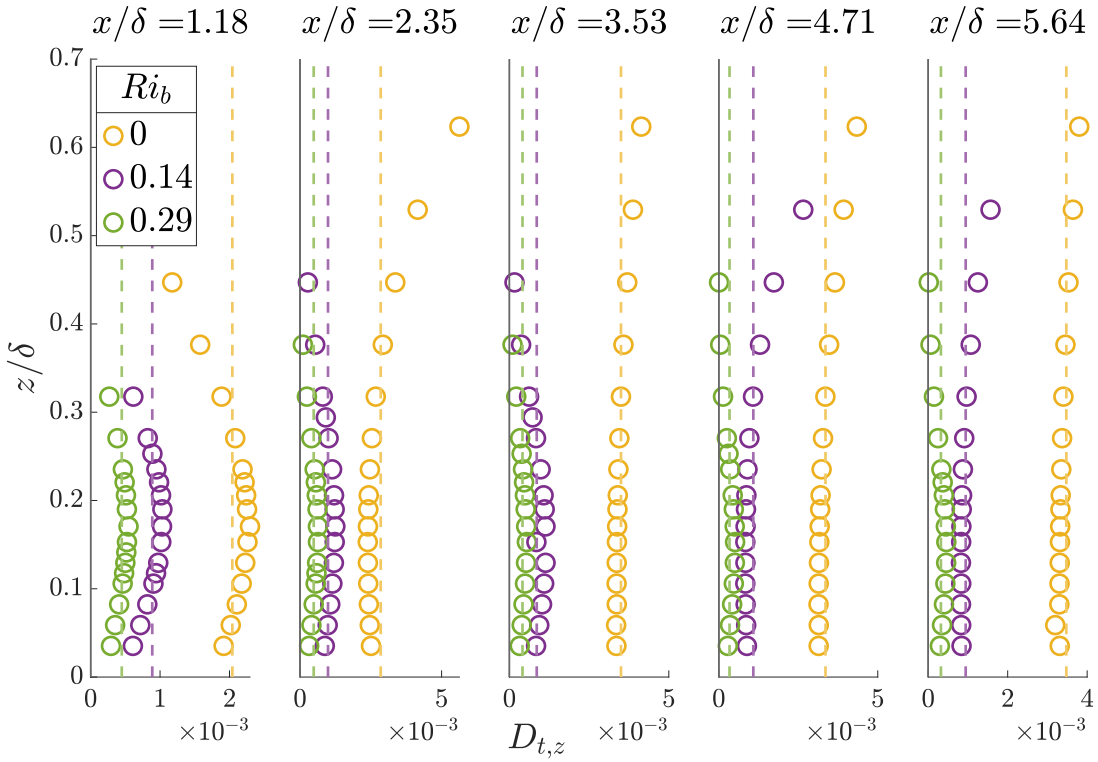

Figure 4.15. Vertical turbulent diffusion coefficient.

value. In the figure, vertical dotted lines represent optimized values of $D_{t,z}$, from here labeled as $\hat{D}_{t,z}$, obtained by means of an optimization procedure on definition, viz.

$$\hat{D}_{t,z} = -\overline{w'c'}/(\partial\overline{c}/\partial z), \tag{4.16}$$

aimed at finding the best coefficient to minimize ratio error.

Lateral values of diffusion coefficient are reported in figure 4.16 for different longitudinal measuring locations.

In this analysis it is possible to verify that the higher the stability condition considered, the lower the value of the diffusion coefficient, both lateral and vertical.

4.6.1 Turbulent Schmidt number

An important characteristic of turbulence is the enhancement of transport, often expressed in terms of turbulent viscosity or turbulent diffusivity of a scalar substance. The turbulent viscosity and diffusivity are both flow-dependent, and the latter depends also on the molecular Schmidt number Sc which is the ratio of molecular viscosity and molecular diffusivity. Even so, these quantities continue to be used because of their convenience in practice and simplicity as theoretical concepts. The turbulent Schmidt number Sc_t is a non-dimensional number defined as the ratio of momentum diffusivity and mass diffusivity, and is used to characterize flows in which there are simultaneous momentum and mass diffusion convection processes. Practically, it is defined as the ratio between coefficients of turbulent viscosity and turbulent diffusion of scalar properties (e.g. density deviation, concentration, buoyancy):

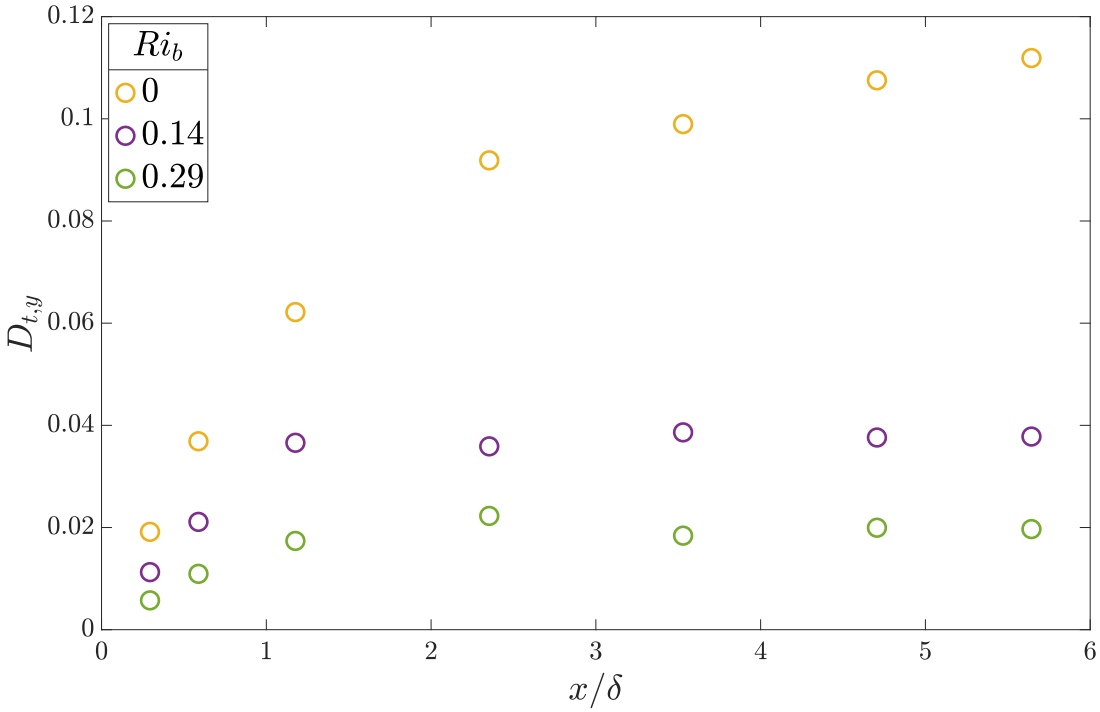

Figure 4.16. Lateral turbulent diffusion coefficient.

$$Sc_t = \frac{\nu_t}{D_t}. \tag{4.17}$$

The profiles for Sc_t have been computed along the vertical direction, hence considering only the vertical diffusivity coefficient $D_{t,z}$. Profiles at different longitudinal stations are shown in figure 4.17.

The relevant result is that the computed Schmidt number is not affected by boundary layer stratification. Profiles appear to be coincident along both the streamwise and the vertical direction. In general, the computed Sc_t are close to the unity value apart for the region closer to the ground.

An estimation for this number is obtained considering the turbulent diffusion coefficient to be a function of the Lagrangian integral time scale, [16] [34],

$$D_{t,z} = \sigma_w^2 T_{Lw}, \tag{4.18}$$

where T_{Lw} is computed by means of equation 3.11. Considering the condition of equilibrium between production, suppression and dissipation rate ε and the relationship for $\nu_t = u_\star \kappa z$, it is possible to obtain the new expression for equation 4.18:

$$D_{t,z} = \frac{2}{C_0} \frac{\sigma_w^4}{u_\star^3} \kappa z. \tag{4.19}$$

In the surface boundary layer the standard deviation of the vertical profile is usually assumed to be a linear function of the friction velocity $\sigma_w = \alpha u_\star$, where

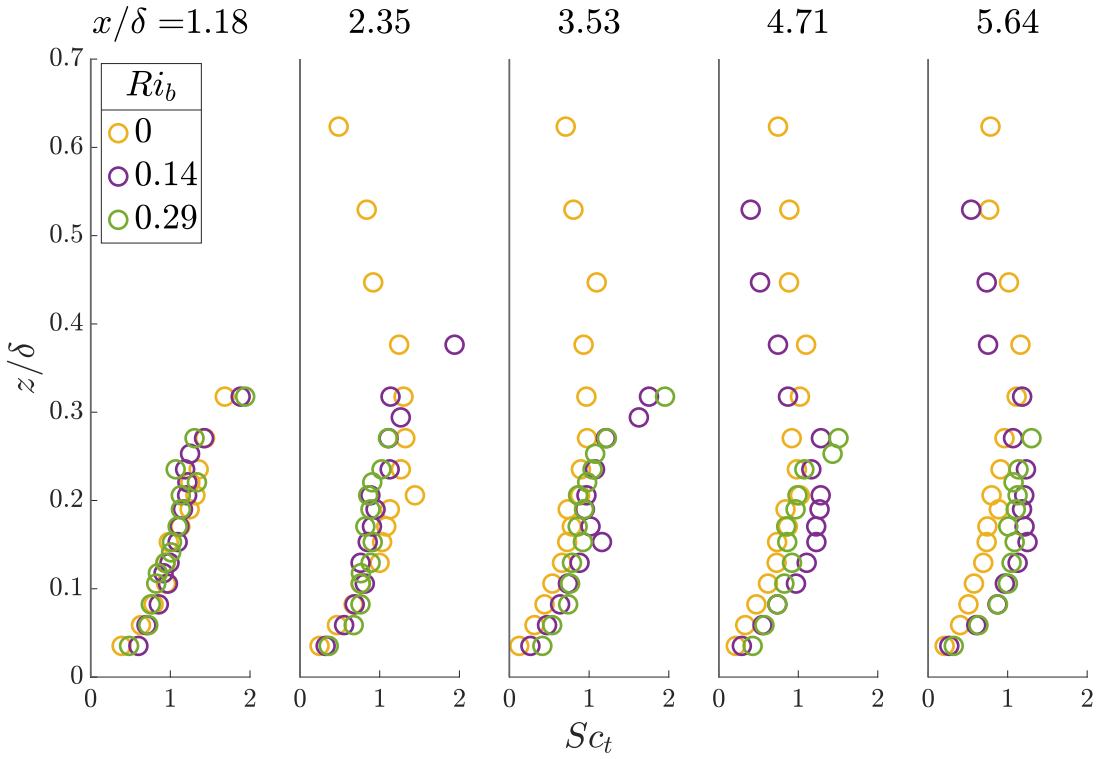

Figure 4.17. Turbulent Schmidt number.

$\alpha = 1.3$. In this way, an approximated version of turbulent diffusion coefficient is obtained, i.e.

$$D_{t,z} \approx \frac{2\alpha^4}{C_0}\nu_t, \tag{4.20}$$

which eventually leads to the approximated turbulent Schmidt number:

$$Sc_t \approx \frac{C_0}{2\alpha^4} = 0.8, \tag{4.21}$$

where the Kolmogorov constant is $C_0 = 4.5$. A good agreement between this approximation and the measured data is seen in the region close to the center of the plume, at a height off the ground from $z/\delta = 0.1$ to $z/\delta = 0.2$.

4.7 Longitudinal mass flux

To verify the reliability of the data set collected at the EnFlo Lab the conservation of the scalar mass along the longitudinal direction of the wind tunnel is evaluated. The computation of mass flux must take into account both mean and fluctuating components of velocity and concentration measured by LDA and FFID:

$$\dot{M}_q = \iint \overline{u}\,\overline{c} + \overline{u'c'}\; dydz. \tag{4.22}$$

The mass flux check is performed evaluating whether the computed flux equals the scalar flux injected by the source or whether the ratio between the two is equal

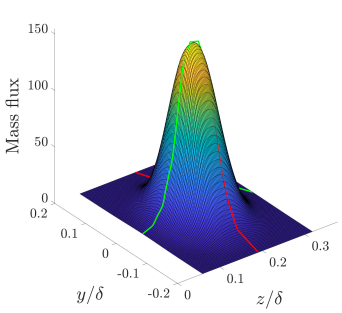

(a) $Ri_b = 0$, $x/\delta = 0.59$

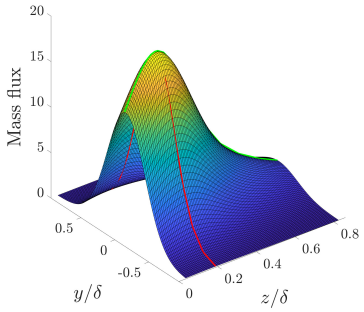

(b) $Ri_b = 0$, $x/\delta = 5.64$

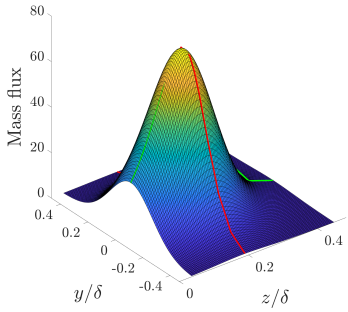

(c) $Ri_b = 0.29$, $x/\delta = 5.64$

Figure 4.18. Mass flux in two-dimensional domain by means of Gaussian approach.

to one.

The procedure needs to have some hypotheses introduced. In fact, only one lateral and one vertical set of concentration and velocity measurements have been made at each longitudinal station while the mass flux check requires the knowledge of quantities in a two-dimensional domain along the vertical and the lateral directions. The Gaussian description of the mean concentration field is helpful. It it hypothesized that the mass flux in equation 4.22 can be described as well by means of a Gaussian or a double Gaussian distribution. Moreover, it is hypothesized that in the integration domain the mass flux is described by a two-dimensional Gaussian distribution, obtained by the two measured profiles. Some of the computed fluxes are shown in figure 4.18. The green and the red lines are the measured profiles along vertical and lateral directions.

In the stations close to the source, the behavior of flux is very similar varying the stability condition. In the further stations, as in figure 4.18b and 4.18c, it is possible to see a different development of the flux. Similar conclusions can be seen in the vertical profiles of mean concentration in figure 4.1.

Final results of mass flux are obtained by means two-dimensional numerical integration and they are reported in table 4.1.

The obtained values can be considered satisfactorily close to unity value, considering a level of uncertainties introduced by experimental data and hypotheses

$\frac{\iint \overline{u}\,\overline{c}+\overline{u'c'}\,dydz}{\dot{M}_q}$		Longitudinal stations x/δ						
		0.29	0.59	1.18	2.35	3.53	4.71	5.64
Ri_b	0	0.97	0.87	0.87	0.88	0.87	0.94	0.83
	0.14	0.97	0.89	0.90	0.92	0.88	0.91	0.91
	0.29	0.92	0.90	0.90	0.89	0.90	0.86	0.82

Table 4.1. Mass flux check.

made. This result is mandatory in order to study the concentration field without the danger of losing information, i.e. concentration of the scalar, along the longitudinal direction during experimental phase. Deeper analysis has verified that the fluctuating part of equation 4.22, i.e. $\overline{u'c'}$, gives a negative contribution to the overall integration and it counts around the 2-3% of the total.

4.8 Plume spread

An important parameter in the study of pollution dispersion is the spread both in vertical and lateral directions. A measure of this parameter is obtained directly from the vertical and lateral profiles of the data. In particular, through a Gaussian approach, i.e. equations 4.1 and 4.2, the values of σ_y and σ_z are obtained with best fitting. Several models have been proposed and tested through years.

Following the Taylor's formulation [34], the spreads are expressed as:

$$\sigma_y^2 = \frac{\sigma_0^2}{6} + 2\sigma_v^2 T_{Lv}\left\{t - T_{Lv}\left[1 - \exp\left(-\frac{t}{T_{Lv}}\right)\right]\right\}, \tag{4.23}$$

$$\sigma_z^2 = \frac{\sigma_0^2}{6} + 2\sigma_w^2 T_{Lw}\left\{t - T_{Lw}\left[1 - \exp\left(-\frac{t}{T_{Lw}}\right)\right]\right\}, \tag{4.24}$$

where t is the flight time which can be computed as x/u_{ave}, T_{Lv} and T_{Lw} are Lagrangian time scales, σ_v and σ_w are standard deviations of lateral and vertical velocity components. For the mean longitudinal velocity u_{ave} the velocity at the center of mass of the plume is considered. Results are reported in figures 4.19a and 4.19b, where dots are spreads computed from data and lines are plume spreads by equations 4.23 and 4.24. Vertical spreads, in particular for stable cases, are found to be lower than the lateral ones.

4.8.1 Vertical spread

Another analytical form to compute the plume spread has been proposed in [31] and it is the following: for neutral case,

$$\sigma_z = 0.4_w t, \tag{4.25}$$

for stable case,

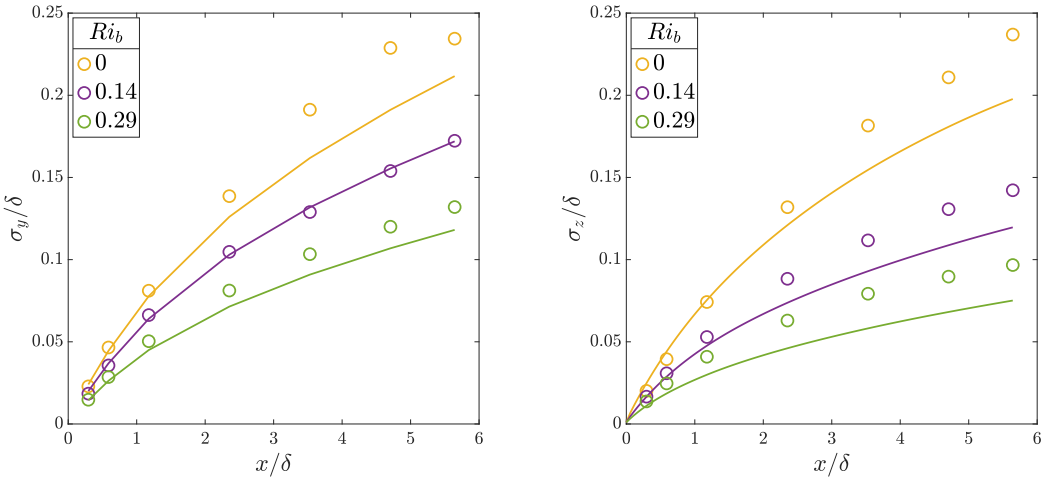

(a) Lateral spread **(b)** Vertical spread

Figure 4.19. Plume spread by means of Taylor model.

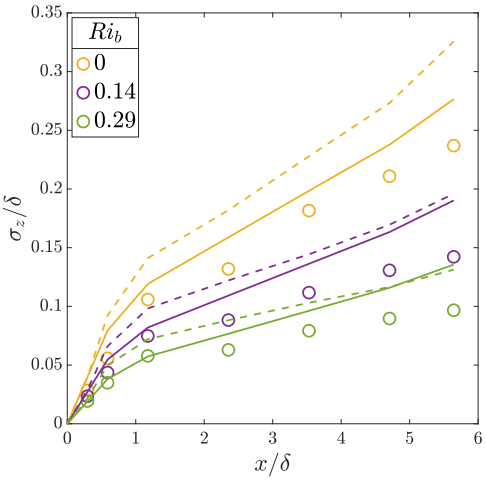

Figure 4.20. Vertical plume spread (data and models).

$$\sigma_z = \frac{\sigma_w t}{\sqrt{6.25 + \frac{N^2 t^2}{1+2Nt}}} \tag{4.26}$$

where σ_v, σ_w e N are computed at the averaged height of the plume z_{cm}. The Brunt - Vaisala frequency is $N = \sqrt{\frac{g}{T_0}\frac{d\vartheta}{dz}}$ and shown in figure 3.12b. This model here presented gives the incremental value of the plume spread station by station. Results are shown in figure 4.20 in lines, among dots which represent experimental data and dotted lines are profiles obtained by means of the following definition:

$$\frac{d\sigma_z^2}{dx} = \frac{D_{t,z}}{2u_{ave}}. \tag{4.27}$$

Ri_b [-]	δ_{Re} [mm]
0	850
0.14	530
0.29	320

Table 4.2. Boundary layer height from Reynolds stresses.

4.8.2 Lateral spread

The model employed for the comparison with experimental data is the following [31]: for neutral case,

$$\sigma_y = \frac{\sigma_v t}{\sqrt{1 + \alpha \frac{u_\star}{\delta}}}, \tag{4.28}$$

while for stable case,

$$\sigma_y = \frac{\sigma_v t}{\sqrt{1 + \alpha \frac{u_\star L}{\delta^2}}}, \tag{4.29}$$

where α is a constant, σ_v is lateral velocity standard deviation computed at source height, t is flight time and L is the Monin-Obukhov length.

The value of α has been fixed at 2.5 through an optimization process between the model and the experimental data.

Two strategies have been employed to express the value of δ. The trivial evaluation of this parameter is the one presented in section 3.2 according to streamwise velocity profiles as indicated in table 3.1. These values imply a bad agreement between computed profiles and measured data as shown in figure 4.21a.

A better agreement is obtained when a different definition of δ is considered. The new value will be indicated as δ_{Re} and it is computed from the Reynolds stresses profiles. In particular, the new boundary layer height is defined as the height from the ground where the spatial derivative of Reynolds stresses in figure 3.3c drops to zero. Values obtained are reported in table 4.2. Results of this approach in terms of plume lateral spread are reported in figure 4.21b.

In both figures 4.21a and 4.21b, the dashed lines are the profiles of lateral spread obtained by means of the following definition:

$$\frac{d\sigma_y^2}{dx} = \frac{D_{t,y}}{2u_{ave}}, \tag{4.30}$$

employed to evaluate, stations by stations, the increment of plume spread.

4.9 Analytical solution for the concentration variance

This method allows to obtain the statistics of the passive scalar in the whole domain in a closed and ready-to-use form. This has been already tested in [2] for a

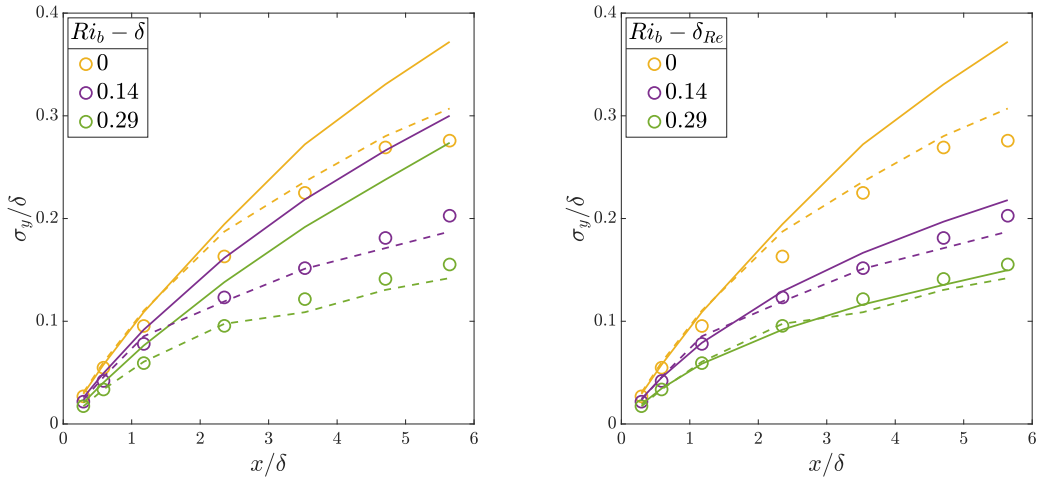

(a) Using δ **(b)** Using δ_{Re}

Figure 4.21. Lateral plume spread (data and models).

neutral boundary layer dispersion. With the data acquired during the experimental phase, this model can be extended also to stable boundary layers. The analytical solution here presented is based on the procedure in [2].

A statistically steady condition for which it can be applied a gradient-diffusion model is taken into account. Consider the one-point one-time probability density function of the concentration, i.e. $p(\psi; x_j)$, whose transport equation can be expressed as follows:

$$\overline{u}_j \frac{\partial}{\partial x_j} p = \frac{\partial}{\partial x_j} \left(D_{t,j} \frac{\partial}{\partial x_j} p \right) + \frac{1}{\tau_m} \frac{\partial}{\partial \psi} \left[p(\psi - \overline{c}) \right], \tag{4.31}$$

where $\overline{u}_j$ is a component of mean velocity field, $D_{t,j}(x_j)$ is the turbulent diffusivity (presented in section 4.6) and τ_m the mixing timescale, discussed in appendix D.

For an x-oriented flow with homogeneous mean velocity $\overline{u}$, the advective mass flux along the longitudinal direction is significantly larger than its turbulent counterpart, which brings to he assumption that $D_{t,x} \approx 0$. Moreover, the statistics of velocity fluctuations are assumed to be homogeneous and isotropic, implying constant $D_{t,y}$, $D_{t,z}$ and τ_m.

It is convenient to introduce the following scalings:

$$X = \frac{x}{L}, \ (Y, Z) = \sqrt{\frac{\overline{u}}{D_{t,y,z} L}} (y, z), \ \mathcal{A} = \frac{L}{\tau_m \overline{u}}, \tag{4.32}$$

where L is a characteristic length, i.e. the boundary layer height δ in this case.

Multiplying equation 4.31 for ψ^n and integrating, the following system of equations is obtained for the nth order moment μ_n:

$$\mathcal{L}_n \mu_n = n \mathcal{A} \mu_1 \mu_{n-1}, \tag{4.33}$$

where $\mathcal{L}_n = \frac{\partial}{\partial x} - \frac{\partial^2}{\partial y^2} - - \frac{\partial^2}{\partial z^2} + n\mathcal{A}$.

When $n = 1$, equation 4.33 reduces to a homogeneous linear partial differential equation whose solution is the classical Gaussian model for the mean plume dispersion:

$$\mu_1 = \overline{c} = \frac{m}{X} \exp\left[-\frac{Y^2 + Z^2}{4X}\right], \tag{4.34}$$

where m is a constant determined by applying boundary conditions.

When $n > 1$, the solution for equation 4.33 is obtained by means of the Green's function $G[X_j, X_{0,j}]$ implying

$$\mathcal{L}_n G[X_j, X_{0,j}] = \delta_D[\hat{X}_j], \tag{4.35}$$

where δ_D is the Dirac's function and coordinates $\hat{X}_j$ are referred to the local reference frame $X_{j,0}$, i.e. $\hat{X}_j = X_j - X_{0,j}$.

Applying the Fourier transform to the last equation, which leads to

$$G[\hat{X}_j] = \frac{\vartheta[\hat{X}]}{4\pi\hat{X}} \exp\left[-n\mathcal{A}\hat{X} - \frac{\hat{Y}^2 + \hat{Z}^2}{4\hat{X}}\right] \tag{4.36}$$

where ϑ is the Heaviside function, and considering the properties of the Dirac's function, the exact solution for the statistical moment is eventually obtained:

$$\mu_n = n\mathcal{A} \iiint_{-\infty}^{+\infty} \mu_1(X_{0,j})\mu_{n-1}(X_{0,j})G[\hat{X}_j]\, dX_{0,j}. \tag{4.37}$$

It is now considered the case of a localized source of diameter d_s placed at the origin of the reference frame at a height h_s from the ground and within a turbulent boundary layer. Since this configuration does not satisfy the hypotheses of homogeneous and isotropic turbulence, the following approximations must be considered: (i) $\overline{u}$ is the velocity at the source height, (ii) $D_{t,y}$ and $D_{t,z}$ are constant when solving the equations but space-dependent in the final formula.

If vertical profiles of concentration are considered, the reflection to the ground is solved by means of a mirror imaginary source leading to the Gaussian solution:

$$\mu_1 = \vartheta[X]\frac{m}{X}\left(\exp\left[-\frac{Y^2 + Z^2}{4X}\right] + \exp\left[-\frac{Y^2 + (Z + 2H_s)^2}{X}\right]\right), \tag{4.38}$$

where $m = \dot{M}_q/(4\pi\sqrt{D_{t,y}D_{t,z}}L)$ comes from the mass conservation and $H_s = h_s\sqrt{U/D_{t,z}L}$ is the non-dimensional source height.

Regarding the second order moment, with the specification of reflection into the ground, the solution reads

$$\mu_2 = 2\mathcal{A}m^2 \int_{\xi}^{X} \left(\frac{\exp[-2A(X - X_0) - \frac{Y^2+Z^2}{2(2X-X_0)}]}{X_0(2X - X_0)} + r_2\right) dX_0, \tag{4.39}$$

where $\xi > 0$ is a parameter depending on source conditions and r_2 is the reflection term:

$$r_2 = \frac{1}{X_0(2X - X_0)} \exp\left[-2\mathcal{A}(X - X_0) - \frac{Y^2 + (Z + 2H_s)^2}{2(2X - X_0)}\right] \cdot \left(1 + 2\exp\left[\frac{H_s(2H_sX_0 + X_0Z - H_sX)}{X_0(2X - X_0)}\right]\right). \quad (4.40)$$

The longitudinal integral in equation 4.39 is analytically solvable only on the plume axis if the wall reflection is neglected. Otherwise, a numerical approach is requested with the crucial feature that the lower bound ξ is numerically small (in a range around 10^{-18}).

The following procedure can be applied. The integral in equation 4.39 is split in the longitudinal domain as follows

$$\mu_2 = 2\mathcal{A}m^2 \int_\xi^X g(X_j, X_0)\, dX_0 = 2\mathcal{A}m^2 \left[\int_\xi^\varphi g(X_j, X_0)\, dX_0 + \int_\varphi^X g(X_j, X_0)\, dX_0\right], \quad (4.41)$$

where $\varphi \ll 1$ is a small value but big enough not to provide numerical issues when solving the second integral in the right-hand side of equation 4.41. The first term, i.e. the integral between ξ and ψ, is related to a region in the very proximity of the source. Here, the reflection term can be neglected and, since $X_0 \ll 1$, the integrand function g can be expanded in a first order series of X_0:

$$\int_\varphi^X g(X_j, X_0)\, dX_0 \approx \left[\frac{\log(\varphi/\xi)}{2X} + F\right] \exp\left(-2\mathcal{A}X - \frac{Y^2 + Z^2}{4X}\right), \quad (4.42)$$

where F is a function with small numerical influence.

The parameter ξ which appears in the integral of equation 4.39 is introduced to avoid singularity and it is linked to the source conditions. This is expressed as $\xi = (d_s/h_s)^{10}$ through a best fit of experimental data, keeping in mind that experiments have demonstrated how the ratio between the initial size of the plume (related to source diameter d_s) and the largest eddy (related to h_s) affects the concentration fluctuations close to the source.

In this analysis, concentration signals taken at the source height in the center of the plume are considered at different longitudinal stations. For these points, the analytical solutions of first and second order moment are computed and compared with experimental data. The second order moment is expressed in terms of intensity of concentration fluctuations, i.e. the ratio between the standard deviation and the mean value.

Results for the first order moment, i.e. the mean value, are shown in figure 4.22. The profiles from the analytical solution are in agreement with the experimental one, expect small uncertainties close to the source. Figure 4.23 shows the results for the second order moment. It is evident that two values of the mixing times, as shown in figure D.1 are necessary to simulate the behavior of the experimental profiles. Closer to the source, a constant mixing timescale produces better results

while further downstream a variable mixing timescale is necessary. The results for the two scales can be matched empirically when $i_c \approx 1$. However, it is evident that a better agreement should be searched, mainly in a region close to the source where the intensity of concentration is high.

The small drift between data and models is caused by the choice of parameter ξ. In fact, it requires to be calibrated each time fitting the experimental data. In the present work, the value chosen for this parameter is the one employed by [2]. A better analysis can be done evaluating the specific value of ξ for the cases presented.

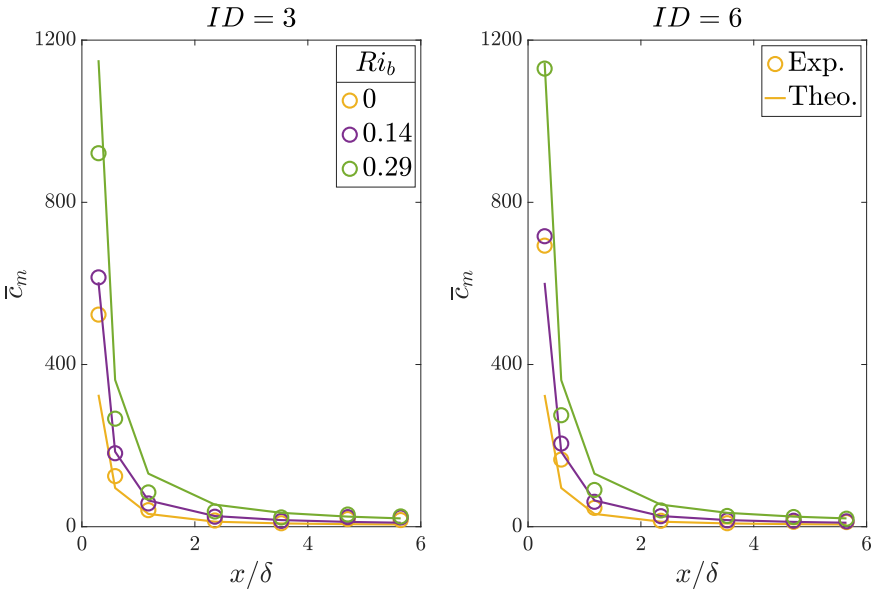

Figure 4.22. First order moment analytical solutions and data.

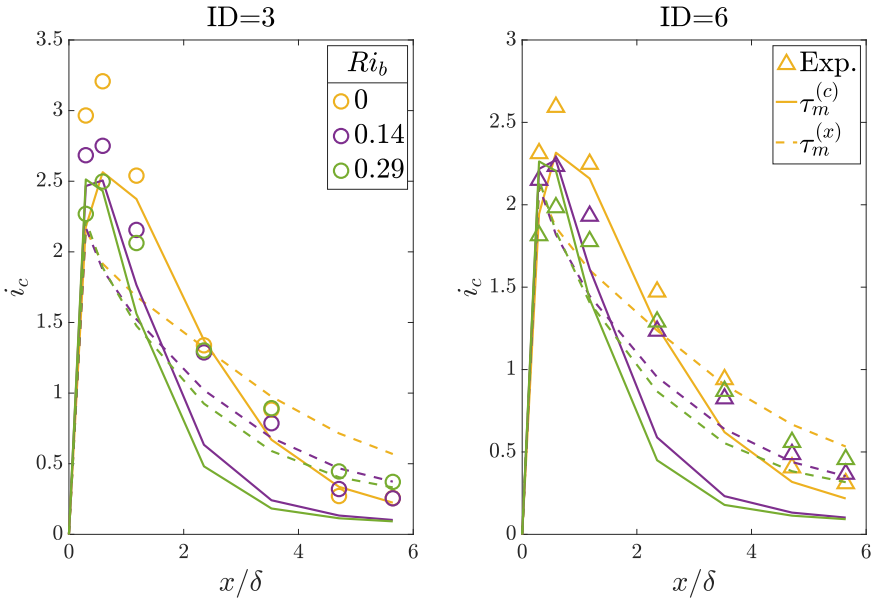

Figure 4.23. Second order moment analytical solutions and data.

Conclusions

The main objective of this work was to analyze the effect of the atmospheric stability on pollutant dispersion in the atmospheric boundary layers. Before the present work, no laboratory experiments have been performed with this specific purpose.

The first achievement was to properly simulate the atmospheric stratification within a wind tunnel. The EnFlo Lab wind tunnel at the University of Surrey has been the experimental facility for this kind of task. The peculiarity of this wind tunnel is the presence of heat exchangers at the walls and at the ground of the wind tunnel in order to reproduce a heat flux within the boundary layer.

The experimental campaign aimed at characterizing the stable boundary layers have brought good results. The action of turbulence suppression by means of atmospheric stability has been reported. The stability of the boundary layer can be well reproduced and it can be widely employed for this kind of study in the future.

The analysis of the concentration field has shown promising results. A strong dependency on the stability conditions has been reported for profiles of mean concentration. It has been observed how the suppression of atmospheric turbulence by means of stratification causes the suppression of the diffusion process as well. An atmosphere in stable conditions is not able to effectively mix and diffuse a pollutant diluted within. Moreover, an analysis on plume spread, along with the validation of some previous models, have been done reporting great differences at varying the stability conditions.

Up to the fourth order moments of concentration signals have been analyzed and a good agreement between the one-point concentration probability density function and the gamma distribution has been verified. However, a deeper study on this correlation needs to be performed since a misalignment between the higher order moments has been observed in a region close to the source. This behavior could be caused by an interaction between LDA seeding and pollutant tracer measured by the Fast FID.

The coupling between the concentration field and the velocity field has been studied computing turbulent fluxes. The application of closure models has brought to the analysis of the turbulent diffusion coefficients and the turbulent Schmidt number. The latter was found to be independent of the stability condition considered.

Many paths are now open for future investigations. The stratification of atmospheric boundary layers can be well reproduced and applied to pollutant transfer

but they can also be applied to other real case scenarios. The study can be extended to urban pollution simulation, reproducing scale models of real urban areas, or to wind farms analysis.

The experimental campaign can be expanded. Other stability conditions can be considered in order to understand more deeply the effect of stability on pollutant dispersion. The simulation of unstable boundary layers will be of great interest. Moreover, more source conditions could be tested: changing the source size, the source height or the condition of emission of the tracer. In this way a more complete dataset will be available for future studies or analyses.

The dataset collected during the experimental phase can be considered a one of a kind among the experiments in pollutant dispersion in the atmosphere. As previously mentioned, no other laboratory experiments are available in literature about this subject. According to this unicity, the results presented here can be employed to calibrate some of the wide range of dispersion models available nowadays, such as analytical models or Lagrangian particles models.

Appendix A

Mean concentration profiles

In this appendix, the vertical (figure A.1) and lateral (figure A.2) profiles of the mean concentration field are reported for each measuring point along the longitudinal axis. Further analysis is reported in section 4.2.

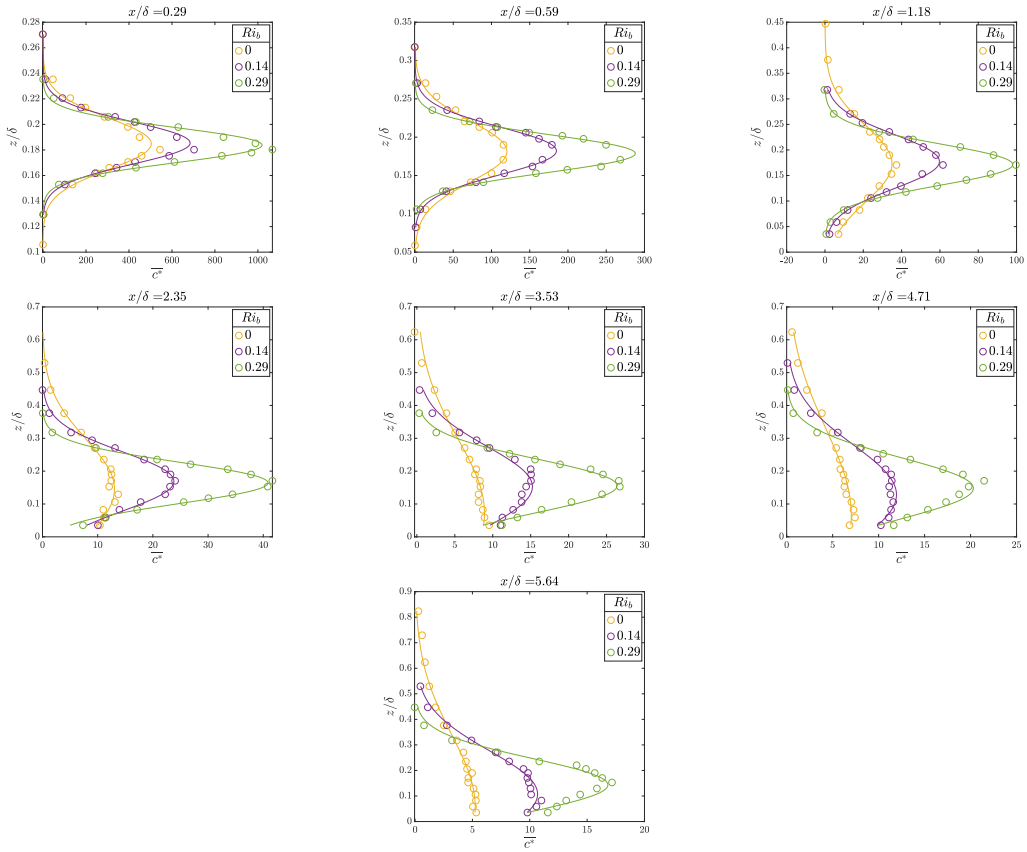

Figure A.1. Vertical profiles mean concentration at each longitudinal location.

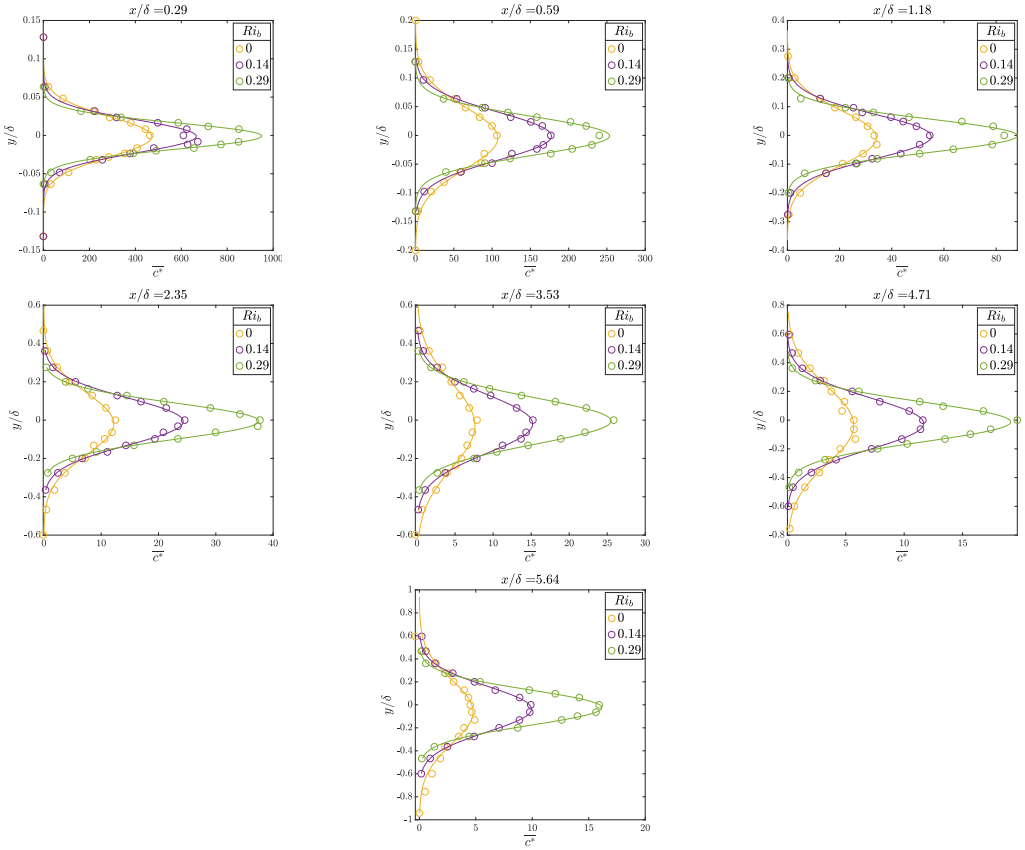

Figure A.2. Lateral profiles mean concentration at each longitudinal location.

Appendix B

Pasquill stability classes

There is not a unique and standard definition of atmospheric stability. However, a proper description of the atmospheric conditions is necessary to evaluate the pollutant dispersion.

F. Pasquill proposed in [28] a simple scheme to characterise and define the stability conditions of the atmosphere. It is based on seven, sometimes six, classes which are defined according to wind speed and day and night cycle. The classes are reported in table B.1.

Even if this classification has been sometimes criticized for its semplicity, it has proven to be useful when considering the Gaussian model in non-neutral atmosphere.

The original classification was based on six classes of stability but class G has been added by other authors in order to achive simmetry in the scheme. However, this class is not very useful since it can be experienced in particular atmospheric conditions (such as night calm wind with possible mist formation) for which the application of Gaussian models is problematic due to the lack of a preferred transport direction.

The classification is based on the criteria presented in table B.2. The exact evaluation of day and night conditions is not unique but in general, for incoming solar radiation, the following values are considered: strong $>$700 W/m^2, moderate 350-700 W/m^2, slight $<$ 350 W/m^2.

The ground roughness is not taken into account in this procedure. This makes this classification weak since uncertanties are high. However, it is possibile to define a new procedure which takes into account the roughness of the ground and

Class	**Atmospheric conditions**
A	Very unstable
B	Unstable
C	Slightly unstable
D	Neutral
E	Slightly stable
F	Stable
G	Very stable

Table B.1. Atmosphere stability classes.

Surface wind speed [m/s]	Daytime solar radiation			Nighttime cloud cover		
	Strong	Moderate	Slight	>50%	<50%	Clear
<2	A	A-B	B	E	F	G
2-3	A-B	B	C	E	F	G-F
3-5	B	B-C	C	D	E	-
5-6	C	C-D	D	D	D	-
>6	C	D	D	D	D	-

Table B.2. Meteorological conditions for stability classes.

the Monin-Obukhov length defined in section 1.3.4. The stability condition is hence defined by figure B.1 according to roungness length z_0 and the opposite of Monin-Obukhov length. Typical rounghness values are the following: 1 mm for deserts or snowy terrains, 1 cm for meadows with short grass, 10 cm for uncultivated land, 1 m for forests or urban areas.

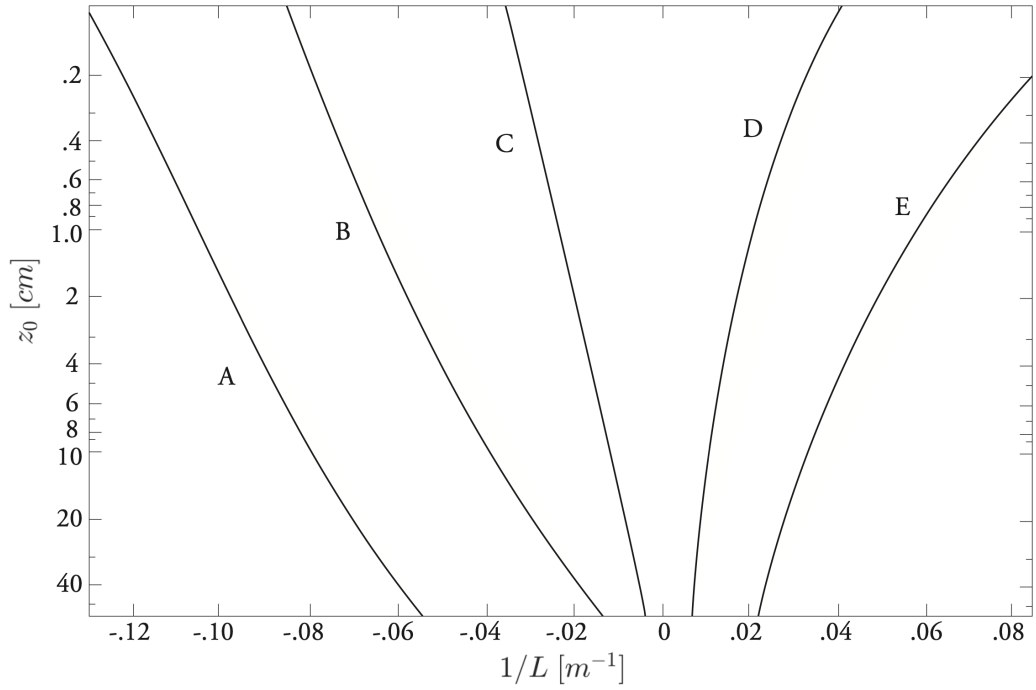

Figure B.1. Relation between stability classes with ground rounghness and Monin-Obukhov length.

Appendix C

Gamma distribution

The gamma distribution has been introduced since it has appeared to be the best statistical distribution to model the probability density function of a concentration signal from a point source in a turbulent boundary layer. For further considerations see section 4.4.

In statistics, the gamma distribution is a two-parameter family of continuous probability distributions. Some other distributions, such as the exponential, the Erlang and the chi-squared, can be considered as special cases of the gamma distribution. In order to describe this distribution, three different parametrization can be employed:

- using a shape parameter k and a scale parameter ϑ,
- using a shape parameter $\alpha = k$ and a rate parameter, defined as the inverse of the scale parameter $\beta = 1/\vartheta$,
- using a shape parameter k and a mean parameter $\mu = k\vartheta = \alpha/\beta$.

This distribution, in one of its different parametrizations, is applied to a wide range of different fields. The following are just a few examples of its application. It can be used to model the aggregate insurance claims and the amount of rainfall accumulated in a reservoir. In wireless communication, the gamma distribution is used to model the multi-path fading of signal power. In oncology, the age distribution of cancer incidence often follows the gamma distribution, where the shape parameter stands for the number of driver events while the scale parameter for the time interval between them. In neuroscience, it is used to describe the inter-spike intervals. In bacterial gene expression, it describes the copy number of a constitutively expressed protein with the mean number of bursts per cell cycle as scale parameter and the mean number or protein molecules produced by a single mRNA during its lifetime as shape parameter.

From a mathematical standpoint, the formal definition for the gamma distribution with the shape-scale parametrization is the following:

$$f(x; k, \vartheta) = \frac{x^{k-1} e^{-x/\vartheta}}{\vartheta^k \Gamma(k)}, \tag{C.1}$$

with $x > 0$, $k > 0$, $\vartheta > 0$ and $\Gamma(k)$ is the gamma function. Some different gamma distributions are shown in figure C.1 in terms of probability density function and cumulative density function.

The skewness and the kurtosis for this distribution depend only on the shape parameter k. The values are respectively $2/\sqrt{k}$ for the skewness and $3 + 6/k$ for the kurtosis.

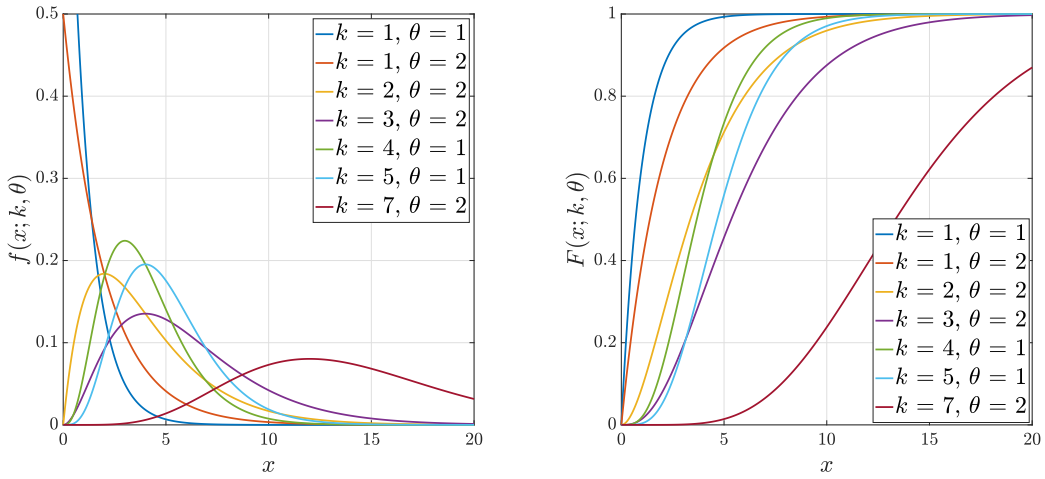

(a) Probability density function **(b)** Cumulative density function

Figure C.1. Gamma distribution.

The gamma function $\Gamma(x)$ was devised by Euler (1729) to extend the factorial from positive integers to real and complex numbers:

$$\Gamma(x) = \int_0^\infty e^{-s} s^{x-1}\, ds \qquad \mathrm{Re}(x) > 0. \tag{C.2}$$

A graphical description of this function in presented in figure C.2.

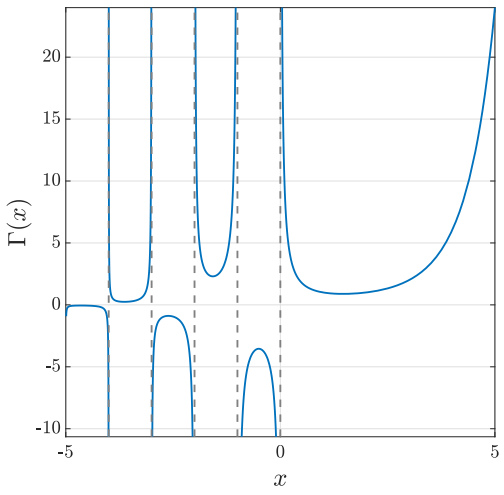

Figure C.2. Gamma function.

Appendix D

Mixing timescales for the analytical solution

Two mixing timescale models will be necessary to satisfactorily model the solution for concentration variance. In the meandering-dominated regime, close to the source, a constant mixing timescale $\tau_m^{(c)}$ will be adopted. On the contrary, in the relative dispersion regime, further from the source, an x-dependent mixing timescale $\tau_m^{(x)}$ will be used.

Different formulations for τ_m are available in literature. In this work, the formulation presented by [6] has been used. The mixing timescale is expressed as

$$\tau_m^{(x)} = \alpha \frac{\sigma_r}{\sigma_{ur}}, \tag{D.1}$$

where α is an empirical constant whose value of 0.65 has been obtained with a best fit of experimental data, σ_r is the relative plume spread around the plume's center of mass and σ_{ur} is the root-mean square of the fluctuations of relative velocity.

The relative plume spread is computed as

$$\sigma_r^2 = \frac{C_r \varepsilon (t_0 - t)^3}{1 + \left[C_r \varepsilon (t_0 - t)^3 - d_s^2\right] / (d_s^2 + 2\sigma_u T_L t)}, \tag{D.2}$$

where $t_0 = (d_s^2 / C_R \varepsilon)^{1/3}$ is the inertial formulation for a dispersion from finite source size, $t = x/U$ is the flight time, T_L is the Lagrangian timescale computed by means of equation 3.11 and $C_r = 0.3$ is the Richardson constant.

The term $\sigma_u r$ is modeled as [17]:

$$\sigma_{ur}^2 = \sigma_u^2 \left(\frac{\sigma_r}{L_E} \right)^{2/3}, \tag{D.3}$$

where $L_E = \varepsilon \left(2\sigma_u/2\right)^{3/2}$ is the Eulerian integral scale and σ_u^2 is the mean of three velocity component variances. Notice that when the plume reaches the Eulerian scale, i.e. $\sigma_r = L_E$, the meandering motion becomes negligible and $\sigma_{ur} = \sigma_u$.

For the constant mixing timescale, the following formulation has been adopted:

$$\tau_m^{(c)} = 0.44\tau = 0.44 \frac{k}{\varepsilon}. \tag{D.4}$$

The values computed for the mixing timescales are shown in figure D.1.

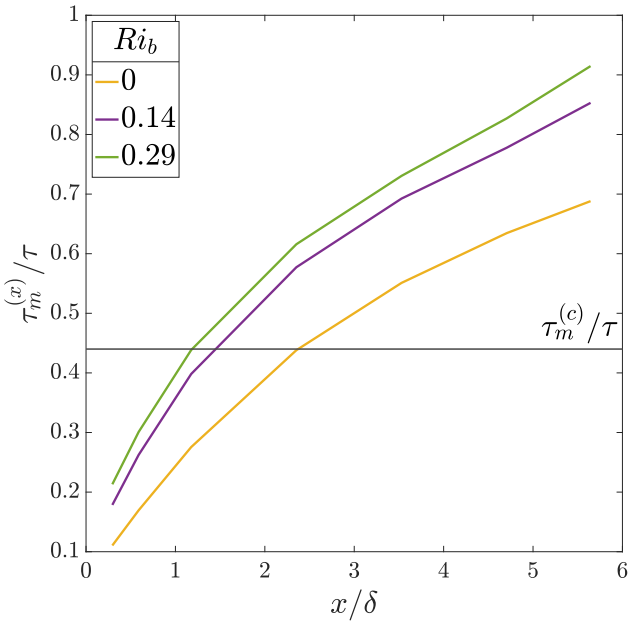

Figure D.1. Mixing timescales.

Bibliography

[1] Jonathan O Anderson, Josef G Thundiyil, and Andrew Stolbach. "Clearing the air: a review of the effects of particulate matter air pollution on human health". In: *Journal of Medical Toxicology* 8.2 (2012), pp. 166–175.

[2] Matteo B Bertagni et al. "Solution for the statistical moments of scalar turbulence". In: *Physical Review Fluids* 4.12 (2019), p. 124701.

[3] Bert Brunekreef and Stephen T Holgate. "Air pollution and health". In: *The lancet* 360.9341 (2002), pp. 1233–1242.

[4] Claudio Cancelli, Maurizio Boffadossi, and Pietro Salizzoni. *Fluidodinamica ambientale: Turbolenza e dispersione*. Otto Editore, 2006.

[5] SB Carpenter et al. "Principal plume dispersion models: TVA power plants". In: *Journal of the Air Pollution Control Association* 21.8 (1971), pp. 491–495.

[6] M Cassiani, P Franzese, and Umberto Giostra. "A PDF micromixing model of dispersion for atmospheric flow. Part I: development of the model, application to homogeneous turbulence and to neutral boundary layer". In: *Atmospheric Environment* 39.8 (2005), pp. 1457–1469.

[7] JE Fackrell. "A flame ionisation detector for measuring fluctuating concentration". In: *Journal of Physics E: Scientific Instruments* 13.8 (1980), p. 888.

[8] JE Fackrell and AG Robins. "Concentration fluctuations and fluxes in plumes from point sources in a turbulent boundary layer". In: *Journal of Fluid Mechanics* 117 (1982), pp. 1–26.

[9] RGJ Flay and DC Stevenson. "Integral length scales in an atmospheric boundary-layer near the ground". In: *Australasian Fluid Mechanics Conference, 9 th, Auckland, New Zealand*. 1987, pp. 464–467.

[10] Frank Gifford Jr. "Statistical properties of a fluctuating plume dispersion model". In: *Advances in geophysics*. Vol. 6. Elsevier, 1959, pp. 117–137.

[11] World Bank Group. *The cost of air pollution: strengthening the economic case for action*. Vol. 1. 2016. URL: `http://documents.worldbank.org/curated/en/781521473177013155/The-cost-of-air-pollution-strengthening-the-economic-case-for-action`.

[12] Philip E Hancock and Paul Hayden. "Wind-tunnel simulation of weakly and moderately stable atmospheric boundary layers". In: *Boundary-layer meteorology* 168.1 (2018), pp. 29–57.

[13] Institute for Health Metrics and Evaluation. *GBD Compare Data Visualization*. URL: `http://vizhub.healthdata.org/gbd-compare`.

[14] HPAH Irwin. "The design of spires for wind simulation". In: *Journal of wind engineering and industrial aerodynamics* 7.3 (1981), pp. 361–366.

[15] Jagadish Chandran Kaimal and John J Finnigan. *Atmospheric boundary layer flows: their structure and measurement*. Oxford university press, 1994.

[16] H. Correia L. Soulhac P. Salizzoni M. Marro H. Gamel. "High-frequency measurements of turbulent mass fluxes in wall bounded flows". Submitted for publication.

[17] Massimo Marro et al. "Dispersion of a passive scalar fluctuating plume in a turbulent boundary layer. Part III: Stochastic modelling". In: *Boundary-layer meteorology* 167.3 (2018), pp. 349–369.

[18] Davide Marucci. "Effects of atmospheric stratification on flow and dispersion in the urban environment." PhD thesis. University of Surrey, 2019.

[19] Davide Marucci, Matteo Carpentieri, and Paul Hayden. "On the simulation of thick non-neutral boundary layers for urban studies in a wind tunnel". In: *International Journal of Heat and Fluid Flow* 72 (2018), pp. 37–51.

[20] Davide Marucci et al. "Wind-tunnel simulation of stable atmospheric boundary layers for fundamental studies in dispersion and wind power". In: *12th UK conference on wind engineering*. 2016, pp. 5–7.

[21] N Mole and ED Clarke. "Relationships between higher moments of concentration and of dose in turbulent dispersion". In: *Boundary-Layer Meteorology* 73.1-2 (1995), pp. 35–52.

[22] AS Monin and AM Obukhov. "Basic laws of turbulent mixing in the atmosphere near the ground". In: *Tr. Akad. Nauk SSSR Geofiz. Inst* 24.151 (1954), pp. 163–187.

[23] Chiara Nironi. "Concentration fluctuations of a passive scalar in a turbulent boundary layer". PhD thesis. 2013.

[24] Chiara Nironi et al. "Dispersion of a passive scalar fluctuating plume in a turbulent boundary layer. Part I: Velocity and concentration measurements". In: *Boundary-layer meteorology* 156.3 (2015), pp. 415–446.

[25] AM Obukhov. "Turbulence in an atmosphere with inhomogeneous temperature, Tr". In: *Inst. Teor. Geofis. Akad. Nauk. SSSR* 1 (1946), pp. 95–115.

[26] United States. National Oceanic, Atmospheric Administration, and United States. Air Force. *US standard atmosphere, 1976*. Vol. 76. 1562. National Oceanic and Atmospheric Administration, 1976.

[27] Michel Orsi. "Dispersion and mixing in turbulence: data analysis, numerical simulations and modelling". In: (2019).

[28] Frank Pasquill. "Atmospheric diffusion". In: *D. Van Nostrand* 297 (1962), p. 1962.

[29] Stephen B Pope. *Turbulent flows*. 2001.

[30] AG Robins and ROBINS AG. "The development and structure of simulated neutrally stable atmospheric boundary layers". In: (1979).

[31] Lionel Soulhac et al. "The model SIRANE for atmospheric urban pollutant dispersion; part I, presentation of the model". In: *Atmospheric Environment* 45.39 (2011), pp. 7379–7395.

[32] Roland B Stull. *An introduction to boundary layer meteorology*. Vol. 13. Springer Science & Business Media, 2012.

[33] Roland B Stull and C Donald Ahrens. *Meteorology today for scientists and engineers*. West Pub., 1995.

[34] Geoffrey I Taylor. "Diffusion by continuous movements". In: *Proceedings of the london mathematical society* 2.1 (1922), pp. 196–212.

[35] H Tennekes. "Similarity relations, scaling laws and spectral dynamics". In: *Atmospheric turbulence and air pollution modelling*. Springer, 1984, pp. 37–68.

[36] Hendrik Tennekes, John Leask Lumley, Jonh L Lumley, et al. *A first course in turbulence*. MIT press, 1972.

[37] Zellman Warhaft. "Passive scalars in turbulent flows". In: *Annual Review of Fluid Mechanics* 32.1 (2000), pp. 203–240.

[38] Eugene Yee, DJ Wilson, and BW Zelt. "Probability distributions of concentration fluctuations of a weakly diffusive passive plume in a turbulent boundary layer". In: *Boundary-Layer Meteorology* 64.4 (1993), pp. 321–354.

[39] Zhu Yongjian et al. "Association between short-term exposure to air pollution and COVID-19 infection: Evidence from China". In: *Science of the total environment* (2020), p. 138704.